Master's thesis

NTNU
Norwegian University of Science and Technology
Faculty of Natural Sciences
Department of Physics

Lene Fikstvedt

Dosimetric impact of geometric distortions in radiotherapeutic dose planning

Master's thesis in Applied Physics and Mathematics
Supervisor: Ola Engelsen
Co-supervisor: Veronika Tømmerås and Anne Beate Langeland Marthinsen

June 2022

NTNU
Norwegian University of Science and Technology

UNIVERSITETSSYKEHUSET NORD-NORGE

Lene Fikstvedt

Dosimetric impact of geometric distortions in radiotherapeutic dose planning

Master's thesis in Applied Physics and Mathematics
Supervisor: Ola Engelsen
Co-supervisor: Veronika Tømmerås and Anne Beate Langeland Marthinsen
June 2022

Norwegian University of Science and Technology
Faculty of Natural Sciences
Department of Physics

NTNU
Norwegian University of Science and Technology

Summary

Background: Magnetic resonance imaging (MRI) has the potential to improve radiotherapy (RT) treatment by enhancing delineation, removing uncertainties related to image co-registration and aiding functional tissue information. In clinical practice, geometric distortions pertaining to MRI and the resulting dosimetric impact must be addressed to fully integrate treatment planning based on MRI, an MRI-only workflow. Uncorrected geometric distortions may lead to a significant under- or overdosage of tissues and organs. Hence, a quantitative determination of the dosimetric effect is warranted. This study aimed to generally quantify the effect of translational geometric distortions and test the robustness of the results in treatment planning. The results may also be relevant for other treatment planning uncertainties leading to target mislocalisation. This study is limited to translational geometric distortions in two directions in relation to volumetric modulated arc therapy (VMAT).

Methods: Reference treatment plans and distorted treatment plans were created and analysed. In total 78 reference plans and 936 distorted plans were created using phantom images. Translational relocations up to 3 mm in steps of 0.5 mm were introduced by moving the beams isocentre in two directions. The reference plans were chosen to test the influence of the object's shape, photon energy and planning target volume (PTV)'s position, size and composition. In addition, 24 reference plans and 288 distorted plans were generated using synthetic CT (sCT) patient images. The plans were analysed by D_{95}, dose spill and conformity index (CI).

Results: This study found an acceptance of 2 mm translational geometric distortions by investigating D_{95} with a clinically acceptable limit of 5 % dose difference. PTV's position and composition within the phantom and photon energy did not affect this limit. The body shape had minimal impact, although there was an increasing dosimetric difference as the displacements increased. Furthermore, larger targets were found to tolerate larger displacements. Employing phantom data on patient images would result in minimal dose difference (<0.5%) for PTV sizes of 26, 30 and 35 mm in diameter. The results suggest extra considerations for smaller targets combined with large distortions as the dose difference was 1.8 % for 22 mm PTV.

Conclusions: 2 mm translational geometric distortions were found clinically acceptable. Thus, when determining whether an MRI-only workflow is applicable, geometric distortions should be predicted and found below this limit. Larger targets may tolerate larger displacements regarding target coverage. However, the dose accumulated in normal tissue needs further considerations. Phantom results may safely be utilised for patient cases.

Sammendrag

Bakgrunn: Magnetisk resonanstomografi (MR) har potensial til å forbedre strålebehandling ved å forbedre volum inntegning, fjerne usikkerhet knyttet til bildesamregistrering og tilføye funksjonell vevs-informasjon. I klinisk praksis må geometriske forvrengninger knyttet til MR og den resulterende dosimetriske innvirkning bestemmes for å fullt ut integrere behandlingsplanlegging kun basert på MR. U-korrigerte geometriske forvrengninger kan føre til en betydelig under- eller overdosering av vev og organer. Derfor er en kvantitativ bestemmelse av den dosimetriske effekten nødvendig. Denne studien hadde som mål å kvantifisere effekten av translatoriske geometriske forvrengninger samt å teste robustheten til resultatene i behandlingsplanlegging. Resultatene kan også være relevante for andre usikkerheter knyttet til behandlingsplanlegging som fører til feillokalisering av målvolumer. Dette studiet er begrenset til translatoriske geometriske forvrengninger i to retninger ved bruk av Volumetric Modulated Arc Therapy (VMAT).

Metode: Referanseplaner og forvrengte behandlingsplaner ble laget og analysert. Det ble totalt laget 78 referanseplaner og 936 forvrengte planer ved bruk av fantombilder. Translatoriske forflyttinger opp til 3 mm i steg på 0.5 mm ble introdusert ved å flytte strålens isosenter i to retninger. Referanseplanene ble valgt for å teste påvirkningen av objektets form, strålens fotonenergi og planleggingsmålvolumet (PTV) sin posisjon, størrelse og komposisjon. I tillegg ble det generert 24 referanseplaner og 288 forvrengte planer for syntetiske CT (sCT) av pasientbilder. Planene ble analysert ved D_{95}, dosesøl og samsvarsindeks (CI).

Resultater: Denne studien fant en akseptgrense på 2 mm translatoriske geometriske forvrengninger ved å undersøke D_{95} med en klinisk akseptabel grense på 5 % dose differanse. PTV's posisjon og komposisjon i fantomet, og fotonenergi, påvirket ikke denne grensen. Kroppsformen hadde minimal innvirkning selv om doseforskjellen økte når forskyvningene økte. Videre ble det funnet at større målvolum tåler større forskyvninger. Bruk av fantomdata på pasientbilder vil resultere i en minimal dose forskjell (<0.5 %) for PTV-størrelser på 26, 30 og 35 mm i diameter. Resultatene foreslår at ekstra hensyn må tas for mindre målvolum kombinert med store forvregninger ettersom doseforskjellen var 1.8 % for 22 mm PTV.

Konklusjon: 2 mm translatoriske geometriske forvrengninger ble funnet klinisk akseptable. For å avgjøre om en arbeidsflyt basert på bare MR er anvendelig, bør geometriske forvrengninger predikeres og bli funnet under denne grensen. Større målvolum kan tåle større forskyvninger med tanke på målvolumets dosedekning. Likevel krever dosen akkumulert i normalt vev ytterligere vurderinger. Fantom resultatene kan trygt brukes på pasienter.

Acknowledgements

This master thesis was written as the final delivery of the study program Applied Physics and Mathematics at the Norwegian University of Science and Technology (NTNU) in Trondheim. This work was carried out at the PET-centre of University Hospital of North Norway (UNN) in Tromsø during the spring semester of 2022.

I would like to thank my UNN supervisor Ola Engelsen for allowing me to write my master thesis in a clinical environment and for valuable feedback. Furthermore, for the kind words that got me through the mildly claustrophobic MRI scans.

Many thanks to my UNN supervisor Veronika Tømmerås for helping me with the treatment planning system.

I would also like to thank my NTNU supervisor Anne Beate Langeland Marthinsen for taking the time to answer my questions.

A final thanks to my fellow students at NTNU for their support and collaboration during the last five years.

Lene Fikstvedt
Trondheim, June 2022

Contents

Acronyms

AAA analytical anisotropic algorithm. 7, 17

ACR American College of Radiology. 13, 60

CI conformity index. i, 2, 3, 9, 22, 29, 32, 36, 39, 42, 45, 49, 50, 52–61, 69, 88–96

CN conformation number. 9

CT computed tomography. 1, 3–5, 7, 10, 14, 15, 19, 49, 57, 61, 63, 69

CTV clinical target volume. 5

DICOM digital imaging and communications in medicine. 17, 19

DNA deoxyribonucleic acid. 3, 4

DVH dose-volume histogram. 1, 8, 17, 21, 22, 28, 31, 34, 38, 41, 50, 52–60, 69

FFT Fast Fourier transform. 11

FOV field of view. 1, 12, 13, 50, 53, 57, 61

GTV gross tumour volume. 5, 6

ICRU International Commission on Radiation Units and Measurements. 5, 8, 49

IMRT intensity modulated radiation therapy. 6, 7

LINAC linear accelerator. 3, 7, 22

MLC multileaf collimator. 6, 7, 21, 54

MR magnetic resonance. 11, 14

MRI magnetic resonance imaging. i, v, 1–3, 5, 11–15, 20, 49–51, 53, 54, 57–61, 63

OAR organs at risk. 5–8, 60, 61

PET positron emission tomography. 1, 5

PET/MR positron emission tomography/magnetic resonance imaging. 20

PTV planning target volume. i, 1, 5, 8, 9, 17, 21–25, 30–32, 34–36, 40, 41, 43–47, 50–61, 63, 70–77, 79–96

ROI region of interest. 1

RT radiotherapy. i, 1, 3–5, 10, 13, 17, 49, 50, 61

sCT synthetic CT. i, 1–3, 11, 14, 15, 17, 20, 49, 57, 62, 63

TPS treatment planning system. 6–8, 11, 14, 17–19, 21, 58

UNN University Hospital of North Norway. v, 6–9, 15, 17, 20, 22, 49, 50, 57

VMAT volumetric modulated arc therapy. i, 7, 21, 22, 62, 63, 70

List of Figures

1 Introduction

Radiotherapy (RT) is the standard treatment for many types of cancer. It utilises radiation to kill cancer cells. The goal is to deliver a sufficient radiation dose to the tumour and to give as low a dose as possible to the normal tissue. High-quality RT treatment thus relies on precise localisation of the tumour and other vital structures.

Computed tomography (CT) is the golden standard imaging technique for RT planning purposes [1]. The direct relationship between voxel intensity and electron density is utilised and necessary for dose calculation. In addition, CT provides anatomical information for tumour delineation. However, due to the low soft-tissue contrast, other imaging modalities such as magnetic resonance imaging (MRI) and positron emission tomography (PET) may be used in addition to CT to aid better structure visualisation and provide functional tissue information. In such cases, the RT planning workflow, involving several imaging acquisitions and image co-registrations, becomes a time-consuming and resource-demanding process. In addition, uncertainties arise because the images cannot be taken simultaneously, which may lead to biological differences in the images. These differences causes image co-registration complications.

Alleviating these issues, MRI-only workflows exist. Two major MRI-only challenges are 1) the lack of electron density information and 2) geometric distortions inherent to the image acquisition. This thesis addresses the impact of the latter on RT dose planning. Methods have been developed to generate synthetic CT (sCT) images from MRI and thus assigning electron density values to each voxel. Such methods have been implemented and clinically approved with less than 1 % dose difference between sCT and regular CT images, further explained (theory 2.3.3). Geometric distortions may originate from patient-specific or system-specific factors (theory 2.3.2), and are inevitable. If structures are mispositioned, it may compromise dose delivery and treatment effect as the dose is not delivered where it should. Quantifying the dosimetric effect from geometric distortions related to MRI is warranted to validate the MRI-only workflow and to aid in determining which patients may benefit from this workflow.

Previous studies have reported various results regarding the effect of geometric distortions, all from no significant impact [2] [3] to a significant impact of 1 mm geometric offset [4] [5]. Common for these studies is that they investigate one anatomical region using patient data. Hence, the results are only valid for that specific case and depend on the amount of distortions in that region. Walker et al. (2016) [6] argues that the studies concluding with no significant impact are either considering region of interests (ROIs) close to the centre of the field of view (FOV) or utilises a low field MRI, both leading to minimal distortions (section 2.3.2). By investigating a larger ROI they conclude with a significant impact [6].

This study aimed to generally quantify the dosimetric effect from translational geometric distortions in RT. It is a continuation of a small project on the same issue conducted by this author in the autumn of 2021, quantifying translational geometric distortions using a synthetic spherical water phantom. Dose-volume histogram (DVH) analysis showed a significant decrease in dose to planning target volume (PTV) for translational distortions of 2 mm [7]. The validity of this simple result and robustness have been tested by analysing several treatment parameters' impact on the effect of translational geometric distortions. The parameters are body shape, photon energy, and PTV's size, position, and tissue density. Two phantoms with

more realistic shapes have been used in addition to the spherical water phantom. The results are mainly based on phantom images, making the results reproducible unlike some patient studies. In addition, sCT images generated from MRI images of this author's pelvic region have been used and compared to the phantom cases. Translational geometric distortions up to 3 mm in two directions have been analysed by evaluating D_{95}, dose spill and conformity index (CI).

To determine whether a patient may benefit from an MRI-only workflow, the benefits should be compared to the drawbacks. This thesis presents the threshold limit for when translational geometric distortions are clinically acceptable. If the predicted geometric distortions are above this limit, an MRI-only workflow may not be beneficial. The results may extend to predict the dosimetric impact from other uncertainties leading to target mispositioning; Such as patient movement, internal organ motion, patient setup errors and target delineation errors [1]. However, a more elaborate discussion on these uncertainties is beyond the scope of this thesis.

2 Theory

This chapter presents the relevant theory utilised in this thesis. This includes RT principles and the imaging modalities MRI and CT. Geometric distortions concerning MRI will be explained in more detail due to their relevance in this thesis. As mentioned in the introduction, this master thesis is a continuation of previous work performed by this author during the autumn semester of 2021 [7]. Hence, this theory chapter is adopted from the theory section in the project paper and includes some identical paragraphs. However, several changes have been made; The radiotherapy section (section 2.1) has been expanded and include two new subsections about photon interaction with matter (section 2.1.1) and CI (section 2.1.4). Furthermore, a sCT subsection (section 2.3.3) has been added to the MRI section (section 2.3), and a statistical analysis section (section 2.4) has been written.

2.1 Radiotherapy

RT is one of the standard methods used for cancer treatment in addition to chemotherapy, surgery and immunotherapy [1]. External photon beam therapy is generally the most used RT method and will therefore be the focus of this thesis. High energy photons, typically 6-15 MV, are produced and delivered by a linear accelerator (LINAC). The LINAC head, the gantry, can rotate 360 degrees around the patient and irradiate from all angles. Furthermore, the beam is shaped to the target, further explained (section 2.1.2). The principle is to use ionising radiation to kill cancer cells by targeting their deoxyribonucleic acid (DNA) [8]. The treatment aims to deliver a sufficient radiation dose to the tumour and minimise the dose to normal tissue. The treatment should be reproducible, personalised, and conform to the target in order to cure or prolong survival and reduce side effects to the patient [1].

Photons are electromagnetic radiation. They are characterised as indirectly ionising, meaning that they do not not produce chemical or biological damage themselves [8]. Instead, they deposit energy to electrons in the tissue that, in turn, can produce DNA damage [8]. The biological effect may be induced by direct or indirect energy deposition through free radicals. Direct action is when electrons directly ionise the target molecule. Indirect damage is when the electrons interact with a molecule, e.g. water, to produce free radicals that may diffuse and damage the target molecule. 2/3 of the biological damage is caused by indirect damage when using photons, mainly by producing highly reactive hydroxyl radicals (OH·) [8]. Unrepaired DNA damage may cause loss or alteration of genes which may lead to cell death. Typically the cell dies after several attempts to divide, hence expressed hours or days after the inflicted damage [8]. Note, however, that most of the DNA damage is repaired.

2.1.1 Photon interaction with matter

Photons deposit their energy to electrons through three different processes, photoelectric effect, Compton scattering or pair production. Which process occurs depends on the photon energy and the chemical composition of the material [8].

Pair production dominates for photon energies above 25 MeV [8]. The photon energy is converted into a positron and an electron in proximity to a nucleus. The positron will shortly annihilate with an electron

in the tissue, resulting in two 511 kV photons propagating in opposite directions. The electron may interact with other electrons in the tissue that can further produce the DNA damage.

Compton scattering is the dominating process using 6-15 MV photons commonly used in RT treatment [1]. The incident photon interacts with a loosely bound electron, a free electron, i.e. the electron binding energy is small compared to the photon energy. Energy is transferred as kinetic energy to the electron [8]. The photon continues its propagation through the tissue with its remaining energy on a deflected path. Hence, one photon may interact with several electrons as it propagates through the tissue before being fully absorbed. Since the electron is considered a free electron, the probability of Compton scattering is independent of the material.

The photoelectric effect dominates for lower photon energies and is relevant as the photon loses energy and slows down. In addition, it is the dominating interaction when using kV photons, utilised in CT for diagnostic imaging (section 2.2). The photon interacts with a bound electron that is ejected. During this interaction, all of the photon energy is absorbed [8]. The electron vacancy may be filled by an outer shell electron relaxing to a lower energy state, causing the release of a characteristic X-ray. The photoelectric probability decreases as the photon's energy increases and is proportional to Z^3, where Z is the atomic number of the molecule in question. Hence, the amount of photons absorbed through the photoelectric effect depends on the energy and the material.

The reduction in photon energy as it propagates through the body is known as photon attenuation. This property will be explained in more detail later (section 2.2). Regardless of which interaction occurs, fast electrons are produced. These secondary electrons may interact with other electrons in the tissue resulting in a cascade of electrons giving rise to the locally absorbed dose. *Absorbed dose* is defined as the mean energy imparted by ionising radiation per unit mass of an infinitesimal volume [8]. It is commonly measured in Gray [Gy], where 1 Gy is 1 J/kg.

The photon dose and interaction in the body may be visualised at different depths for specific energy through depth dose curves (fig. 2.1). The first part shows the build-up area, characterised by an increasing dose as photons interact with electrons on its path.
The fluence, defined as the number of particles per unit area, increases with depth until the electrons' range is reached. Photon radiation is not suited for superficial tumours as the maximum dose is found after a certain depth. Thus, a tissue equivalent material, bolus, is added to the surface in such cases. The tumour is then relatively shifted deeper, allowing photons to interact with electrons in the bolus. The dose decreases at depths beyond the dose maximum due to attenuation, scattering, and an increased distance from the source governed by the inverse square law [1]. The photon interaction depends on the energy of the photons. For common RT photon energies, higher energetic photons are more forward-directed and interact less than lower energetic photons. This is because the probability of interaction decrease with increasing photon energy. Hence, their dose maximum is further into the body, and they also reach further into the body (fig. 2.1). It is common to use 6 - 10 MV photons as higher energetic photons increases unwanted neutron doses [10] [11]. The photon beam do not have specific energies but a spectrum of energies. The maximum energy is reported, and the mean energy is 1/3 of maximum energy, e.g., the mean energy of the 6 MV photons are 2 MV [1].

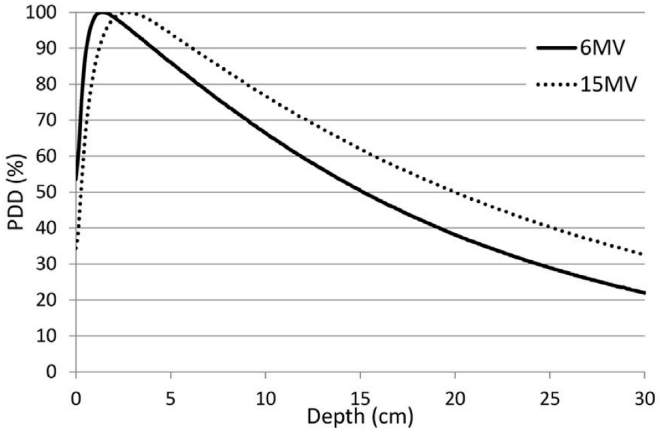

Figure 2.1: Depth dose curves for 6 MV and 10 MV photons for percent depth doses. The figure is obtained from [9] and generated using a 10 x 10 cm field at a 100 cm source surface distance.

The electron density in tissues also determines the probability of photon interaction. Lung tissue has a low electron density compared to water. Fewer interactions occur, and a build-up area is usually found behind lung tissue [1]. Bone has a slightly higher electron density than water, resulting in decreased dose behind the bone. However, since the Compton-effect dominates for MV photons, only a minimal reduction is found behind the bone [8].

In addition to the absorbed dose, the biological effect depends on several other factors such as radiation quality, radiosensitivity, tissue type and cancer type. For example, 1 Gy in a particular target volume may not produce the same biological effect as 1 Gy in nearby organs at risks (OARs). Therefore, a personalised treatment through a comprehensive treatment planning process provides the best possible outcome for each patient.

2.1.2 RT planning

The first step of treatment planning is to localise the tumour and other structures of interest precisely. CT is the most commonly used imaging modality for RT dose calculations due to the straightforwardly available electron density information from CT voxel intensities. However, CT is often supplemented with MRI and/or PET to precisely determine tumour size and extent and to determine the cancer stage [1]. International Commission on Radiation Units and Measurements (ICRU) has presented guidelines to volumes (fig. 2.2) that is recommended for tumour delineation during the planning process. Furthermore, Norwegian national guidelines exist [11]. Gross tumour volume (GTV) is the visible extent and localisation of the malignant growth [1][11]. Clinical target volume (CTV) accounts for any microscopical extension of the primary tumour and may encompass GTV [1][11]. It is the anatomical volume desired to deliver a specific prescribed dose. Note, however, that CTV do not need to contain a GTV, e.g., in cases where the tumour has been surgically removed. PTV encompasses CTV with additional margins added for internal organ motion and treatment delivery uncertainty. Healthy organs tolerate radiation differently depending

on their size, structure and function. Therefore, critical structures need to be delineated and accounted for during the planning process. OAR is defined as healthy tissue near GTV whose irradiation could cause damage that would make changes in the radiotherapy plan and therefore must be considered in the treatment planning [11]. The treatment plan is created based on the target volumes and healthy organs in proximity.

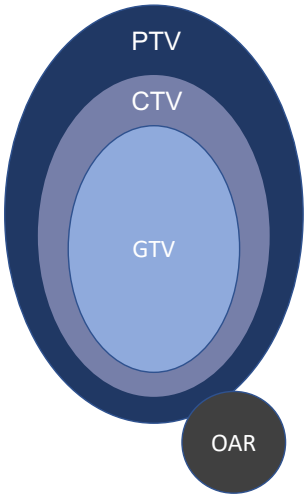

Figure 2.2: The most important volume definitions in radiotherapy. GTV is the gross tumour volume, CTV is the clinical target volume, PTV is the planning target volume and OAR is the organs at risk. The figure is adopted from [1] and is created by this author for the project paper [7].

For the best planning base, the volume delineation should have a high isotropic resolution, and high geometric accuracy and precision [12]. Once the target is defined, a treatment plan can be made in the treatment planning system (TPS). The two main approaches to finding the optimal treatment plan are conventional forward treatment planning and modern inverse treatment planning. Forward treatment planning is considered an iterative trial-and-error method [13]. The dose distribution is calculated after manually adjusting the field components giving a radiation field from "logical" angles. It is time-consuming and may be challenging to determine when the optimal plan is reached [1]. In inverse treatment planning, the desired dose, shape and size of the target, and position of OARs are used to calculate the radiation fields needed [1]. Treatment plans are calculated by dose optimisation algorithms [14]. The algorithms and plan generation may vary between different vendors and TPS. Varian Eclipse is currently in clinical use at University Hospital of North Norway (UNN) and is therefore the TPS used in this thesis. The algorithms are explained in detail in their reference guide [14]. During the optimisation tool, an upper and a lower dose criteria are added for each of the delineated structures. Furthermore, the importance of the different criteria are added as weighting factors. The algorithm searches for the best plan by finding a global minimum of the objective function. Objective functions are defined as the dose difference between the current plan and the dose criteria multiplied by the weighting. The dose criteria are determined for every patient and depends on the treatment intention and cancer type. The Norwegian Directorate of Health has published Norwegian guidelines and procedure for different cancer types [15]. These publications contains the dose recommendations and tolerance limits.

Inverse treatment planning is mainly associated with intensity modulated radiation therapy (IMRT) [13]. The beam is customised using multileaf collimator (MLC) consisting of several lead blocks that can be

moved individually. These are positioned in the LINAC head. By applying different MLC configurations from different directions the beam is shaped to the target. Furthermore, low intensity is achieved in OARs by blocking the beam. The result is a dose distribution that conforms to the target volume [13]. Volumetric modulated arc therapy (VMAT) is a type of IMRT where the beam changes intensity and reshapes continuously as the LINAC head, *gantry*, rotates around the patient [16]. Since VMAT is mostly used at UNN today, this thesis focuses on VMAT plans. Note that since the optimisation algorithm searches for a global minimum based on the given dose criteria, the optimisation stops when the criteria are met. Hence, performing several optimisations may produce different plans. The plans can be characterised by different monitor units (MU), which is a measure of machine output from the LINAC. The LINAC is calibrated at the clinic. A typical calibration setup uses a water tank, a field size of 10 x 10 cm and a source-surface distance of 90 cm. The MU that provides 1 Gy at 10 cm water depth may vary between clinics, and this information is given to the TPS [1]. Furthermore, the TPS requires several other parameters, e.g, depth doses and cross profiles, performed in the clinic [1].

Dose calculations are also performed by the TPS, where different vendors may use different dose calculation methods. Varian Eclipse applies an analytical anisotropic algorithm (AAA), which is a model-based approach comprised of two main components [17]. The first component is a configuration algorithm that determines basic physical parameters to be utilised for the actual dose calculation algorithm. Such parameters are fluence (section 2.1.1) and energy spectrum of photons and electrons and their scattering properties in water equivalent medium. These parameters are pre-simulated using Monte-Carlo simulation and then modified to match the measured beam data. The actual dose algorithm is a 3D pencil beam convolution-superposition algorithm, i.e., separate photon and electron convolutions are superpositioned to obtain the final dose distribution [17]. Primary photons, scattered photons and electrons scattered from the LINAC head are thus separately modelled. In addition, lateral scattering is accounted for by 13 lateral scattering kernels. The 3D volume is divided into voxels and given a mean electron density based on the CT images. The TPS calculates the electron density by using CT-calibration curves relating CT intensity values to electron density for each photon energy. An example of a dose distribution obtained from Eclipse is seen in figure 2.3.

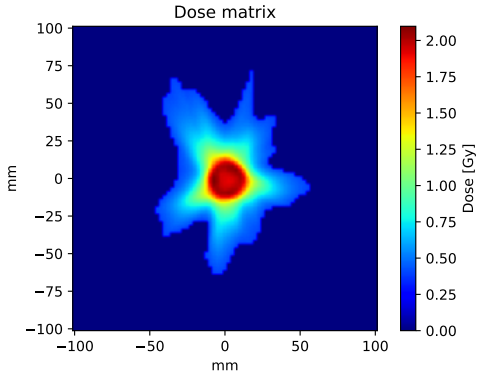

Figure 2.3: 2D dose distribution from VMAT plan obtained from Eclipse 15.1.

2.1.3 Dose-volume histogram

DVH is a graphic representation of the 3D dose distribution calculated by the TPS [1]. An example of a cumulative DVH can be seen in figure 2.4. The x-axis is bin doses, and the y-axis is the relative volume of a structure receiving greater than or equal to the dose. Every line represents one volume or structure. Generally, the goal is a uniform dose distribution within PTV and to have as low a dose as possible outside the volume. Thus, the curve's steepness around the prescribed dose determines the plan's quality, and the curve should therefore resemble a step function. Furthermore, DVHs are used to visualise the dose received by OAR and/or other organs of interest. It is common to evaluate doses to PTV as volume doses $D_{volume\%}$, e.g., D_{50} means that 50 % of the volume receives this dose or more. ICRU [18] and the Norwegian Radiation Protection Authority [11] recommends parameters to be reported for every patient. Typical parameters are near-maximum dose D_2, median dose D_{50} and near-minimum dose D_{98} [11]. These are included in figure 2.4 as dashed lines. Furthermore, they recommend mean doses to be reported [11] [18].

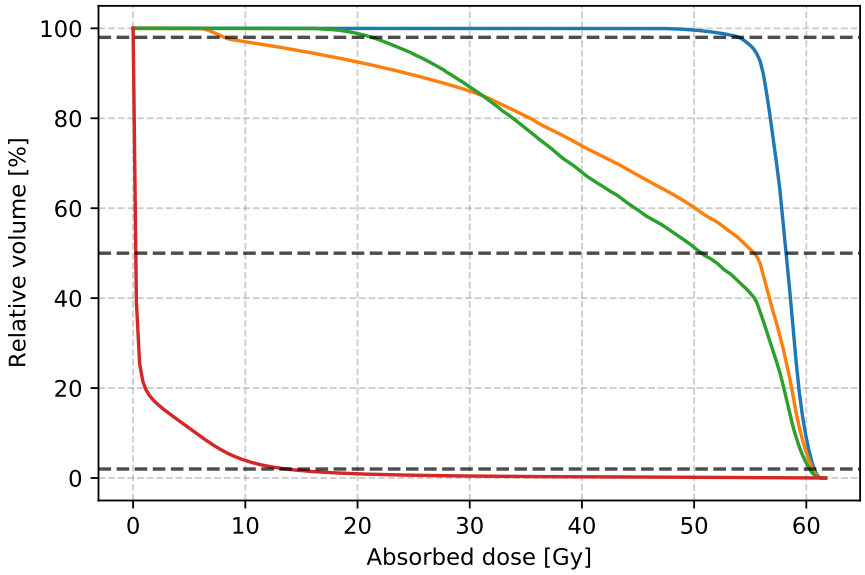

Figure 2.4: Dose-volume histogram. Every line represents one volume or structure. The blue line show a typical PTV. The other lines may resemble OARs or other volumes of interest. The figure also includes D_{98}, D_{50} and D_2 as dashed lines.

Determining the quality of a treatment plan is always a compromise between giving a sufficient dose to the tumour and sparing the normal tissue. At UNN, the dose received by PTV is generally evaluated as the dose received by 95% of the volume, D_{95}. Ideally, 95% of the target volume should receive 95% of the prescribed dose. However, this may vary for some patients. The allowed dose to OAR is determined by tolerance limits specified in the literature [15] (section 2.1.2). Different organs may tolerate a different amount of radiation, and the dose criteria should be obeyed.

In this thesis a clinically acceptable limit of 5 % D_{95} dose difference is utilised. In addition to being a

limit utilised at UNN, this has also been used as the acceptable limit in several other studies on the same issue [2] [3] [4] [5].

2.1.4 Conformity index

Another measure of the treatment plan quality is CI. It is a measure of how well the dose covers the target. The ideal is an equal volume of the prescribed isodose received by the target and the total volume of the isodose and spatial overlap between these two (fig. 2.5).

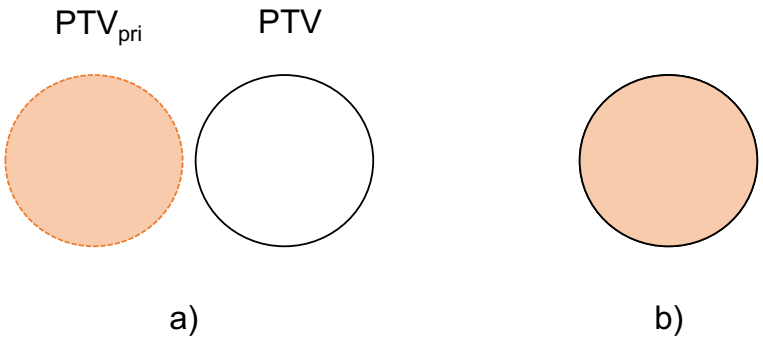

Figure 2.5: Treatment plan quality. The volume of the prescribed dose PTV_{pri} and the volume of PTV should be a) equal in size and b) spatially overlap.

Several CIs have been defined e.g, by SALT group [19], Radiation therapy Oncology group [20], Lomax and Scheib [21] and Van't Riet and Paddick [22]. The SALT group defines CI as the portion of the target volume that receives a certain dose (eq. (2.1).

$$CI = \frac{PTV_{pri}}{PTV} \tag{2.1}$$

PTV_{pri} is the volume of the prescribed isodose inside PTV, and PTV is the volume of PTV. A CI = 1 indicates that all of PTV is covered by the prescribed isodose and thus perfect target coverage (fig. 2.5 b). However, it does not indicate the amount of dose outside the target. The CI defined by Lomax and Scheib [21], also called the healthy-tissue conformity index, describes the portion of the isodose inside the target. This may be turned into a measure of the dose spill by subtracting the healthy tissue CI from 1 (eq. (2.2).

$$\text{Dose spill} = 1 - \frac{PTV_{pri}}{V_{pri}} \tag{2.2}$$

V_{pri} is the volume of the prescribed isodose. Van't Riet and Paddick [22] suggests a combination of SALT [19] and Lomax and Scheib [21] by multiplying SALT CI (eq. (2.1) by the healthy tissue CI (1 - eq. (2.2). Thus, indicating plan quality by including both target coverage and dose spill outside the target. This is referred to as conformation number (CN) [22].

This thesis utilises CI suggested by SALT and the dose spill suggested by Lomax and Scheib. Examining these two values is therefore closely related to CN, but an individual investigation aids a better understanding of the dosimetric differences upon simulation of translational geometric distortions.

2.2 Computed tomography

As mentioned in the introduction (section 1), CT is the golden standard imaging method for RT. The reason is the direct relationship between voxel intensity value and electron density, utilised for dose calculations [1].

2.2.1 Basic principle of CT

CT utilises X-rays and their interaction in the body. The preferred interaction is photoelectric interaction (section 2.1.1), where atoms in the tissue absorb incident X-rays [1]. A tightly bound electron will then be ejected, which results in a loosely bound electron filling the vacancy. A characteristic X-ray is emitted when an electron in the higher energy state relaxes to the lower energy state. The photon's energy corresponds to the energy difference between the binding energy of the two electrons; It is typically not more than a few keV and will be absorbed by the tissue [23]. Hence, the incident X-ray will be fully absorbed and not reach the detector. The absorbed amount of the incident beam is referred to as attenuation. The transmitted intensity I detected gives information about the attenuation of the beam during its propagation through the body given by

$$I = I_0 e^{-\mu L}, \tag{2.3}$$

where I_0 is the incident beam intensity, μ is the linear attenuation coefficient and L is the travelled distance [23]. The attenuation difference in different tissues gives the contrast in the image.

The CT scanner consist of a X-ray fan-beam and an array of detectors on the opposite side. The setup can be seen in figure 2.6.

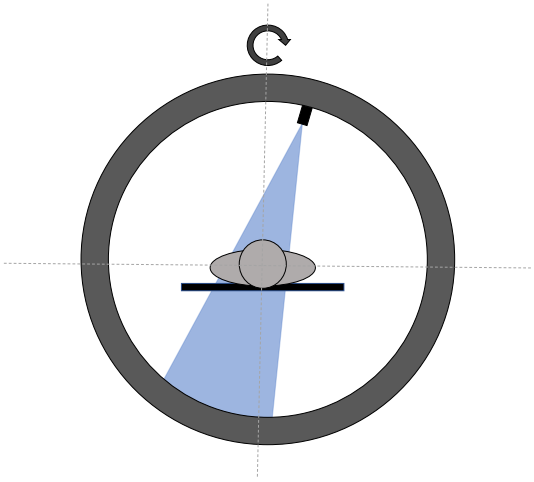

Figure 2.6: The CT scanner. The source is an X-ray fan-beam that can rotate around the patient. An array of detectors on the opposite side registers the transmitted beam.

By collecting one-dimensional projections along 180° in all directions, attenuation coefficients can be measured. It results in an attenuation map. For convenience, the attenuation map may be converted into

Hounsfield units (HU) by

$$HU = \frac{\mu - \mu_{H_2O}}{\mu_{H_2O}} * 1000.$$

HU is normalised to water; Thus water is defined as 0 HU while air is -1000 HU [23]. HU calibration curves are used by the TPS to convert HU for each voxel in the image to electron density information (section 2.1.2).

2.3 Magnetic Resonance Imaging

MRI is a noninvasive imaging technique. Compared to other imaging techniques, MRI offers exquisite soft-tissue contrast, functional information, and the ability to image tissues in arbitrary planes [24]. A detailed description of MRI is very elaborate and beyond the scope of this thesis. The interested reader is referred to the many excellent textbooks on the issue, e.g. [25] [26]. This section will focus only on the most essential MRI theory pertaining to this thesis, i.e. spatial encoding and geometric distortions. An understanding of the latter is important because it is one of the limiting factors in the MRI-only workflow. Furthermore, a magnetic resonance (MR) scan was performed during this thesis testing the dosimetric impact of translational geometric distortions (section 3). This chapter also includes a section about sCT as sCT images need to be generated from MRI images to obtain the electron density information in an MRI-only workflow.

2.3.1 Spatial encoding MRI

Spatial encoding is the method used to spatially locate the MRI signal based on difference in precessional frequencies [25]. The Larmor frequency ω_0 is the proton's precession rate around the external magnetic field B_0, described by the Larmor equation (2.4). The gyromagnetic ratio γ is given in MHz/T and varies between atomic species [25].

$$\omega_0 = \gamma B_0 \tag{2.4}$$

Three pulsed-field gradients are applied to influence the precessional frequency. A gradient is a sloped magnetic field generated by electromagnets [25]. This extra linear magnetic field will add to the external magnetic field and cause *precessional* frequency- and phase shifts depending on the position of the spins. Figure 2.7 shows an example pulse sequence diagram containing the gradients and pulses necessary for spatial encoding. A slice-select gradient is applied simultaneously as the rf-pulse, in the direction of the magnetic field. This gradient enables excitation of one slice by applying an rf-pulse with the appropriate frequency bandwidth, selectively causing resonance in the desired slice. A frequency gradient enables signal localisation along the long axis of a slice. It is applied when recording the signal and is often called a readout gradient. A phase encoding gradient is applied after the rf-pulse giving the spins an initial phase difference that enables localisation along the short axis before signal readout. The signal is stored in the spatial frequency domain, k-space [25]. Fast Fourier transform (FFT) is performed to reconstruct the image by calculating the signal intensity for each pixel position.

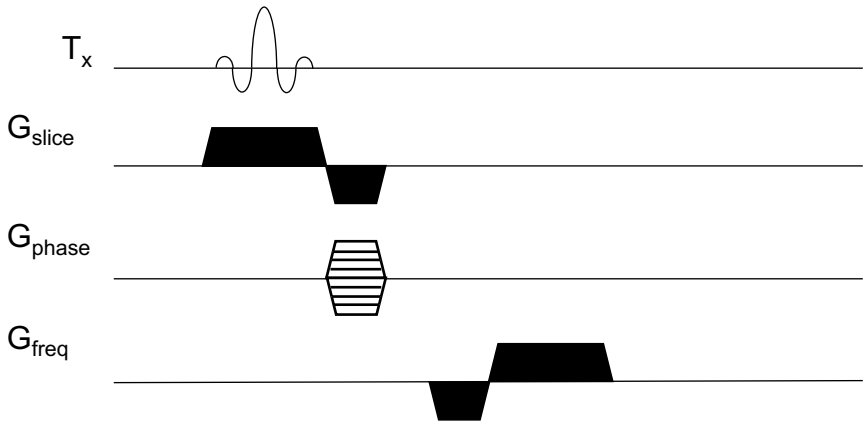

Figure 2.7: Pulse sequence diagram for spatial encoding in MRI. The sequence displayed is the gradient echo sequence, the simplest sequence for spatial encoding. First, a slice-selective pulse combined with a slice-selective gradient is applied. Note that the gradient is followed by a rewind lobe reversing the additional phase accumulation from half of the slice gradient. Second, a phase gradient gives spins at different positions along the phase encoding direction a phase change before the readout. The steepness of the gradient is changed for every excitation pulse. Third, a readout gradient is applied to record the signal giving the spins a frequency depending on their position along the frequency encoding direction.

2.3.2 Geometric distortion

Geometric distortion is one of the faults limiting MRI as the primary imaging technique for treatment planning [1]. It can be separated into two categories, system-induced distortions and patient-induced distortions [27] [24]. Geometric distortions are found up to 15 mm [28]. However, corrections may be applied to reduce distortions.

System-induced distortion

As the name implies, system-induced distortion arises from limitations in the system hardware. This involves the external magnetic field B_0, the gradients and the applied magnetic field B_1. The external magnetic field B_0 cannot be perfect, and inhomogeneities will occur [25]. The image construction relies on a homogeneous magnetic field to locate the spins based on their precessional frequencies (section 2.3.1). An inhomogeneous magnetic field causes local differences in the frequency, leading to image distortions seen as translation relocation and loss of signal in the direction of the slice-select gradient and the frequency encoding gradient [1]. The distortion magnitude is inversely proportional to the applied gradient strength. Non-linear gradients also lead to unwanted differences in precessional frequencies, which leads to translational relocation in all encoding directions. Non-linear gradients may be a result of eddy-currents. Eddy-currents are induced currents related to switching on and off the gradient, affecting the gradient. Thus, sequences involving quick changes in the gradients are more prone to eddy currents, e.g. echo-planar imaging sequences. The magnitude of distortions related to non-linear gradients is independent of the gradient strength [27]. An inhomogeneous magnetic field from the rf-pulse B_1 will result in uneven excitation giving different flip angles in the FOV. The result is signal loss which gives shading artefacts in the image. It can also be a result of different sensitivity in the receiver coils.

System-induced distortions depend on the applied imaging sequence and increase with increasing distance from the magnetic isocentre [1]. Hence, a larger FOV is more prone to geometric distortions. Several methods have been developed to correct these errors. By an extensive measurement of phantoms, maps of system distortions have been created. Implementing this method has proven to reduce distortions from 9 mm to 1 mm [1]. Furthermore, Eddy currents can be reduced by creating pre-compensated gradients. According to American College of Radiology (ACR) [29], system-induced geometric distortions should not exceed 2% in images used for RT planning purposes. This thesis investigates the effect of translational geometric distortions up to 3 mm in two directions.

Patient-induced distortion

Patient-induced distortion arises because of patients' individual composition. Magnetic susceptibility and chemical shift effects make up the two causes of patient-induced distortions. [1].

Magnetic susceptibility is the degree to which a substance is affected by a magnetic field and is an intrinsic property of a substance [30]. Water is slightly diamagnetic, which causes a decrease in the magnetic field. On the other hand, air is slightly paramagnetic, increasing the magnetic field strength (fig. 2.8) [24]. Protons in an environment with different magnetic susceptibility will therefore precess with slightly different frequencies and phases. The result is a misinterpretation of position and spin dephasing in the tissues' interface, leading to signal loss or geometric distortions. Hence, the signal loss or distortions are particularly pronounced at boundaries between two substances with different magnetic susceptibility, e.g. water and air boundary. Some imaging sequences are more prone to magnetic susceptibility differences, e.g. T_2^* weighted sequences with long echo times TE. When applying the slice selective and readout gradient, the linear gradients will be affected by the change in the magnetic field (fig. 2.8). The changes in the magnetic field at interfaces will give a steep gradient moving from water to air and a shallow gradient moving from air to water. The effect is a stretched area and a squeezed area in the image. Other objects such as metal implants will cause large magnetic susceptibility artefacts and image distortions.

Chemical shift artefacts appear due different proton shielding from the magnetic field in different chemical environments [25]. Oxygen is an electronegative atom and thus attract electrons from the hydrogen atoms in water. Protons in water are thus less shielded from the external magnetic field than protons in fat. Hence, they experience the field more and precess at a slightly higher Larmor frequency ω_0 compared to protons in fat. MRI assumes that all protons are water, and a shift in frequency results in misinterpretation of position in the frequency encoding direction. The shift depends on the frequency differences, frequency bandwidth and FOV, given by equation (2.5).

$$\delta = \frac{(\omega_2 - \omega_1)FOV}{BW} \tag{2.5}$$

Since patient-induced distortions depend on the patients' composition, they vary from patient to patient and are more challenging to correct than system-induced distortions [1]. However, fat suppression methods can be used to remove the signal from fat. In addition, increasing the bandwidth, lowering the field strength and using a smaller FOV reduces chemical shift artefacts, as seen from equation (2.5). Another effect of chemical shift is chemical misregistration. At some point, the spins from water and fat will be out of phase, as they precess at different frequencies. A signal loss will appear if the signal is recorded at that time. However, this

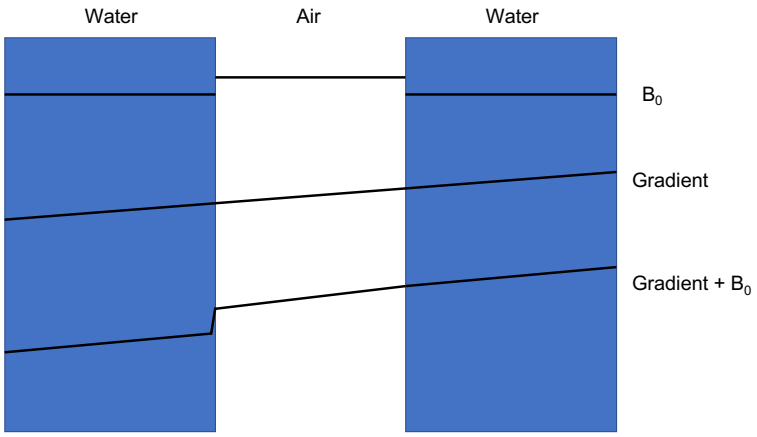

Figure 2.8: Figure illustrating the effect of magnetic susceptibility. Water is diamagnetic and air is slightly paramagnetic. Thus, the magnetic field changes depending on material. When applying the linear gradient, the result is a stretched out area when going from water to air, and a squeezed are when going from air to water.

can be avoided by adjusting TE to record when water and fat are in phase or by using a spin-echo sequence.

2.3.3 Synthetic CT

The direct relationship between CT voxel intensity and linear attenuation (eq. (2.3) is used for dose calculation by the TPS (section 2.1.2). Therefore, methods to construct sCT images from MRI for MRI-only exists. Two approaches are: the bulk density approach, and the atlas-based approach [31]. This section will describe the idea of these two approaches and delve deeper into the artificial intelligence (AI) based method delivered by Siemens Healthineers.

The bulk density approach is to segment structures and assign CT values. The segmentation is based on the MRI images, where structures are mainly segmented into air, bone, and soft-tissue [31]. Dedicated MRI sequences allows the segmentation based on MRI intensity values. Dixon method is commonly used. T1 VIBE DIXON sequence acquires images where water and fat are in-phase, IP, and opposite-phase, OP [32]. Furthermore, water-only and fat-only images can be created according to equation (2.6), further utilised for threshold intensity value segmentation. However, this method struggles with differentiating bone and air as these structures give the same low MRI signal. Additional sequences to acquire bone information, such as ultrashort echo time sequences, may be applied.

$$\begin{aligned} \text{Water only} &= (IP + OP)/2 \\ \text{Fat only} &= (IP - OP)/2. \end{aligned} \tag{2.6}$$

The atlas-based approach generate sCT based on comparing the MRI images to a pre-compiled atlas of paired MRI and CT images from patients that have undergone both MR and CT examinations [31]. However, this method is limited to the amount of data available, resulting in difficulties in handling atypical anatomy.

Siemens Healthineers have recently released an AI-based algorithm for continuous HU generation from MRI images. The algorithm is explained in their white paper [33] and a brief explanation will follow in this paragraph. It is clinically approved and currently limited to brain and pelvis images only. The algorithm is a deep neural network trained to learn sCT construction. It is trained using large numbers of paired MRI and CT images. The network architecture comprises two parts. The first part is a convolutional neural network to segment MRI images acquired using the T1 VIBE DIXON sequence into background, bone and soft tissue. The second part is a generator and discriminator that takes the in-phase and opposite-phase information and the segmentation information from the first part to construct the sCT. The discriminator tries to compare the constructed sCT to the ground truth, the real CT image, and the differences are given back to the algorithm to provide an optimised sCT image. The algorithm is delivered fully trained to the user on Syngo.via RT-image suite VB60, which is utilised at UNN. The AI has been clinically approved where dose differences between sCT and planning CT was found below 1 % [33].

2.4 Statistical analysis

The theory used for statistical analysis is presented in this section.

2.4.1 Mean and standard deviation

When analysing samples, mean and standard deviations are commonly used. Mean is a measure of the central location and is given by

$$\overline{x} = \frac{\sum_{n=1}^{N} x_n}{N}. \tag{2.7}$$

The mean $\overline{x}$ is the average of all observations x_n from 1 to N. Note however, that it is sensitive to extreme values and may not always be a good measure of the central location.

The standard deviation is a measure of the samples' spread . It is defined as the summary of differences of each observations from the mean [34] given by

$$SD = \sqrt{\frac{\sum_{i=1}^{N}(x_i - \overline{x})^2}{N-1}}. \tag{2.8}$$

x_i is the sample, N is the number of samples and $\overline{x}$ is the mean. For an accurate and good statistical result, number of samples should be large [34].

2.4.2 Statistical testing - Mann Whitney U test

Two sample t-tests may be utilised to compare two sets of measurements. It is often based on mean, median and variance values of the two data sets [34]. The result is a p-value determining whether or not to reject the formulated null hypothesis. It is common to reject the null hypothesis if the p-value is below 0.05, meaning there is less than a 5% chance that the difference is random. Hence one can conclude that there is a statistically significant difference between the data sets.

The Mann-Whitney U-test, also called the Wilcoxon rank-sum test, is a non-parametric test that compares two unpaired groups [34]. Non-parametric tests do not assume that the data comes from a specific distribution, and unpaired groups means that there is no connection between the measurements. The null hypothesis states that the two groups are equal and from the same distribution. All values are ranked from 1 to n, independent of which group they belong. One is given to the smallest number, and n is given to the highest number. The average of each group is calculated according to (2.7). If the averages are very different, the p-value will be small. If $p<0.05$, the null hypothesis is rejected, and one can conclude with 95% certainty that the difference between the distributions is not random.

3 Method

This thesis aimed to quantify the dosimetric impact of translational geometric distortions (section 2.3.2) on general terms. Several parameters' impact have been tested, such as phantom shape and photon energy, and PTV's size, position and tissue density. Three different phantoms have been used. In addition, a patient image of this author has been investigated to verify whether the results may translate to real patient images.

The method was to collect images, import them into TPS, create reference- and distorted plans, and at last evaluate the dose matrices and DVH (section 2.1.3) information. Translational geometric distortions was introduced by moving the beam isocentre in the TPS. Moving the beams isocentre in one direction is equivalent to moving the body in the opposite direction but the latter was considered more time-consuming. The distorted plans were thus the same, i.e., the same arc as the reference plans. Due to the findings in the project paper [7], only distortions up to 3 mm were investigated but now in more detail at a higher resolution. The translational geometric distortions were introduced in steps of 0.5 mm in two directions.

The method will be thoroughly explained in the following.

3.1 Software

Syngo.via RT Image Suite VB60, provided by Siemens Healthineers and accessed at UNN, were used to visualise the image scan performed on PET/MR. Furthermore, RT Image Suite provides the tool to generate sCT images (theory 2.3.3). The images were exported from Syngo.via to be imported into the TPS. The TPS used was Eclipse version 15.1, Varian Medical Systems. This is the standard TPS in clinical use at UNN. It utilised an AAA for dose calculation (theory 2.1.2). After creating RT-plans, digital imaging and communications in medicine (DICOM) files were exported from TPS. Python3 was used to analyse the DICOM files. All code created for analysis is found in the appendix F. Prism 9 was used in addition to Python to plot some of the graphs and to perform the statistic tests (theory 2.4). Orakeltjenesten at NTNU gave the license to the program on request from this author.

3.2 Image generation

Three phantoms were used in this study; A spherical water phantom, a pelvis phantom and a NEMA IQ phantom. In addition, patient images of this author were used.

3.2.1 Spherical water phantom

The sCT spherical water phantom (fig. 3.1) was digitally created using Python3 during the autumn of 2021 for the project report [7]. Thus, the creation method is explained in detail in the project report, but the code is also attached (appendix F). This was considered the simplest case evaluated. The spherical water phantom was 20 cm in diameter and the image resolution was 0.98 x 0.98 x 5 mm.

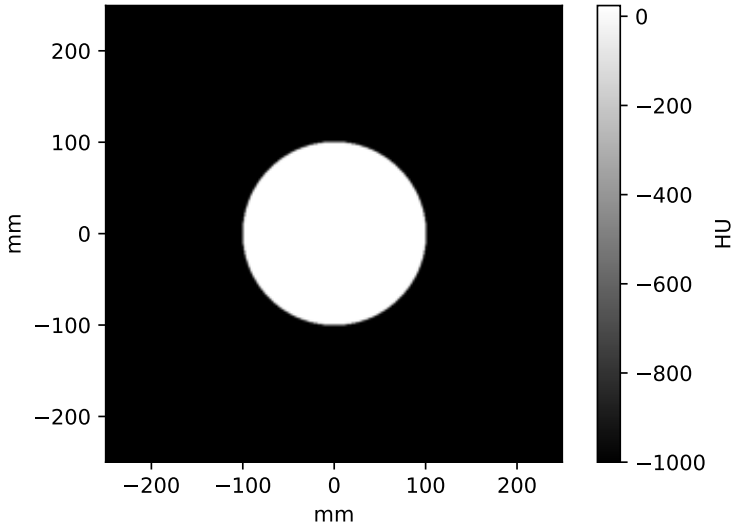

Figure 3.1: The spherical digitally created water phantom. The image resolution was 0.98 x 0.98 x 5 mm and the phantom diameter was 20 cm.

Even though the sphere was evaluated during the project paper, new plans were created to get better statistical results. In addition, translational geometric distortions in steps of 0.5 mm were performed contrary to 1 mm steps performed in the previous report [7]. The spherical shape was chosen to give an isotropic dose distribution where translational movement in one direction is equivalent to all directions. Therefore, only distortions in one direction, +x-direction, were investigated on this phantom and assumed to be equal in the -x-direction.

3.2.2 Pelvis phantom

The images of the pelvis phantom (fig. 3.2) were received from the supervisor during autumn of 2021. They were the images replaced with the digitally created spherical water phantom explained above (section 3.2.1). Hence, the pelvis phantom images have the exact image resolution as the spherical phantom. The phantom resembles a human pelvis and contains a simulated spine inside. The table in the images (fig. 3.2) is ignored by the TPS by defining a body contour excluding the table.

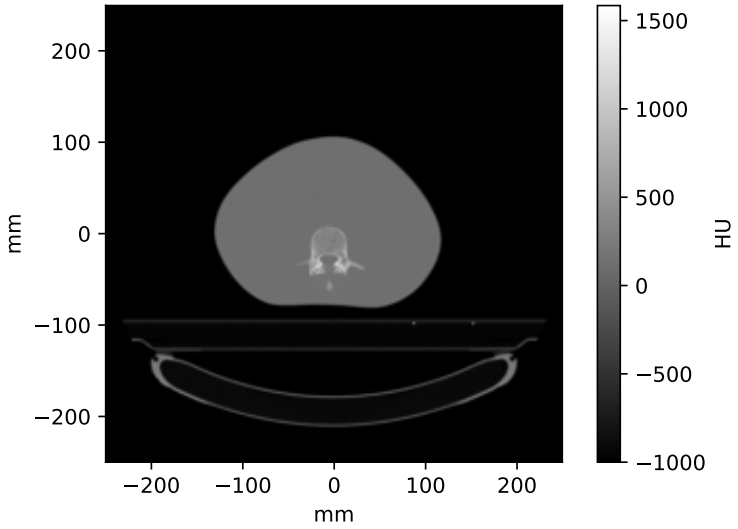

Figure 3.2: The pelvis phantom with a spine inside. The image resolution was 0.98 x 0.98 x 5 mm.

Several cases have been investigated using the pelvis phantom and will be explained in more detail in section 3.5. This phantom was chosen because it resembles a human pelvis and thus has a shape more realistic than the spherical phantom. Furthermore, the spine enables investigations of the influence of bone on the effect of translational geometric distortions.

3.2.3 NEMA IQ phantom

The NEMA IQ phantom was chosen as it resembles a human torso. It is built of acrylic glass material and contains six hollow glass spheres that may be filled with activity. These spheres have 10, 13, 17, 22, 28 and 37 mm inner diameter. Additionally, a cylinder filled with styrofoam is positioned in the centre to resemble lung tissue. The lung insert is 51 mm in diameter and 180 mm in length. The images was collected in cooperation with supervisor Ola Engelsen 15.02.22 on the occasion of an annual control. The scanner used was a Siemens hybrid PET/CT. In this thesis, only the CT image of the NEMA IQ phantom is of interest. Therefore, the preparation details such as activity concentrations are not important and will not be explained. The DICOM files were exported from Syngo.via and imported into TPS. The image resolution was 0.98 x 0.98 x 0.6 mm. Thus, a higher resolution was applied for the NEMA IQ phantom than the other two phantoms. In addition, The lung insert makes it more advanced and thus realistic and enables testing of different tissue density effects on translational geometric distortions. The plans created using the NEMA IQ phantom will be further explained in section 3.5. As explained for the pelvis phantom (section 3.2.2), the table is ignored by TPS.

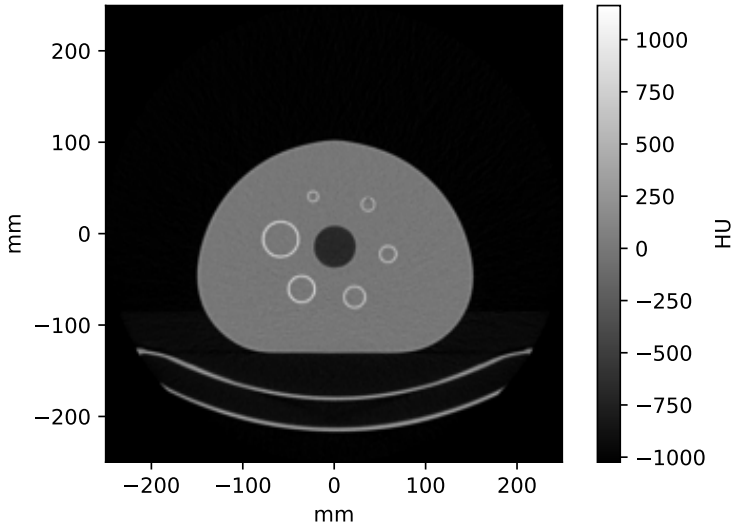

Figure 3.3: The NEMA IQ phantom. The image resolution was 0.98 x 0.98 x 0.6 mm.

3.2.4 Patient images

The patient images utilised were images of the pelvic region of this author from an MRI examination on the hybrid positron emission tomography/magnetic resonance imaging (PET/MR) at UNN 18.03.22. The images were taken using the T1 VIBE DIXON sequence (section 2.3.3). SCT images were generated in Syngo.via RT images suite. The image resolution was 2 x 2 x 3 mm. The pelvic region was chosen because of its resemblance to the pelvis phantom. Furthermore, the sCT generation at Syngo.via is limited to head and pelvis (theory 2.3.3).

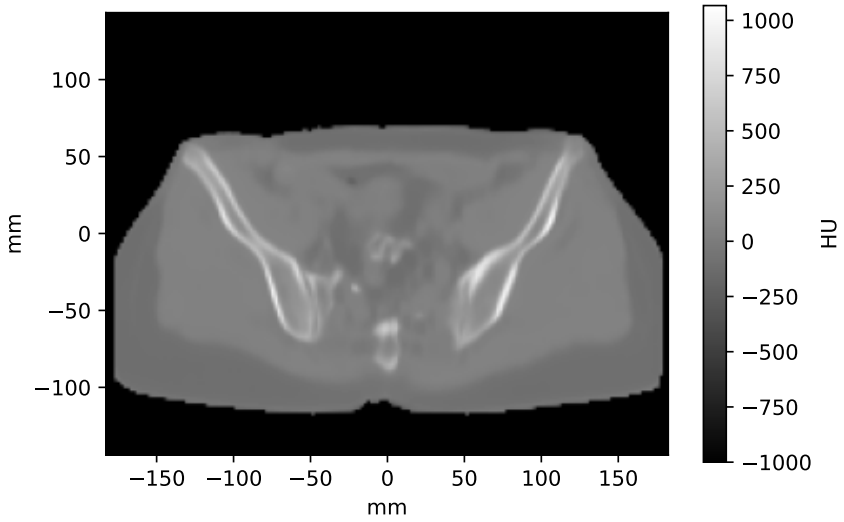

Figure 3.4: Pelvis sCT image of this author. The image resolution was 2 x 2 x 3 mm.

3.3 Treatment plan generation

The images were imported to the TPS. PTVs were created using the contouring tool. In the cases where the same PTV was desired, PTV was duplicated and copied over to these cases. Spherical PTVs with 22 mm diameter were mostly used, but the influence of PTV's size on the impact of translational geometric distortions was also investigated (section 3.5.2).

VMAT plans (theory 2.1.2) were created using the external beam planning tool. All plans were generated using the same parameters. The prescribed dose was 2 Gy delivered in one fraction. 2 Gy was chosen as it is the standard fractionation dose used clinically [35]. The photon energy was chosen to be 6 MV, although different energies' impact was one of the cases investigated, further explained in section 3.5.4. Photon attenuation depends on the energy of the photons (theory 2.1.1), where the attenuation decrease with increasing energy. Therefore, choosing the lowest energy provided by TPS, 6 MV, may represent a worst-case scenario. Furthermore, 6 MV photons are often preferred (theory 2.1.1) [10]. The gantry rotation was a full rotation from 179 degrees to 181 degrees, counterclockwise. MLCs and collimators were added and fitted to the PTV structure. The plans were optimised for upper and lower dose criteria for PTV (theory 2.1.2). The upper criteria was set to 0% of the volume receives a larger dose than 2.13 Gy. This criteria was weighted 75. The lower criteria was set to 100% of the volume receives a greater dose than 1.97 Gy. This criteria was weighed 100. The collimator rotation was chosen to be 30 degrees for all plans. The reference plan was normalised to 100% of the dose covering 50% of the target volume because of recommendations from The Norwegian Radiation Protection Authority [11]. Since the relative dose difference between the reference and distorted cases was of interest, the plan parameters were considered unimportant. The goal, however, was to create a good reference plan. After testing different parameters, these criteria and the plan parameters were chosen as they produced a DVH that resembled a step function around the prescribed dose

(theory 2.1.3).

The distorted cases were created by copying the reference plan and moving the beam's isocentre. The beam's isocentre was moved to 3 mm in +x and -x directions in steps of 0.5 mm. Dose calculations were performed with the same arc after moving the isocentre. The LINAC at UNN was calibrated so that 130 MU provided 1 Gy at 10 cm water depth with a field size of 10 cm x 10 cm and a source-surface distance of 90 cm. Six different plans were created for every case to produce statistical results. Different plans are characterised by their different MU values (theory 2.1.2). During this work, 102 VMAT plans were created and optimised, 1326 dose calculations were performed, and thus 1326 plans were individually exported and analysed.

3.4 Evaluation of the exported DICOM files

Again, Python3 was used to analyse the files. DVHs were reconstructed from the RT dose files and D_{95} (theory 2.1.3) were calculated by finding the intercept between the DVH, a 95% volume line, and the dose at this volume (appendix F). Prism 9 was used to create the plots presented because its simplicity and the ability to switch what component to show. Hence, D_{95} information was manually transferred into Prism 9 for all cases. Furthermore, the DVH information were used to calculate the CI (eq. (2.1) and the dose spill (eq. (2.2), theory 2.1.4). The CI was divided by 0.5 because the dose was normalised to 100% of the prescribed dose, covering 50% of the target. Thus, a CI of 1 was obtained for all the reference plans.

3.5 Evaluation cases

As stated above (section 3), several factors may influence the dosimetric impact of geometric distortions. Such factors may be the quality of the reference treatment plan, plan parameters, e.g., photon energy, plan type, HU in the volume of interest or proximity to the volume of interest, the targets' size and shape, the volumes' position in the body and the shape of the body. A few parameters were carefully selected for illustrative clarity. In the following, these parameters will be explained. Again, all cases were tested by moving the beams' isocentre from 0 to 3 mm in positive and negative x-direction in steps of 0.5 mm.

3.5.1 Body shape

The body shape may influence the dosimetric impact of geometric distortions, i.e., some anatomical regions may be more exposed to translational geometric distortions. This was tested by using all three different phantoms stated above (section 3.2); The spherical water phantom (section 3.2.1), the pelvis phantom (section 3.2.2) and the NEMA IQ phantom (section 3.2.3). Attempts were made to isolate the effect of body shape and minimise other parameters' influence. Therefore, all phantoms were given the same spherical PTV of 22 mm positioned in soft tissue. Furthermore, the PTVs were positioned to the best effort at the centre of the spherical and pelvis phantom. However, because of the simulated spine, PTV was not positioned at the exact centre of the pelvis phantom. Nevertheless, this PTV position is referred to as the centre position in the rest of this thesis. For the NEMA IQ phantom PTV was placed at the 22 mm diameter glass sphere

because of the lung insert in the centre. Figure 3.5 shows the reference dose distributions overlaid with the phantom images.

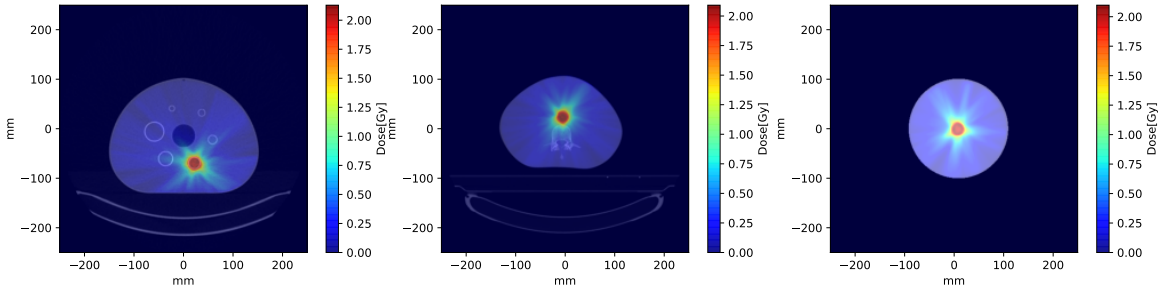

Figure 3.5: Dose distribution within the phantoms testing the influence of body shape. The left image shows the dose distribution of a reference plan generated for the NEMA IQ phantom. The middle shows the Pelvis phantom and the spherical phantom on the right. PTV was 22 mm in diameter and positioned in soft tissue.

3.5.2 PTV size

The size of PTV may influence the dosimetric impact. Spherical PTVs of 22, 26, 30, and 35 mm were tested. The PTVs were, to the best effort, positioned at the centre of the pelvis phantom in soft tissue. However, when a volume was so large that a position at the centre would cause the volume to cover part of the simulated spine, the volume was moved. The dose distribution and thus the position of PTV is seen in figure 3.6. Note that only dose distributions for the 26, 30 and 35 mm PTV size are shown. This is because the 22 mm case is the same as the pelvis phantom case used to investigate the body shape and is therefore seen in figure 3.5. The pelvis phantom was chosen to investigate the PTV size influence because it resembles a human body more than the spherical water phantom and may give more realistic results. In addition, the resolution of the NEMA IQ phantom made the plan generation, dose calculation and file export much more time-consuming and it was therefore not chosen. In addition to the plan analysis explained (section 3.4), the volume of the dose spill was evaluated for each PTV size.

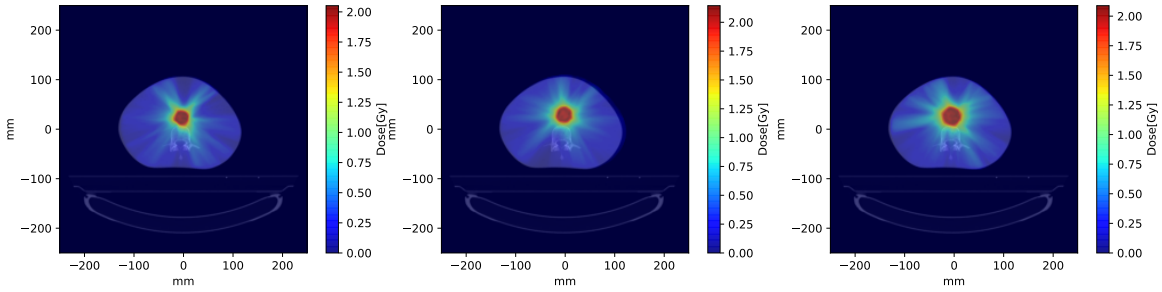

Figure 3.6: Dose distribution within the pelvis phantom testing the influence of PTV size. The images show 26 mm, 30 mm, and 35 mm PTV from left to right.

3.5.3 PTV position

The PTV position was also investigated using the pelvis phantom. A spherical PTV with a 22 mm diameter were placed at the centre of the phantom. In addition, the same PTV was placed 3 cm, 6 cm and 9 cm in positive x-direction on the phantom. The volumes were placed to the best effort at the same position in the y and z-directions. Figure 3.7 show the reference dose distributions for 3 cm, 6 cm and 9 cm. The centre case is the same as used to investigate the phantom shape influence.

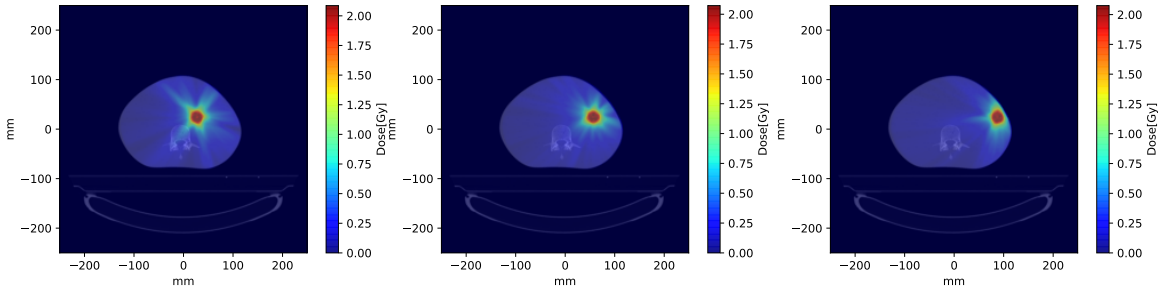

Figure 3.7: The dose distribution within the pelvis phantom for PTV's positioned 3 cm, 6 cm and 9 cm from the centre of the phantom from left to right.

3.5.4 Photon energy

The photon interaction in the body depends strongly on their energy (theory 2.1.2). Higher-energy photons propagate further into the body than lower-energy photons and thus have a dose maximum at a greater depth. Therefore, the photon energy influence on the dosimetric impact of translational geometric distortions was investigated. The energies tested were 6, 10 and 15 MV. The pelvis phantom (fig. 3.2.2) was used with a 22 mm diameter spherical PTV placed at the centre. Again, the pelvis phantom was used as it is more realistic than the spherical phantom and less time-consuming to work with than the NEMA IQ phantom.

3.5.5 Tissue density

Three cases of different tissue densities were tested and compared. The same 22 mm PTV was positioned in the soft tissue of the pelvis phantom, in the simulated spine (compact tissue) of the pelvis phantom, and in the lung insert in the NEMA IQ phantom. The corresponding dose distributions is found in figure 3.8.

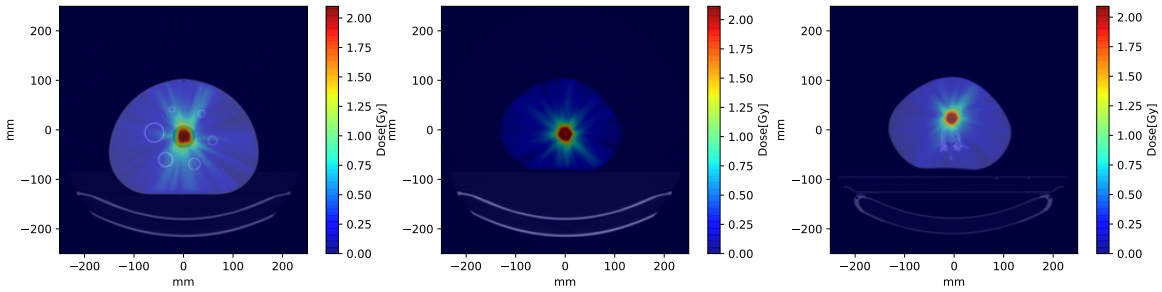

Figure 3.8: The figure shows the dose distributions generated to investigate the influence of PTV density. The left image shows the dose distribution within the NEMA IQ phantom with PTV positioned in the lung insert. The middle image shows the dose distribution when PTV is positioned in the spine of the pelvis phantom. The image to the right shows the dose distribution when PTV is positioned in soft tissue in the pelvis phantom.

3.5.6 Patient case

For the patient case, 22, 26, 30 and 35 mm diameter PTVs were investigated. These were chosen because the phantom results showed a significant dependence on the effect of translational geometric distortions on the target size. PTV were positioned in soft tissue, and the position and dose distributions is shown in figure 3.9. In addition to the evaluation previously described (section 3.4), the volume of the dose spill was evaluated for each PTV size. Furthermore, the D_{95} dose difference between the patient images and the results from phantom images testing PTV size (section 3.5.2) were calculated. This was performed to estimate the percentage dose difference using phantom data on patient images.

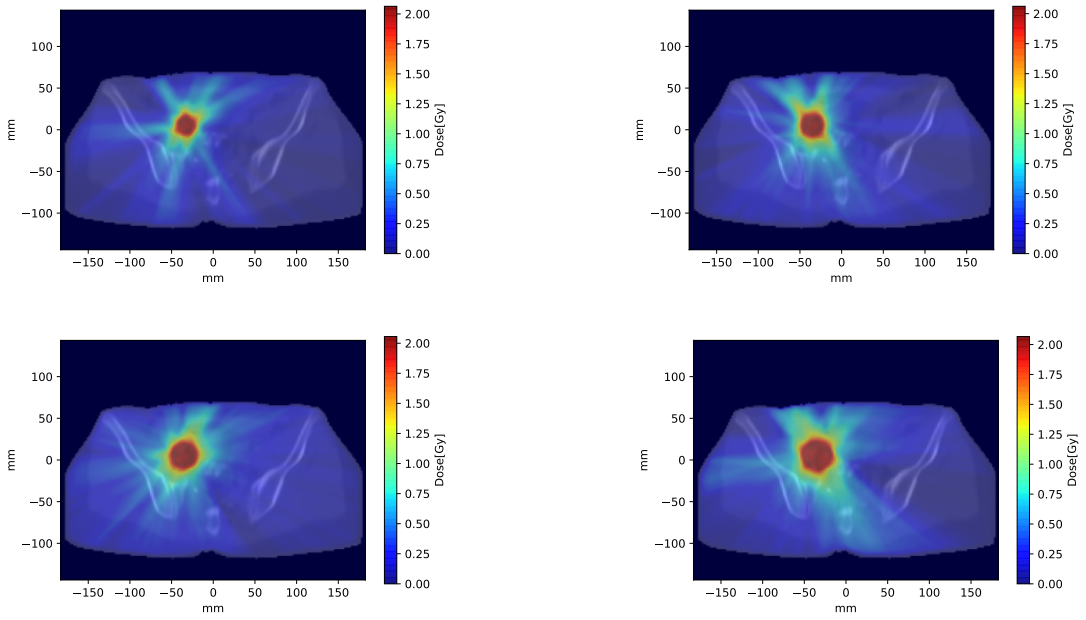

Figure 3.9: The figure shows examples of dose distributions generated for the patient cases. The top images show a plan optimised for 22 mm and 26 mm PTV from left to right. The bottom left plan has 30 mm PTV, and the bottom right has 35 mm PTV. The PTVs were positioned in soft tissue at the same place within the image volume. The plans were generated using the same plan parameters.

4 Results

This chapter presents the results after analysing the files generated as explained in chapter 3.

4.1 Shape

The influence of body shape on the dosimetric impact from displacement was tested (section 3.5.1). Figure 4.1 shows D_{95} dose difference relative to the reference case as a function of displacement. Each dot along the displacement represents the mean D_{95} relative dose difference for the six sets of plans for each case, and includes the standard deviations as error bars. The D_{95} data used to generate the plot are found in appendix B. MU values characterising the six reference plan for each case are found in appendix E. There is a good correlation between all three phantoms when introducing displacement in the positive x-direction. The spherical phantom and the pelvis phantom are in compliance for negative displacements, while the NEMA IQ phantom shows a better target coverage than the respective two. This difference was found statistically significant for displacements in the negative x-direction (p-value < 0.05, Mann-Whitney U-test theory 2.4). Larger variances between the six measurements are found for larger displacements (fig. 4.1). The red dotted line marks when D_{95} has decreased by 5% compared to the reference case, which is deemed the limit of clinical acceptance (theory 2.1.3). Hence, translational distortions above 2 mm are clinically unacceptable according to these results.

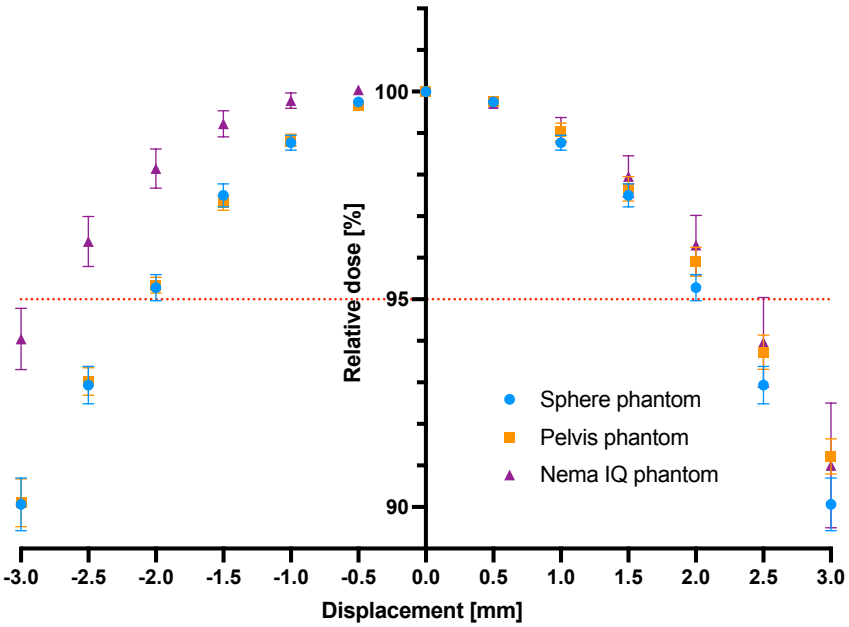

Figure 4.1: Relative D_{95} dose difference for displacement cases as compared to the reference case. Three distinct phantoms, spherical phantom, pelvis phantom, and NEMA IQ phantom, have been utilised. The figure shows the mean values with corresponding standard deviations for six measurements performed after generating six distinct treatment plans for each phantom.

The dosimetric influence of displacement may depend on the quality of the reference plan. Figure 4.2 shows

the DVHs (theory 2.1.3) for one reference plan for each of the phantoms. Only one reference plan for each phantom was chosen for visualisation because the other five plans were approximately identical. The spherical and pelvis phantom plans better resembles a step function than the NEMA IQ phantom (fig. 4.2) (theory 2.1.3). Thus, these reference plans are better. Note that the x-axis is truncated to [1.0, 2.2] Gy to highlight this difference.

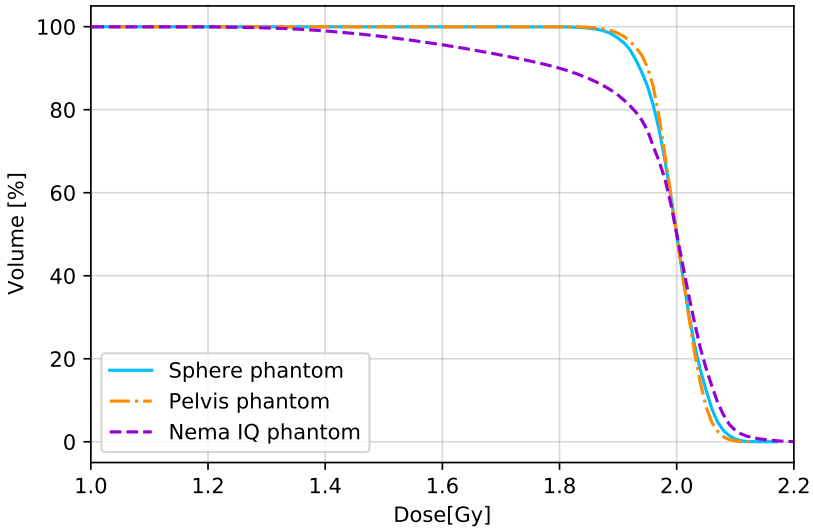

Figure 4.2: DVHs for plans generated with a 22 mm spherical PTV in the spherical phantom, pelvis phantom and the NEMA IQ phantom. The x-axis (doses) is truncated to [1.0, 2.2] Gy for clarity.

The dose spill (theory 2.1.4) is seen in figure 4.3. It shows less dose spill for the spherical phantom case with a statistically significant difference (p-value < 0.05, Mann-Whitney U-test). The dose spill for the NEMA IQ phantom and the pelvis phantom are similar and within each other's error bars. The dose spill increases as the displacement increases.

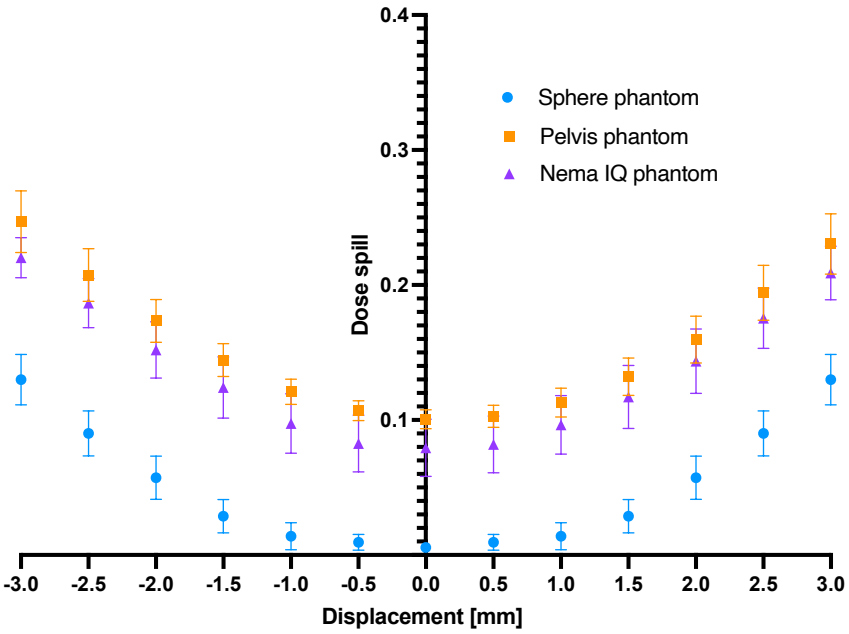

Figure 4.3: Dose spill as a function of displacement for treatment plans generated for the spherical phantom, pelvis phantom and NEMA IQ phantom.

The CI (section 2.1.4) is seen in figure 4.4. CI generally decreases when the displacement increases except for small displacements in the positive x-direction for the pelvis phantom. The difference between the pelvis phantom and the spherical phantom was found statistically significant for all displacements (p-value < 0.05, Mann-Whitney U-test). Furthermore, the NEMA IQ phantom was found statistically different for displacements from -1 mm to 3 mm and -3 mm to -1.5 mm compared to the pelvis phantom and spherical phantom respectively (p-value < 0.05, Mann-Whitney U-test) .

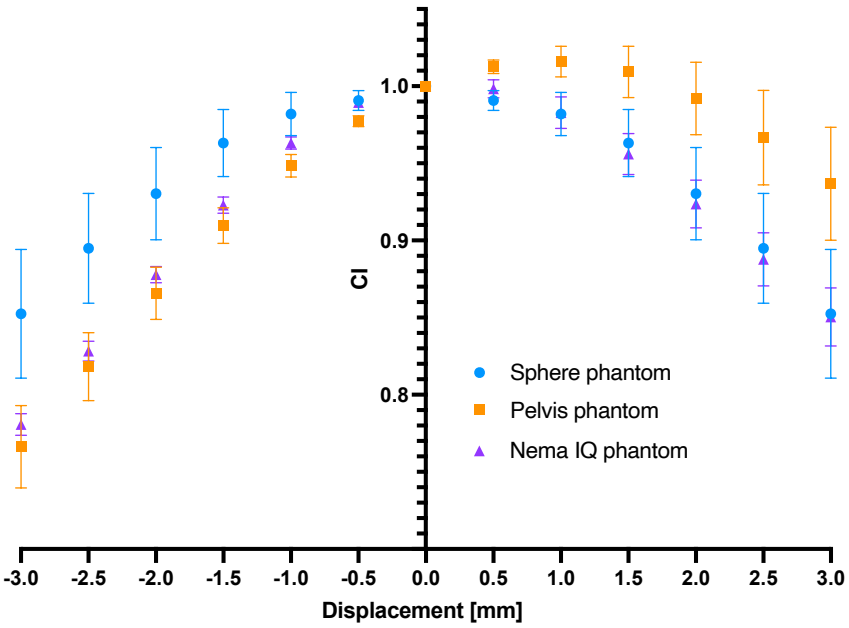

Figure 4.4: CI as a function of displacement for the spherical phantom, pelvis phantom and NEMA IQ phantom plans.

4.2 PTV size

The influence of PTV's size was investigated (section 3.5.2). Figure 4.5 shows relative D_{95} dose difference compared to the reference plans for each cases of PTV size. The figure shows the means and corresponding standard deviations from the six measurements. A larger dose difference, i.e., lower D_{95}, per displacement was found for smaller PTV. The difference between the two larger PTVs compared to the two smaller was found statistically significant (p-value < 0.05, Mann-Whitney U-test). The red dotted line marks when D_{95} has decreased by 5% compared to the reference case.

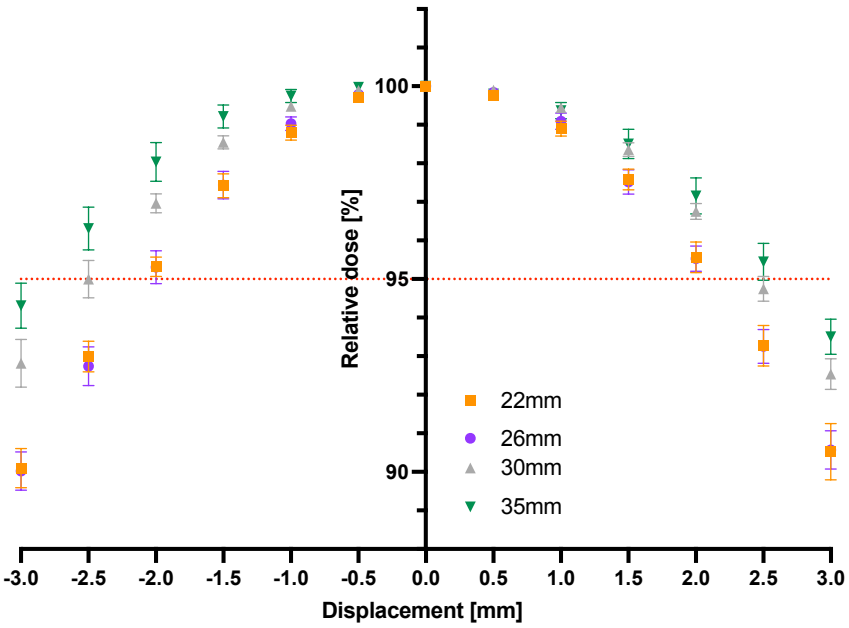

Figure 4.5: Difference in D_{95} as a function of displacement compared to the reference case. Every dot represents the mean of six distinct plans for each case with the corresponding standard deviation. The PTV sizes were 22, 26, 30, and 35 mm.

The DVHs from one reference plan for each PTV sizes are shown in figure 4.6. The figure shows that the plans created with the largest PTVs are better than the 22 mm PTV . Note that the x-axis is truncated to [1.8, 2.1] Gy to highlight this difference.

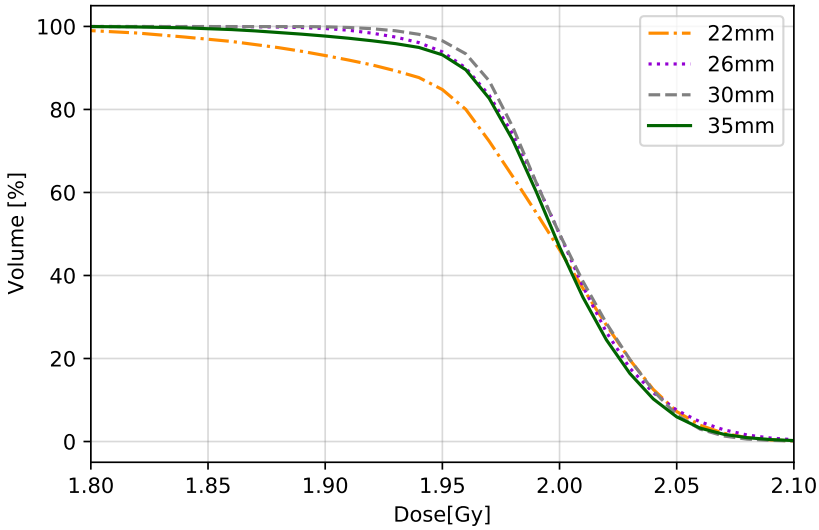

Figure 4.6: DVHs for the reference plans with four different sizes of PTV. The PTVs' diameters were 22, 26, 30 and 35 mm. The x-axis (doses) is truncated to [1.8, 2.1] Gy for clarity.

The dose spill as a function of displacement is shown in figure 4.7. The lowest dose spill is found for the largest PTV of 35 mm. The largest dose spill is found for the two smallest PTVs. The difference was found statistically significant (p-value < 0.05 , Mann-Whitney U-test). The lower dose spill for the largest volume does not necessarily mean that less normal tissue is being damaged. The volume of the dose spill may still be greater illustrated by figure 4.8. It shows coherence between the volume of the spilled dose and the target size with largest dose spill volume for largest target per displacement.

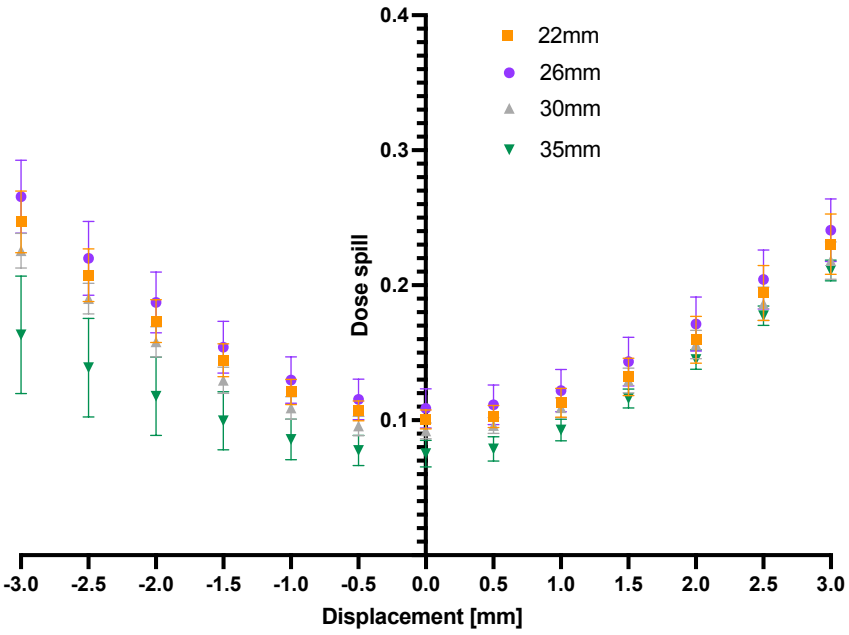

Figure 4.7: Dose spill as a function of displacement for plans created with four different PTV sizes. The PTV sizes were 22, 26, 30 and 35 mm.

Figure 4.9 shows CI as a function of displacement for the four different PTV sizes. The variations within plans created with the same PTV size, and between the different sizes, increases as the displacement increases. Furthermore, CI decreases as the displacement increases. The smaller PTVs favours displacements in the positive x-direction according to CI. Difference in CI was found statistically significant between all PTV sizes for several displacements (p-value < 0.05, Mann-Whitney U-test).

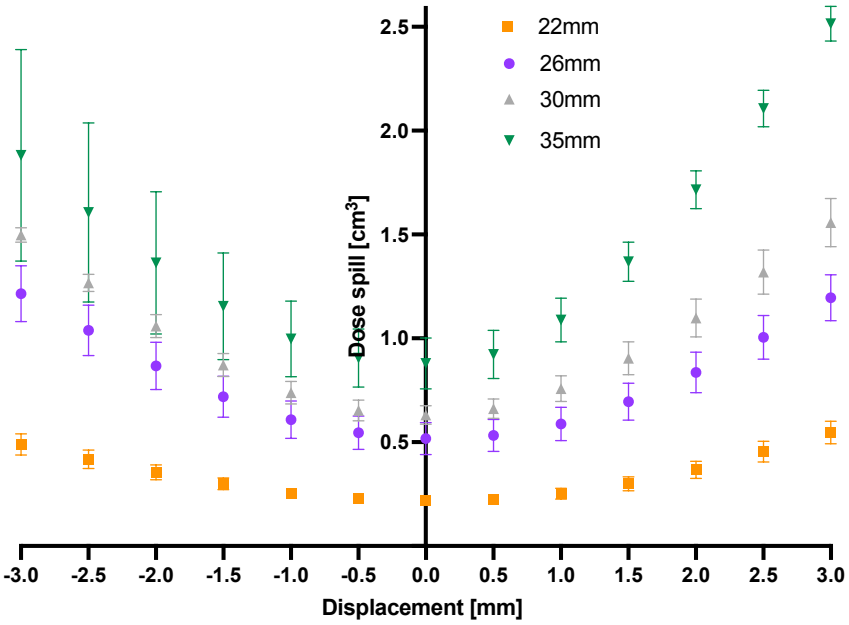

Figure 4.8: Dose spill volume as a function of displacement for plans created with four different PTV sizes. The PTV sizes were 22, 26, 30 and 35 mm.

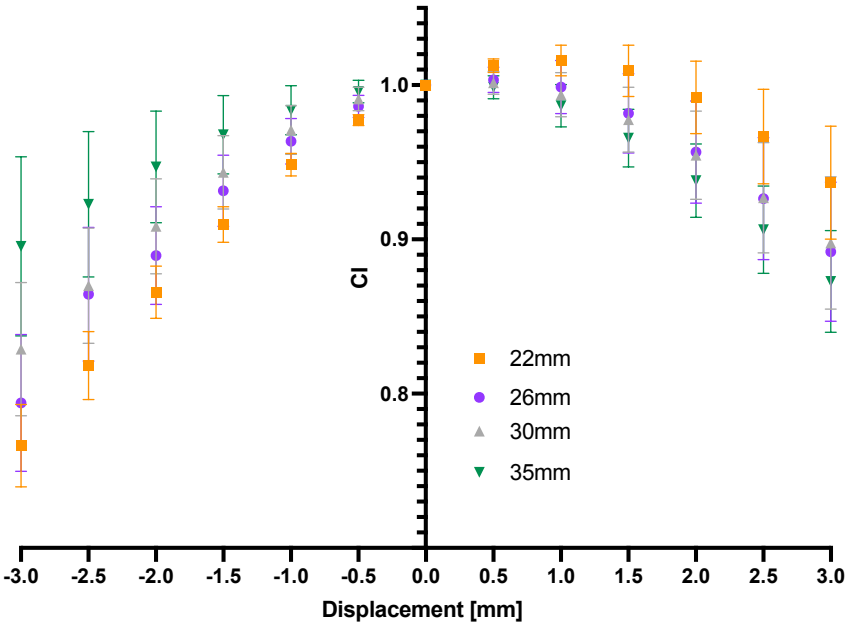

Figure 4.9: CI as a function of displacement for plans created with four different PTV sizes. The PTV sizes were 22, 26, 30 and 35 mm.

4.3 PTV position

PTV positions' influence on dosimetric impact from geometric displacement was investigated (section 3.5.3). PTVs were positioned in the centre and 3 cm, 6 cm, and 9 cm from the centre of the pelvis phantom. Figure 4.10 shows the relative difference in D_{95} for each displacement compared to the reference case. The red dotted line marks a 5% reduction in D_{95}. The points represent the means with corresponding standard deviations from the six measurements performed for each case. Insignificant change in dosimetric impact from PTV's position is observed as the means are similar and within each others error bars (fig. 4.10). Larger than 2 mm translational geometric distortions were found clinically unacceptable. The difference between the centre PTV and the other positions were found statistically significant for displacements above 1 mm in the positive x-direction (p-value < 0.05, Mann-Whitney U-test). Furthermore, a statistically significant difference was found for negative displacements above 0.5 mm comparing the 9 cm PTV position to the centre position.

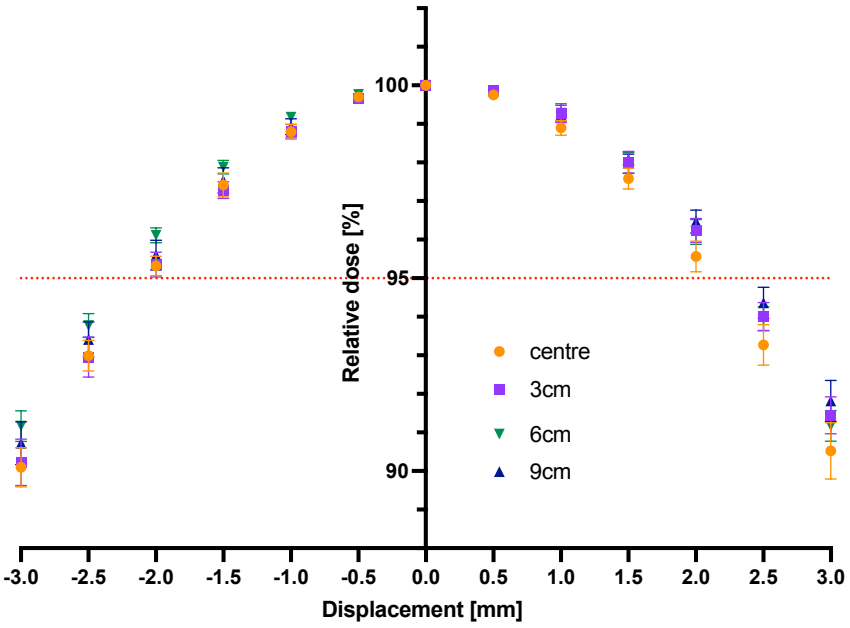

Figure 4.10: Relative D_{95} dose difference for displacement cases compared to the reference case. The figure shows the mean with the corresponding standard deviation for six measurements performed after generating six distinct treatment plans for each PTV position. Four different PTV positions within the same phantom was tested.

Figure 4.11 shows the DVHs for the reference case from one plan for each PTV position. The figure shows approximately no difference in DVHs.

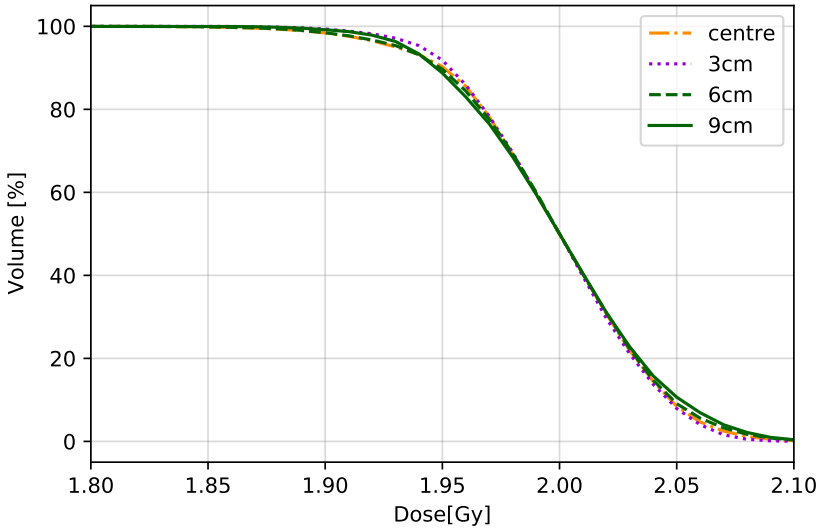

Figure 4.11: DVHs for four plans generated by the TPS. The four plans are generated for the same PTV positioned at different positions within the phantom. The plan labelled centre has PTV positioned approximately in the centre of the phantom. The 3 cm, 6 cm and 9 cm plans have PTV positioned 3, 6 and 9 cm from the centre along the positive x-direction in the phantom. The x-axis (doses) is truncated to [1.8, 2.1] Gy for clarity.

Figure 4.12 shows the dose spill as a function of displacement. Dose spill increases as the displacement increases. There are some differences in dose spill depending on PTV's position. However, the means are within each other's error bars.

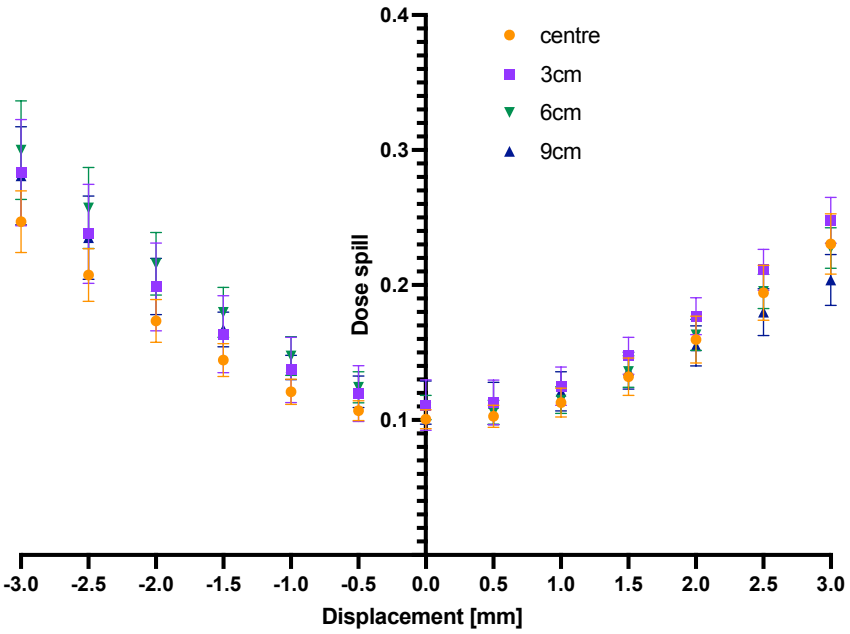

Figure 4.12: Dose spill as a function of displacement for different PTV positions. PTV was positioned in the centre of the phantom and 3 cm, 6 cm and 9 cm in the positive x-direction.

CI as a function of displacement for different PTV positions is shown in figure 4.13. The largest CI is found for 6 cm and 9 cm PTV positions for displacements in the positive x-direction. The lowest CI is found for the same PTVs in the negative x-direction. The difference between these PTV positions and the centre position was found statistically significant (p-value < 0.05, Mann-Whitney U-test). Furthermore, a statistically significant difference was found for the 3 cm PTV position for all displacements in the negative direction (p-value < 0.05, Mann-Whitney U-test).

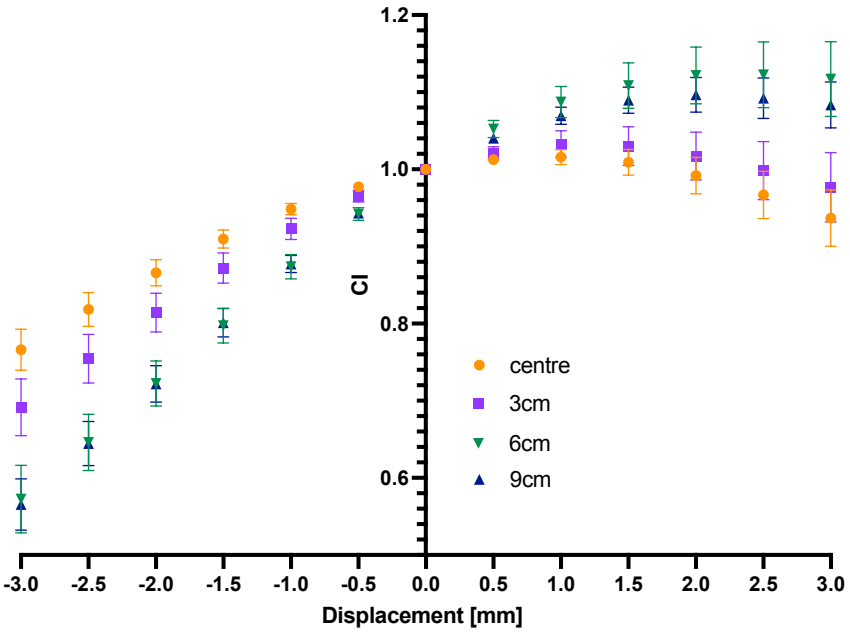

Figure 4.13: CI as a function of displacement for PTV position at the phantom's centre, and 3 cm, 6 cm and 9 cm in the positive x-direction from the centre.

4.4 Energy

Photon energy's influence on the dosimetric impact from geometric displacements were investigated (section 3.5.4). Figure 4.14 shows the relative change in D_{95} compared to the reference plan. The dots represents the mean of six measurements for each energy with corresponding standard deviations. There is little influence from photon energy on the dosimetric impact from translational geometric distortions. However, the difference was found statistically significant for displacement in the positive x-direction (p-value < 0.05 Mann-Whitney U-test).

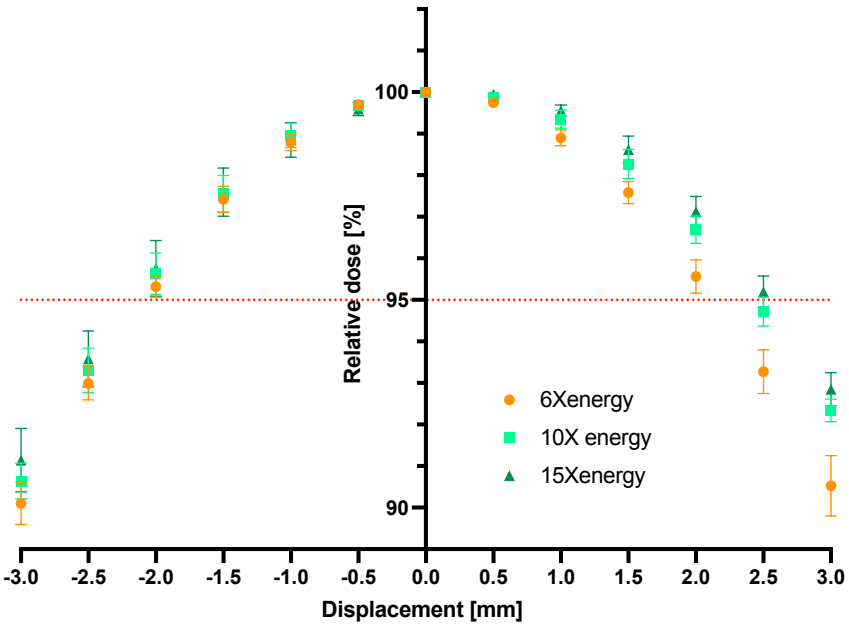

Figure 4.14: Relative D_{95} dose difference for displacement cases as compared to the reference cases. The figure shows the mean with corresponding standard deviation for six measurements for each energy. Three photon energies were investigated using the same phantom, PTV and plan parameters.

Figure 4.15 shows the DVHs for each energy case. The DVHs coincide.

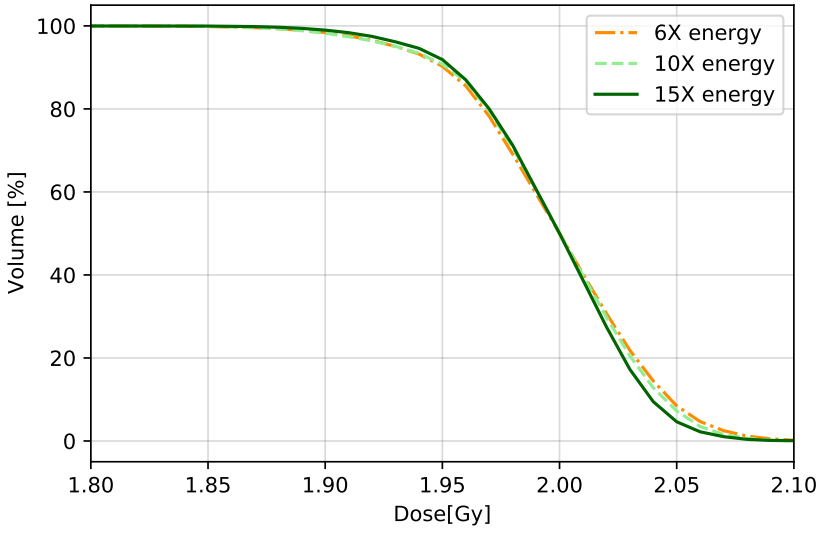

Figure 4.15: DVHs for three plans generated for the same phantom, PTV and plan parameters, but with three different photons energies. The x-axis (doses) is truncated to [1.8, 2.1] Gy for clarity.

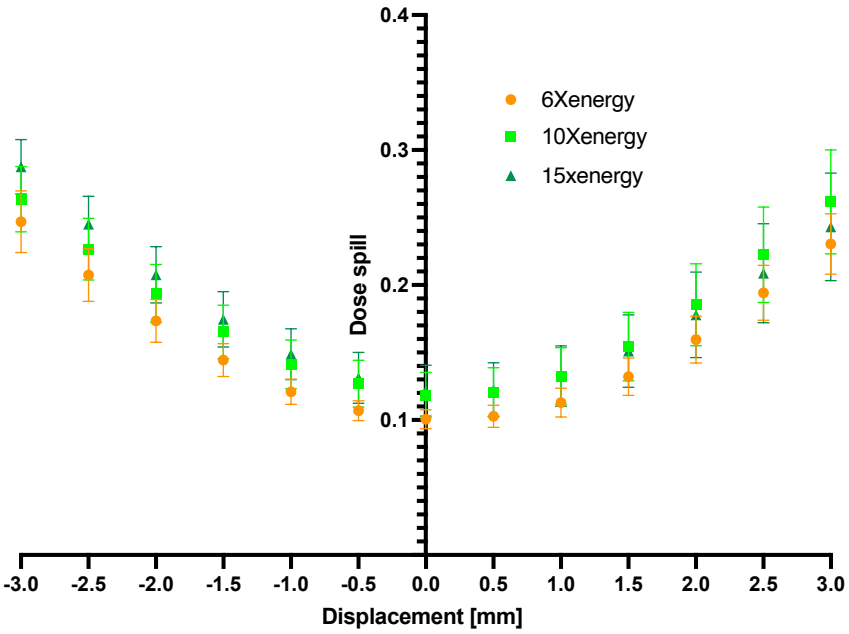

Figure 4.16: The dose spill as a function of displacement for treatment plans optimised using 6, 10 and 15 MV photons. Six plans were made for every energy, and the dots represent the mean with the corresponding standard error.

There is little difference between dose spill for the different energies as the mean dose spill for each energy is mostly within the standard errors of the other (fig. 4.16). The dose spill increases as the displacement increases. A statistically significant difference was found between 6 MV energy and 15 MV energy for displacements in the negative direction (p-value < 0.05 Mann-Whitney U-test).

CI as a function of displacement for the energy case is shown in figure 4.17. The largest CI is found for displacements in the positive x-direction. There are some variations in CI for the different energies and a statistically significant difference was found between the 6 MV and 10 MV energies (p-value < 0.05 Mann-Whitney U-test).

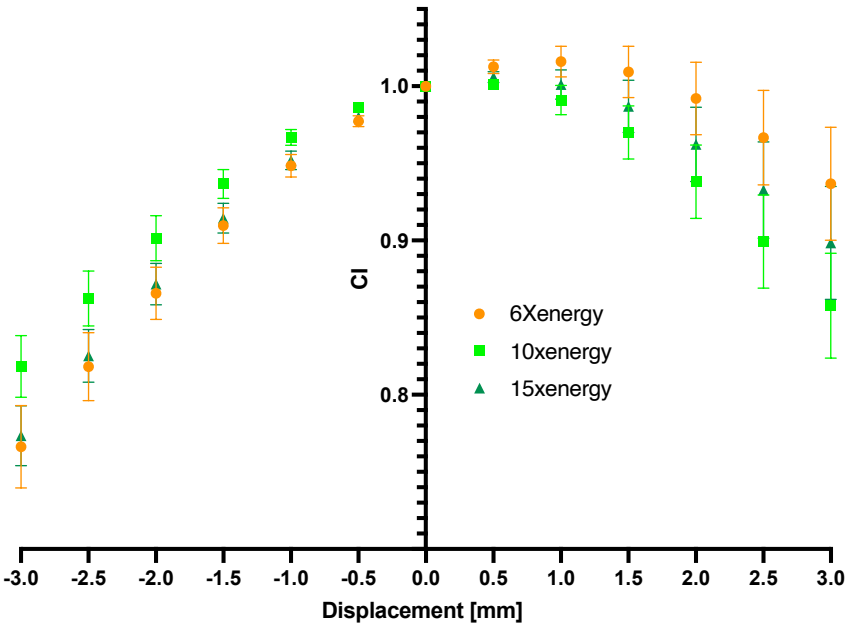

Figure 4.17: CI as a function of displacement for VMAT treatment plans generated using 6, 10 and 15 MV photons.

4.5 Tissue density

Treatment plans were generated when PTV was positioned in three different tissues, compact tissue (bone), lung tissue and soft tissue (section 3.5.5). Figure 4.18 shows relative D_{95} compared to the reference plans. Little variations in D_{95} are found, although the difference was found statistically significant for bone compared to soft tissue for displacements larger than 0.5 mm in both directions (p-value<0.05, Mann-Whitney U-test).

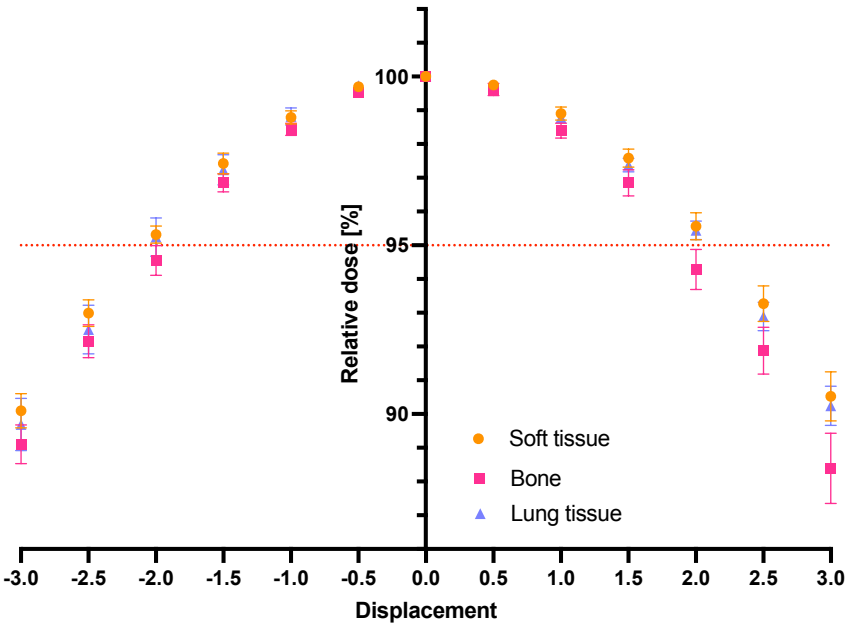

Figure 4.18: Relative D_{95} dose difference for displacement cases as compared to the reference cases. Reference plans were optimised for the same PTV size but composed of different tissue densities. Soft tissue equivalent, lung tissue equivalent and bone equivalent material were tested. The figure shows the mean with corresponding standard deviation for six measurements performed after generating six distinct treatment plans for each tissue case.

DVHs for one reference plan for the different PTV compositions is shown in figure 4.19. It shows the best plan quality for the soft tissue case and the worst plan quality for the lung case if only considering the DVHs.

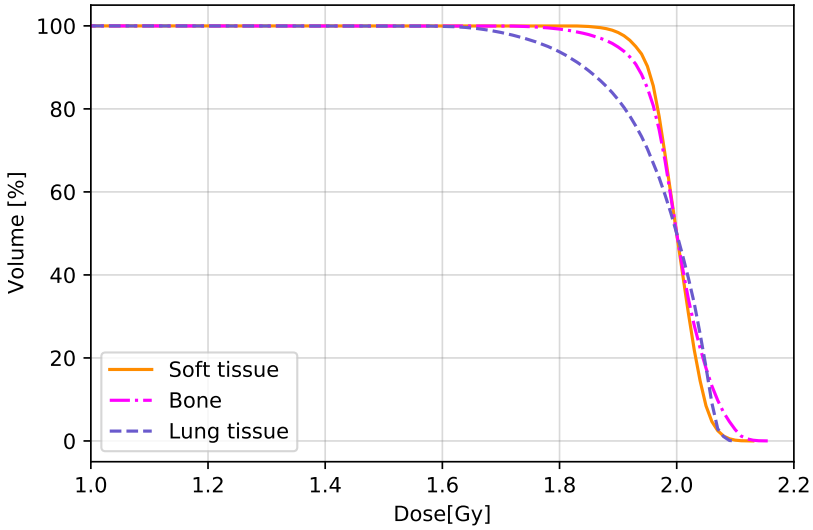

Figure 4.19: DVHs for three different plans optimised for the same PTV comprised of different tissue. The x-axis (doses) is truncated to [1.0, 2.2] Gy for clarity.

Figure 4.20 shows the dose spill as a function of displacement. The largest dose spill is found for the soft tissue cases and the smallest for the lung tissue cases. The difference was found statistically significant (p-value < 0.05, Mann-Whitney U-test). The dose spill increases as the displacement increases.

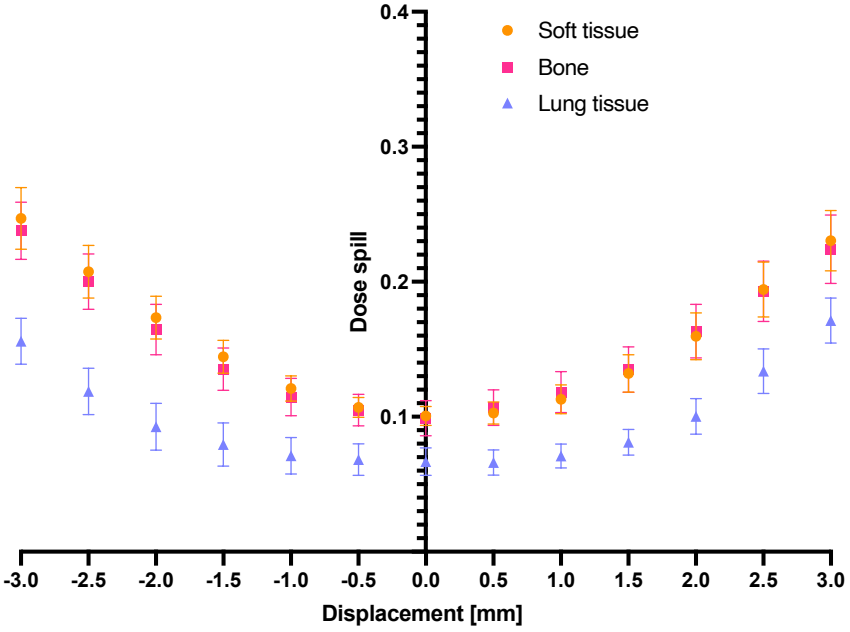

Figure 4.20: Dose spill as a function of displacement for PTV comprised of soft tissue, bone and lung tissue.

Figure 4.21 shows the CI as a function of displacement for the tissue investigations. CI is generally higher for the six lung tissue plans with little variations between them. This difference was found statistically significant (p-value < 0.05, Mann-Whitney U-test). The highest conformity is found for the soft tissue cases for displacements in the positive x-direction. Furthermore, the lowest conformity is found for displacement in the negative x-direction for the soft tissue cases. The difference in CI for bone compared to soft tissue was also found statistically significant (p-value < 0.05, Mann-Whitney U-test).

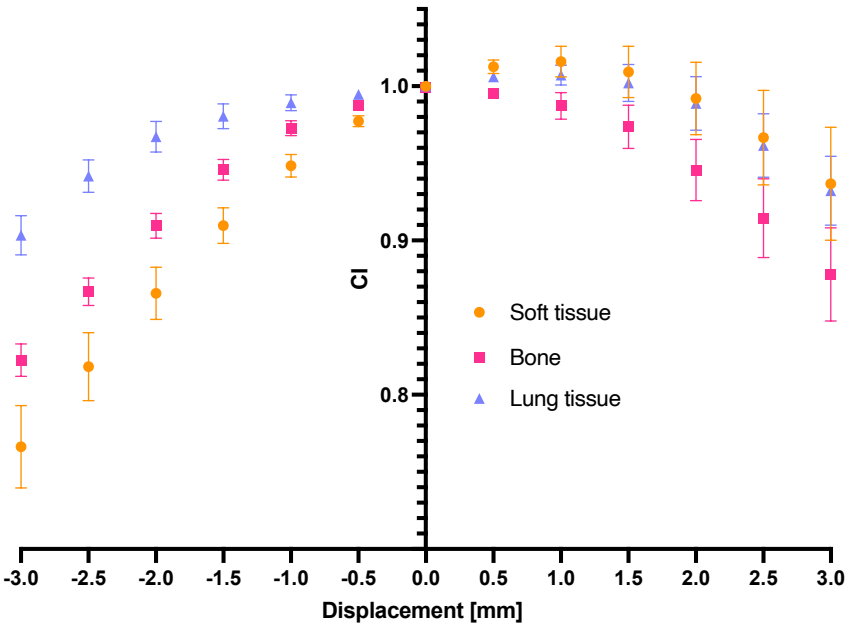

Figure 4.21: CI as a function of displacement for PTV comprised of soft tissue, bone and lung tissue.

4.6 Patient case

Four different PTV sizes were investigated for the patient case (section 3.5.6). Figure 4.22 clearly shows better target coverage per displacement for the largest PTV. Furthermore, it shows worse target coverage for smaller PTV sizes. The difference was found statistically significant (p-value < 0.05, Mann-Whitney U-test). The clinically acceptable displacement is around 2 mm for all cases, although a little less for the 22 mm PTV and a bit more for 35 mm. The target coverage decreases as the displacement increases.

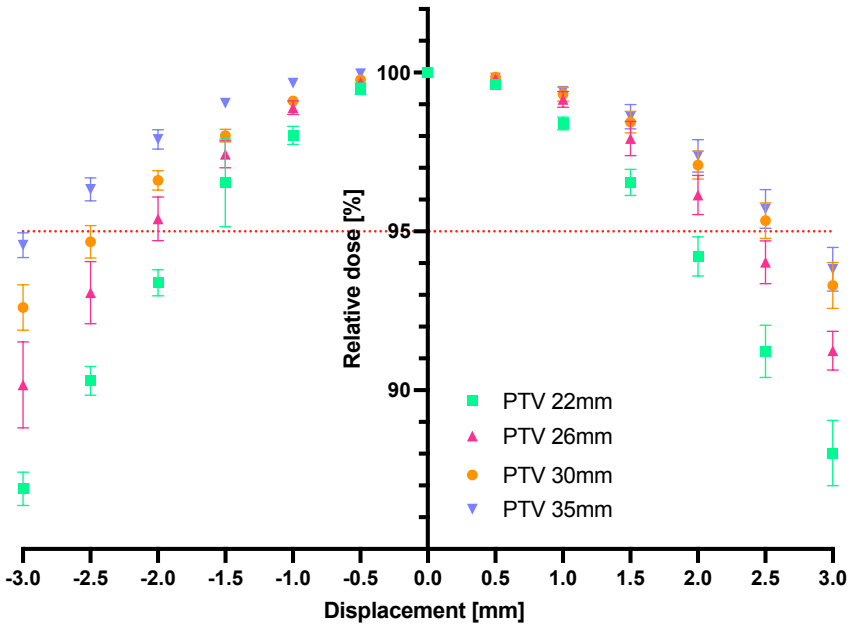

Figure 4.22: Difference in D_{95} as a function of displacement compared to the reference case. The figure shows the mean and corresponding standard deviation from six different measurements for each case. The PTV sizes utilised were 22, 26, 30, and 35 mm on a patient image of the pelvic region.

Figure 4.23 shows a better reference plan for larger PTV sizes. The quality of the treatment plan increases as PTV's size increases.

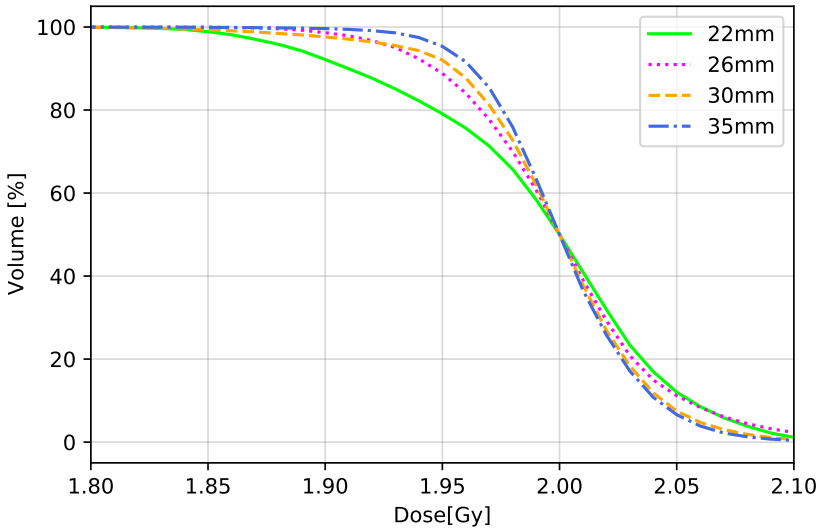

Figure 4.23: DVHs for PTV sizes of 22, 26, 30 and 35 mm. The DVHs are generated from plans optimised with the same parameters, except for the target size. The images are synthetically created CT images created from MRI of this author. The x-axis (doses) is truncated to [1.8, 2.1] Gy for clarity.

The dose spill as a function of displacement is shown in figure 4.24. The lowest dose spill is found for the 22 mm PTVs and the largest dose spill is found for 30 mm PTVs. The difference between 22 mm PTVs and the others was statistically significant for several displacements in the positive x-direction (p-value < 0.05, Mann-Whitney U-test). However, the dose spill is similar and the error bars overlap.

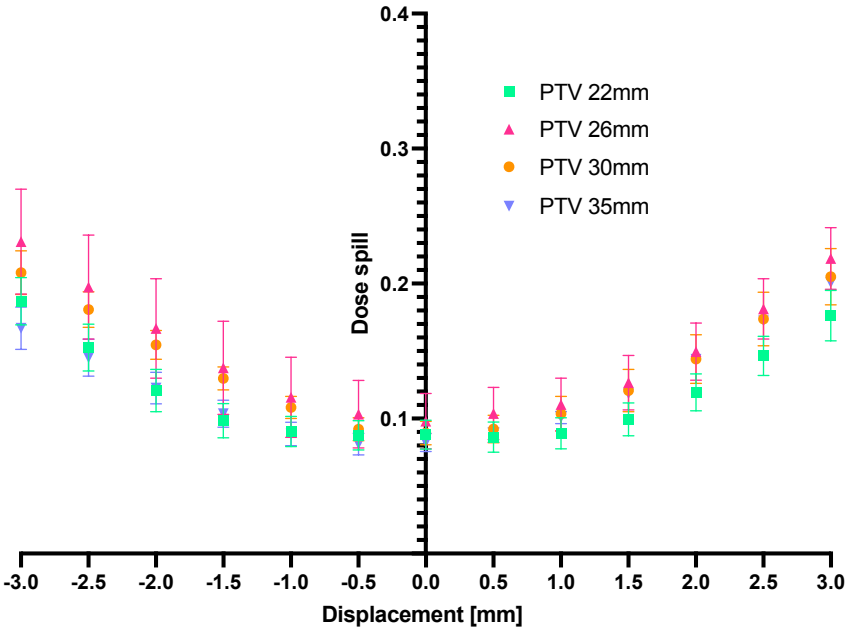

Figure 4.24: Dose spill as a function of displacement for four different PTV sizes. The images used are patient images of the pelvic region. The plans were optimised using the same criteria and plan parameters.

The dose spill volume as a function of displacement is shown in figure 4.25. The dose spill volume is larger for larger targets and increases with displacement.
The CI as a function of displacement for plans optimised with four different PTVs is shown in figure 4.26. The CI is higher for displacements in the negative x-direction and for the smallest PTVs.

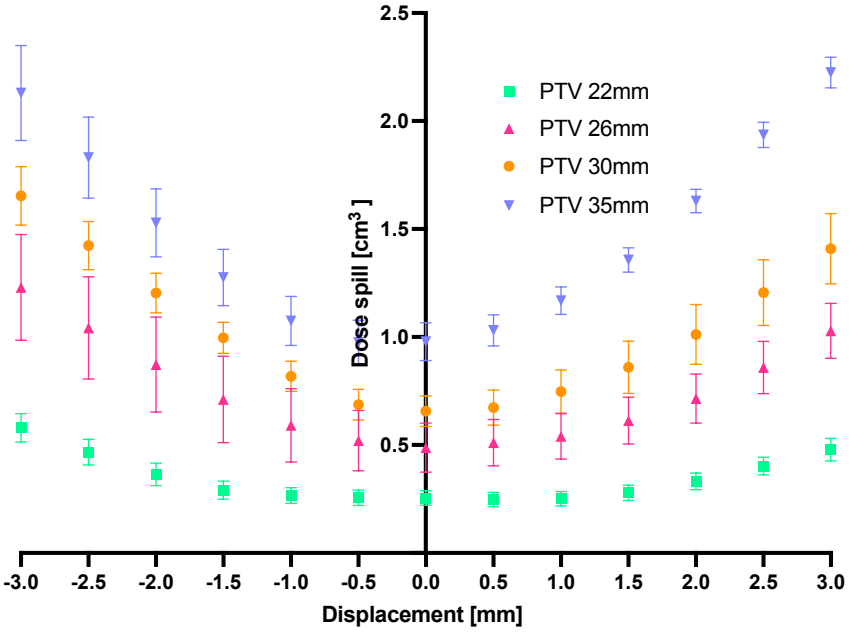

Figure 4.25: Dose spill volume as a function of displacement for plans created for four different PTV sizes. The PTV sizes were 22, 26, 30 and 35 mm.

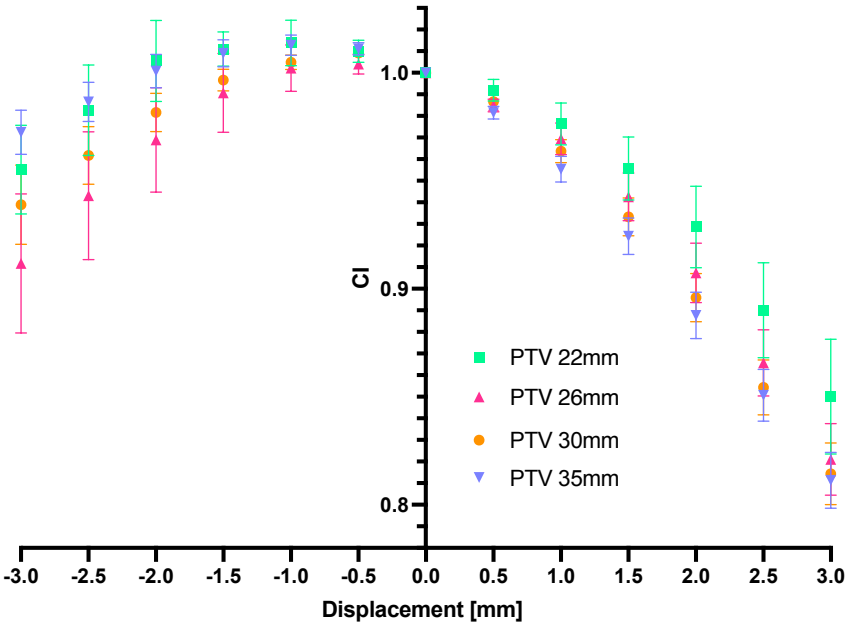

Figure 4.26: CI as a function of displacement. Three different plans were generated for each case of four PTV sizes. The plans were generated using patient images of the pelvic region.

The relative D_{95} dose difference between the phantom study (section 3.5.2) and patient study (section 3.5.6) for each PTV size is seen in figure 4.27. The dose differences are below 0.5 % for the three largest PTVs and the difference do not increase with displacement. Up to 1.8% dose difference are found between the patient

study and phantom study for the smallest PTV. Furthermore, the dose difference increases with displacement.

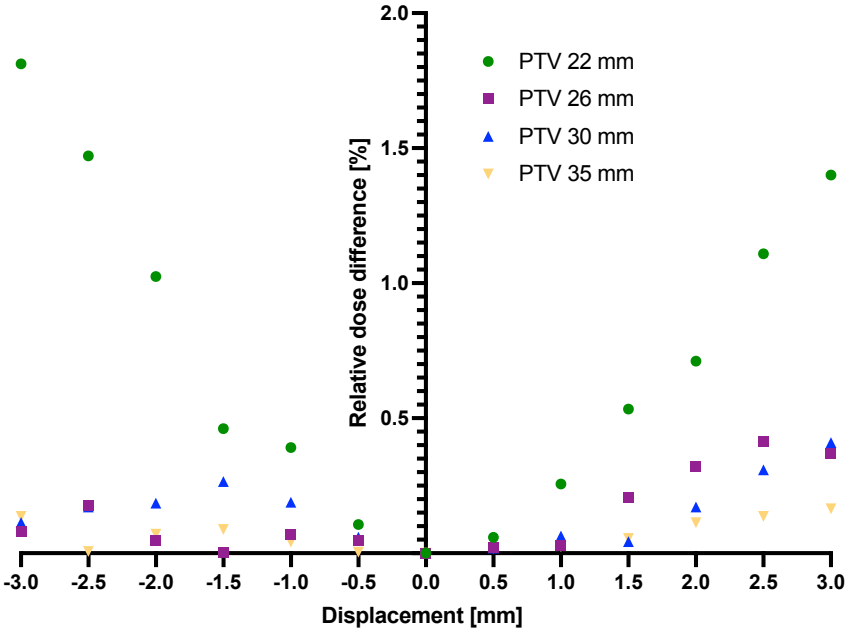

Figure 4.27: Relative percent dose difference as a function of displacement between the phantom and patient case for each PTV size.

5 Discussion

This project aimed to quantify the influence of translational geometric distortions on dose planning in RT. The tolerable limit of geometric distortion in MRI-only RT was investigated.

Several studies have determined the dosimetric effect from geometric distortions on RT treatment at different anatomical sites, as mentioned in the introduction (section 1). These studies have primarily been based on clinical cases using patient images [36]. Thus, their results may not apply to other anatomical sites. This thesis presents a quantitative assessment of the dosimetric effect from geometric distortions irrespective of anatomical region. Phantom images (fig. 3.1, 3.2 and 3.3) were used to ensure reproducible results. Furthermore, phantom images are simpler than patient images making it easier to isolate each parameter's influence on the dosimetric effect from geometric distortions. For validation, the phantom results were tested on a patient case. The parameters investigated were explained in the method (section 3.5). The method was constructed to produce results solely affected by uncertainties from translational geometric distortions. Thus other uncertainties pertaining to the treatment planning process, e.g., treatment delivery uncertainties, patient motion, delineation uncertainties and uncertainties related to sCT generation, are not included. Siemens Healthineers [33] concluded with minimal dosimetric errors (<1%) between sCT images and regular planning CT images for both head and pelvic region (theory 2.3.3). Therefore, dosimetric errors related to sCT generation are assumed minor. Treatment delivery uncertainties and patient motion may be present regardless of whether the treatment planning is based on MRI-only, CT-only or both. The main difference between these planning processes are uncertainties related to geometric distortions (MRI-only), target delineation (CT-only), and image co-registration (both). Note that uncertainties related to target delineation are an issue in MRI-only as well, but they are often reduced compared to CT-only because of the improved soft-tissue contrast. As an example, studies have shown an increased target delineation accuracy by co-registering CT with MRI for prostate cancer patients [37]. The results have enabled fraction escalation while maintaining the dose to critical structures. Thus, uncertainties related to target delineation decreased. However, co-registration errors were found up to 3 mm for prostate cancer patients [38]. If the expected geometric distortions are below 3 mm, the prostate is an area that may benefit from an MRI-only workflow. Furthermore, if the geometric distortion errors are similar to the co-registration errors, these patients may still benefit from an MRI-only workflow as the process is less exhausting for the patient. In addition, MRI-only is also potentially more efficient for the clinic. Studies have shown geometric distortions below 1 mm for prostate cancer [39] and little dose difference between distorted and undistorted images [2]. Therefore an MRI-only workflow has been implemented for prostate cancer at several clinics around the world [40]. However if the expected geometric distortions are beyond a tolerable limit, an MRI only workflow is not beneficial. This tolerable limit is a topic of discussion in this thesis.

5.1 Parameter selection

D_{95} (theory 2.1.3), dose spill and CI (theory 2.1.4) were parameters chosen to investigate the dosimetric impact. D_{95} is the most used parameter when evaluating target coverage in treatment planning at UNN. Furthermore D_{95} is also recommended by ICRU and the Norwegian Radiation Protection Authority along

with other volume doses such as D_{50} and D_2 (theory 2.1.3). These parameters were investigated for the project paper [7]. No significant dose differences were found by evaluating D_{50} and D_2. D_{95} was deemed the most relevant parameter as it describes the overall target coverage while the other two describe the dose covering only parts of the target. Mean dose to PTV and gamma evaluation were also investigated during the project paper [7]. D_{mean} was found to be less sensitive to geometric distortions than near-minimum dose and did not contribute any extra useful information. Therefore, the mean dose was not chosen for investigation in this thesis. Gamma evaluation was a time-consuming process. The script searches iteratively through the large dose matrix as explained in the project paper [7]. Evaluating 1326 files would therefore be too comprehensive. Furthermore, the clinic commonly uses the gamma function to validate that the planned dose is similar to the delivered dose. Thus, it comprises several treatment uncertainties. Applying gamma criteria to investigate dose differences solely due to geometric distortions may result in clinically acceptable plans that would not be acceptable after including treatment delivery uncertainties. Therefore, Gamma evaluation was not chosen to investigate the dosimetric impact of translational geometric distortions in this thesis.

Radiotherapy is a compromise between delivering a sufficient dose to the tumour and sparing normal tissue (theory 2.1.2). Dose spill (theory 2.1.4), defined as the portion of 2 Gy isodose outside of PTV, was therefore chosen to visualise how the dose delivered to normal tissue changes with translational geometric distortions. One would expect it to increase as the displacement increases. Note, however, that the dose spill, as defined in this thesis, does not indicate the volume of dose outside the target. Hence, care should be taken when interpreting the results. Closely related to the dose spill is CI (theory 2.1.4). It is a measure of target coverage but is differentiated from D_{95} as it is a measure of the portion of the prescribed 2 Gy isodose covering the target. It is commonly used as a measure of plan quality, although DVHs are superior for this purpose in the clinic (theory 2.1.3). Therefore, D_{95} has been the most important parameter when evaluating the dosimetric effect of translational geometric distortions in the target. However, CI may provide additional information about the plan and is therefore also included in this thesis.

Translational geometric distortions up to 3 mm were investigated (section 3). Larger distortions may occur [28], and together with other uncertainties in treatment delivery, concerns may be raised if larger distortions should have been investigated. However, as stated above, the aim was to determine a general tolerance limit of translational geometric distortions. The project paper suggested a limit of 2 mm translational distortions from one simple phantom measurement [7]. Thus, larger distortions leading to severe loss in target coverage were not of interest and deemed unacceptable. Furthermore, the expected geometric distortions at two different MRIs at UNN were investigated in a separate project during the spring of 2022 [41]. Different MRI sequences commonly used in RT were investigated. The results showed geometric distortions less than 2 mm for most sequences. Therefore, distortions up to 3 mm were considered most relevant. In cases where the distortions are large, an MRI-only workflow may not be possible. Further work could then focus on reducing the geometric distortions by further development of correction methods on the MRI scanner, adapting the FOV or choosing a different MRI sequence [40].

5.2 Statistical considerations

Six plans for each case were created to produce statistical results. For good statistics, more plans should have been created. However, it was a time-consuming process. The dose optimisation algorithm searches for a global minimum of the objective function, based on the criteria set, to produce the best treatment plan (theory 2.1.2). Utilising the same optimisation criteria for the same case often resulted in the same treatment plan characterised by equal MU values (theory 2.1.2). Several optimisation attempts were needed to produce six different plans. The more plans created, the more attempts were necessary to produce a new distinct plan. The mean difference in D_{95} for the sphere, pelvis and NEMA IQ phantoms (section 3.5.1) when using 6 plans compared to 5 was calculated and found to be 0.03%, 0.03% and 0.06%, respectively (Data accessible: appendix B). We can assume that the difference between analysing 7 plans compared to 6 plans is even less. Six plans were therefore assumed sufficient to produce credible results. The results from the statistical test, Mann-Whitney U-test, may however be affected by the small sample size. A larger sample size gives greater statistical power [34]. The Mann-Whitney U-test ranks the measurements independent of the case they belonged to before calculating the mean of the ranks (theory 2.4). Therefore, the relative difference between the measurements may be tiny, but if all the six measurements from one case are lower than those from the other case, the p-value will be below 0.05.

5.3 Shape

Three phantoms were used to test the influence of body shape on the effect of translational geometric distortions (fig. 3.1, 3.2 and 3.3). The spherical phantom is the simplest and may isolate the effect of translational geometric distortions from other factors. The pelvis phantom is similar in size to the spherical phantom but has a more realistic shape and a simulated spine, making it more advanced. The NEMA IQ phantom's shape is similar to the pelvis phantom but comprises a lung insert instead of bone and is larger than the pelvis phantom. Hence, these phantoms were chosen because of their composition, shape, and size difference. Note, however, they are still phantoms and quite simple compared to the human body. Hence, if the dosimetric effect from translational geometric distortions varies greatly between these phantoms, a general quantitative determination of the influence of geometric distortions may be difficult to find. The same arc and PTV was used to generate the reference plans (section 3.5.1). To minimise the influence of other parameters, PTV was positioned approximately in the centre of the body for both the spherical water phantom and the pelvis phantom. In the NEMA IQ phantom, PTV was positioned in the 22 mm hollow glass sphere because of the lung insert in the centre of the phantom. This may influence the results. However, both the PTV position and PTV tissue difference have been tested and will be independently discussed (section 5.5 and 5.7).

PTV's size was chosen to be 22 mm in diameter which is a typical size of cerebral stereotaxis [4]. The standard treatment for this cancer type is stereotactic radiotherapy relying on MRI for precise tumour localisation [42]. Furthermore, it is a typical size of T1 stage tumours [43]. Therefore, it is a very clinically relevant size. Small targets have been found to tolerate less distortions than larger targets [4]. A small target of 22 mm therefore provides a worst-case scenario. The influence of PTV's size have also been tested and

will be discussed later (section 5.4).

This section will discuss the results investigating the body shape's influence on the dosimetric impact of translational geometric distortions. The results comprise D_{95} evaluation (fig. 4.1) calculated from the DVHs (fig. 4.2), dose spill (fig. 4.3) and CI (fig. 4.4).

For displacements in the positive x-direction D_{95} decreased as the displacement increased for all phantoms (fig. 4.1). This is as expected, and in agreement with the results found in the project paper [7]. In addition, the standard errors increased with displacement. The standard errors indicate variations between the six plans for each case. Because the plans are different and have distinct radiation distributions, minor differences occurs. Some distributions may favour displacement in one direction which becomes more evident for larger displacements, resulting in the observed larger variations (fig. 4.1). The mean relative D_{95} per displacement for each phantom are within the other phantoms' standard error. As an example, for 3 mm displacement D_{95} was 90,8, 90,9 and 90,8 for one plan for the spherical phantom, pelvis phantom, and NEMA IQ phantom, respectively. Furthermore, the difference between the phantoms was not found statistically significant (section 4.1). The difference in D_{95} between the phantoms is also smaller for smaller displacement and the clinically acceptable limit was 2 mm (fig. 4.1).

For displacements in the negative x-direction, larger differences are observed (fig. 4.1). The pelvis phantom and spherical phantom seem to follow the same curve, but the NEMA IQ phantom has a greater D_{95}. An explanation may be the lung insert in the centre of the phantom. Moving the beam's isocentre in the negative x-direction moves the isocentre closer to the lung insert. From theory, a build-up is usually found behind lung tissue because the lung has lower electron density and thus fewer electrons for the photons to interact with (theory 2.1.1). The reference plan is optimised to take this build-up into account. However, when the isocentre is moved, the build-up is shifted. The result is the larger target coverage observed (fig. 4.1). Displacements up to 2.5 mm is clinically acceptable for negative displacements for the NEMA IQ phantom according to relative D_{95} values.

The dose spill (theory 2.1.4) is a measure of the portion of the 2 Gy isodose outside PTV. The dose spill (fig. 4.3) increased as the displacement increased and as the target coverage, D_{95}, decreased. When the target coverage decreases, more dose ends up outside PTV. The dose spill as a function of displacement is therefore as expected. However, the effect from the lung insert which resulted in the larger target coverage for the NEMA IQ phantom, is not observed on the dose spill. For this particular case, a lower dose spill for these displacements would be expected. However, the dose spill was symmetric around the reference plan and thus similar in both displacement directions (fig. 4.3). An explanation may be that both the total 2 Gy isodose and the 2 Gy isodose inside PTV are similarly affected by the lung insert. If so, one would expect a higher CI for negative displacements for the NEMA IQ phantom. This is because CI only depends on the 2 Gy isodose inside PTV (theory 2.1.4). However, CI was similar for the NEMA IQ phantom and pelvis phantom for negative displacements (fig. 4.4). Furthermore, CI was larger for displacements in the positive x-direction. Thus, the target coverage evaluated by D_{95} and CI are inconsistent.

The results suggest that evaluating target coverage based on CI and D_{95} produces different results. D_{95} is the parameter used in the clinic (theory 2.1.3) and indicates the overall target coverage and is therefore

the most important parameter to evaluate. CI shows how the 2 Gy isodose inside PTV is affected by displacements. Hence, it is a measure of how the higher doses are affected. It is not symmetric and indicates larger 2 Gy target coverage for displacements in the positive x-direction. Note that the spherical phantom's CI is symmetric, but this is because the spherical phantom was only evaluated in one direction and assumed isotropic because of its shape (section 3.2.1). However, CI seems to favour displacements in one direction as it depends on where the 2 Gy isodose is positioned in PTV in the reference plan. In retrospect, the spherical phantom should have been tested for negative displacements as well regarding CI. When considering D_{95}, the symmetric assumption is valid. Since the effect from the lung insert was not observable on the CIs, the results suggest that low doses are more affected by inhomogeneities.

The DVH (fig. 4.2) shows a worse reference plan for the NEMA IQ phantom, as it fails to resemble the desired step-function (theory 2.1.3) compared to the other two phantoms. However, the difference in D_{95} (fig. 4.1) and thus the target coverage seem to be unaffected. This suggests little influence of the reference treatment plan quality on the effect of translational geometric distortions. However, the treatment plan quality should be investigated further. The dose spill (fig.4.3) was lower for the spherical phantom case. It may result from the simplicity of the phantom, making it easy to generate a good treatment plan. Note that the DVH only shows dose in PTV and do not indicate the dose outside. Thus, the dose spill also needs to be included when determining the treatment plan quality. Therefore, the spherical phantom's reference plans have the best quality because of the DVH resembling the step-function and because of the low dose spill. The changes in dose spill as a function of displacement were approximately equal for the three phantoms indicating little influence of body shape and plan quality on the dosimetric effect from translational geometric distortions.

To summarise, the body shape does not influence the effect of translational geometric distortions indicated by both D_{95} and dose spill evaluations. CI was shown to favour displacements in one direction depending on the position of the 2 Gy isodose within the phantom. Hence, it should not solely be used to measure the dosimetric impact. However, it can contribute additional information about the reference plan and dose distribution within PTV. The results suggest that care should be taken close to inhomogeneities. Furthermore, the reference plan quality did not affect the dosimetric impact. 2 mm translational geometric distortions were found clinically acceptable for all phantoms. Although little influence of the body shape was found, the amount of distortions depends on the body shape. As an example a large FOV increases chemical shift artefacts (eq. (2.5). Furthermore, larger FOVs are more prone to system-induced distortions because the magnetic field's homogeneity decreases with increasing distance from the magnetic isocentre (theory 2.3.2). Thus, for obese patients, distortions above 2 mm may be expected and are therefore not suited for an MRI-only workflow [44]. In addition if the patient has metal implants, large distortions will be expected which may cause the distortions to increase above 2 mm. The expected distortions should be compared to the 2 mm clinical limit to determine if an MRI-only workflow is beneficial.

5.4 PTV size

Tumours are found in different sizes. As mentioned (section 5.3), the influence of geometric distortions has been found to increase as target size decreases [4]. To generally determine the dosimetric effect, different

PTV sizes were investigated (section 3.5.2). 22 mm PTVs were the smallest targets investigated. Smaller targets are difficult to irradiate without damaging healthy tissue due to photon's interaction in the body (theory 2.1.1) and the extent of the MLCs. Furthermore, most targets are larger after adding uncertainty margins. Therefore, smaller targets were not investigated and are not well suited for an MRI-only workflow. A PTV size of 22 mm therefore provides the worst-case scenario. Targets up to 35 mm were tested. Larger targets are expected to tolerate more distortions and were therefore not investigated.

This section discusses the influence from PTV's size based on D_{95} (fig. 4.5), DVHs (fig. 4.6), dose spill (fig. 4.7, 4.8) and CI (fig. 4.9).

D_{95} values (fig. 4.5) show better target coverage per displacement for larger PTVs. The clinically acceptable limit was 2 mm for the 22, 26 and 30 mm PTV and 2.5 mm for the 35 mm PTV. This was in agreement with previous studies [4]. A displacement affects larger targets less than smaller targets because the displacement is relatively smaller compared to the volume size. This is visualised in figure 5.1 showing how a) a large PTV and b) a small PTV is affected by the same displacement.

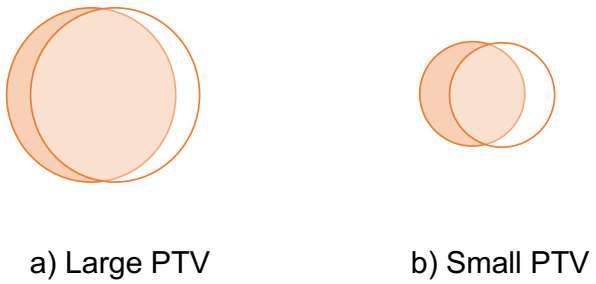

Figure 5.1: The target coverage, overlapping area, shown for a) a large PTV and b) a small PTV for the same displacement. A relatively larger effect on the target coverage is seen for the small PTV compared to the large PTV.

The orange circles represent the initial dose to PTV, and the white circles represent the dose distribution after a displacement. Thus, the white areas in a) and b) are the amount of dose spill outside PTV and the dark orange area is the area of the target that is not covered by dose. The overlapping area between the two circles represent the target coverage after the displacement and is relatively larger for the larger PTV a) (fig. 5.1).

The reference plan quality regarding target coverage was worse for the 22 mm PTV (fig. 4.6). This is as expected as it is more difficult to deliver the prescribed dose to a small target due to photon interaction in the body (theory 2.1.1). D_{95} showed larger influence from displacement on the smallest PTVs which may indicate that the treatment plan quality has an effect on the influence on dosimetric impact from geometric distortions. However, the treatment plan quality was not found to influence the impact when analysing the shape case (section 5.3). Hence, the increased influence on smaller targets is more likely to be an effect of larger displacement relative to the target size as discussed above.

The dose spill (fig. 4.7) was larger for smaller targets which also results in worse treatment plan quality. However, the change in dose spill for each displacement is similar for all PTV sizes. This is as expected

since the dose spill is calculated relative to the total 2 Gy isodose curve. Even though the dose spill was smaller and target coverage was better for the larger PTVs, the actual volume of the dose spill is still greater. This was illustrated by the volume of the 2 Gy isodose outside PTV (fig. 4.8) showing a significantly greater volume outside PTV for the larger targets. Thus, the influence on normal tissue is greater and should be further investigated.

The 35 mm PTVs show large variations in dose spill and CI for negative displacements (fig. 4.7, 4.8 and (fig. 4.9). Three plans (plan 1, 4 and 6) have lower dose spill and a higher CI than the the other three plans (table C.6 and D.6, appendix C and D). The compliance between CI and dose spill suggests that their common parameter, the 2 Gy isodose within PTV, is larger for these three plans. Hence, indicating better treatment plans. The DVHs for these plans were investigated, but no significant difference was found. Thus, all the 35 mm plans have a DVH similar to the 35 mm DVH shown (fig. 4.6). These variations between the plans for the same case are difficult to predict since they did not appear on DVH commonly evaluated in the clinic. The three plans (plans 1, 4 and 6) have a higher quality regarding the prescribed 2 Gy isodose. However, the results do not show the 1.9 Gy isodose curve which may be better for the other three plans (plans 2, 3 and 5). Again, the results suggest that D_{95} is the best measure of target coverage.

The CI (fig. 4.9) was larger for displacements in the positive x-direction compared to the negative x-direction for the two smallest PTV. Smaller PTV would be expected to be more prone to the initial 2 Gy isodose position within the target upon displacement as the relative change in position is larger (fig. 5.1). Thus, if the 2 Gy isodose volume is closer to one side of PTV, displacement in this direction would cause an increase in CI. By only considering CI, small displacements in the positive x-direction seem to be a better treatment plan than the reference plan. However, D_{95} decreased and the dose spill increased, supporting that these parameters need to be evaluated together and care should be taken when interpreting the results.

To summarise, 2 mm translational distortions were clinically acceptable for targets between 22 mm and 30 mm. Larger targets may tolerate larger distortions. Hence, the small targets represent the worst-case scenario. The dose delivered to healthy tissue is larger when larger targets are mispositioned simply because the volume of the planned dose is larger. The resulting normal-tissue complications should be considered and investigated further to fully understand the repercussions of geometric distortions. This thesis is limited to the dosimetric effect on the target and only indicates the relative dose spill of the 2 Gy isodose. The 1.9 Gy isodose might produce different results.

5.5 PTV position

The influence of PTV's position within the phantom on the dosimetric impact from translational geometric distortions was tested (section 3.5.3). PTVs were positioned in the centre, and 3 cm, 6 cm and 9 cm from the centre in the positive x-direction. Moving PTV further from the centre was not performed as it would be too close to the edge of the phantom. Photon external beam therapy is not well suited for superficial tumours (theory 2.1.1) without the use of a bolus and was therefore not performed.

This section discusses the results from D_{95} (fig. 4.10) obtained from the DVHs (fig. 4.11), dose spill (fig.

4.12) and CI (fig. 4.13).

D_{95} (fig. 4.10) shows little influence from PTV's position within the phantom. The means are similar for all positions with small variations. Translational geometric distortions above 2 mm were found unacceptable for all positions. The standard error increases as the displacement increases, possibly because differences between the plans become more evident when moving the isocentre further away. Small differences in the plans cause displacements in one direction to be more favourable than others, thus resulting in a larger variation. However, the variations are not large (<1%, fig. 4.10). Similar increased variations with displacements were found when analysing the body shape's influence (section 5.3) and also apply for the size case (fig. 4.5).

The simulated spine is found in the centre of the image (fig. 3.2.2). Bone has a slightly higher electron density than soft tissue (theory 2.1.1). Therefore, as observed for the lung insert, one might expect a different tolerance of translational geometric distortion when moving the beams isocentre towards the bone than away from the bone. A decreased dose when moving the beams isocentre in the negative x-direction is expected for lower energetic MV photons. This is the opposite effect compared to the lung previously discussed (section 5.3). The largest difference in mean D_{95} comparing displacements in the negative and positive direction was found for the 6 cm case for 3 mm displacement where the difference was approximately 1.6%. Thus, the effect from bone is less evident than the effect from the lung. Since the Compton effect dominates (theory 2.1.1), the bone only causes a minimal reduction of dose behind it [8]. However, it did not affect the influence of translational geometric distortions as the clinically acceptable limit was 2 mm in both directions. The results might be different for larger areas of bone and could be further investigated. For higher energetic MV photons, pair production will also occur. In such cases, pair-production could result in an increased dose behind the bone compared to lower energetic photons [8]. This case could also be further investigated. Note however, that lower energetic MV photons are mainly used (theory 2.1.1).

The DVHs (fig. 4.11) show little difference in the reference plan quality. All the reference plans were therefore similar in plan quality.

Although D_{95} appears almost unaffected by PTV's position within the phantom, larger variations were found analysing CIs (fig. 4.13). The volumes positioned 6 cm and 9 cm towards the edge of the phantom showed an increased CI for displacements in the positive x-direction and decreased CI for displacements in the negative x-direction. The same was found for the other two PTV positions, only less evident. Furthermore, the dose spill was larger for displacement in the negative x-direction. These results indicate that the 2 Gy isodoses within the PTVs are positioned closer to the edge of the phantom. The results also agree with the expected effect from bone; A decreased dose for displacements towards the bone. However, this effect was barely notable on the D_{95} (fig. 4.10) and the lung tissue only affected low doses (section 5.3). Therefore it is more likely that the observed lower CI and higher dose spill for negative displacements are due to the accumulation of higher isodoses closer to the edge within PTV. A possible explanation may be the build-up effect (theory 2.1.1 fig. 2.1) causing larger depositions of higher doses closer to the surface.

To summarise, D_{95} results show minimal influence of PTV's position within the body on the effect of translational geometric distortions. However, suggesting that care should be taken when PTVs are in

proximity to inhomogeneities such as lung or bone. This may also extend to air cavities due to the lack of electrons to interact with. Translational distortions up to 2 mm were found clinically acceptable for all PTV positions. Higher doses within PTV were found to accumulate closer to the edge of the phantom within PTV. Therefore, significant differences in the prescribed dose are observed for displacements in different directions. Although the position of PTV does not influence the dosimetric effect from translational geometric distortions, it may influence the magnitude of the distortions. Fewer distortions are expected closer to the centre of the FOV because the magnetic field is more homogeneous closer to the magnetic isocentre (theory 2.3.2). Thus, if the tumour is far from the body centre, a combined CT and MRI workflow may be beneficial. For the sCT generation in an MRI-only workflow, a MRI of the entire body area is necessary. However, when co-registering these imaging modalities, smaller FOVs may be applied in the MRI images to only include the tumour.

5.6 Photon energy

The photon energies 6 MV, 10 MV and 15 MV were tested (section 3.5.4). These are the energies possible to use in Varian Eclipse at UNN.

This section will discuss the results from D_{95} (fig. 4.14), DVH (fig. 4.15), dose spill (fig. 4.16) and CI (fig. 4.17).

The lower energetic photons show a slightly lower D_{95} with displacement than higher energetic photons (fig. 4.14). This is especially evident for displacements in the positive x-direction. Lower energetic photons are more easily attenuated than higher energetic photons. Therefore, lower energetic photons could be more prone to translational geometric distortions. However, the differences are small and mostly within each other's error bars. The DVHs (fig. 4.15) show similar reference plan quality. Thus, the target coverage is similar for all reference plans.

The dose spill supports little influence of photons energy on the effect of translational geometric distortions. This is because the dose spill is within each other's error bars and symmetric around the reference plans (fig 4.16). The CI is not symmetric (fig. 4.17), suggesting that the position of the 2 Gy isodose favours displacements in the positive x-direction. The variations in CI within the same energy case also increases with displacements. This is similar to results previously observed (section 5.3 and 5.5). Again, the explanation is that small differences in the 2 Gy isodose position within PTV becomes more evident for larger displacements resulting in larger variations between the plans.

The influence of energy may be more significant in proximity to inhomogeneities. As discussed (section 5.3), the lung may cause a build-up behind it. This effect could be even more pronounced for higher energetic photons as the build-up effect will be more significant (theory 2.1.1).

To summarise, photon energy has little influence on the effect of translational geometric distortions. Which photon energy to utilise clinically is specified in the literature [15]. The clinically acceptable limit of translational geometric distortions was 2 mm for all energies. The choice of energy in the presence of distortions does not compromise treatment additionally.

5.7 PTV tissue density

PTVs were positioned in soft tissue, lung tissue and bone to evaluate how the tumour composition influences the effect of translational geometric distortions. Lung tissue are least dense and has fewer electrons for the photons to interact with. Soft tissue is denser than lung tissue but less dense than bone. Tumour tissue often resembles soft tissue, and MRI may be beneficial due to the better soft-tissue contrast. However, lung and bone cancer also occur, making these choices clinically relevant. Furthermore, the results may be valid for other cancer tissues as bone and lung demonstrate the extremes considering the difference in electron densities. Lung tissue was evaluated on the NEMA IQ phantom, while bone and soft tissue were evaluated on the pelvis phantom. Thus, the body shape may influence the results. However, little influence from the body shape was found (section 5.3). The findings are therefore likely to be a result of the different tissue densities.

This section will discuss the results from D_{95} (fig. 4.18), DVHs (fig. 4.19), dose spill (fig. 4.20) and CI (fig 4.21).

A clinically acceptable limit of 2 mm translation distortions was found for soft tissue and lung tissue (fig. 4.18). D_{95} for the bone cases were more affected and the tolerance limit is a bit less than 2 mm. This is as expected because of higher attenuation in bone. Furthermore agreeing with the energy results, where lower energetic photons were found more affected due to higher attenuation (section 5.6). However, relative D_{95} values are similar and within the other tissues' standard error for most displacements.

The results indicate little influence of PTV's composition on the effect of translational geometric distortions. DVHs for the lung tissue indicate a worse reference treatment plan as the dose in large parts of the volume is less than for the soft tissue and bone cases. An explanation is the low electron density in lung tissue making the dose deposition more difficult. These plans also had higher MU values (table E.1 appendix E), meaning more radiation energy per angle to ensure the desired dose accumulation in PTV. Note that the interpretation of these results assumes a correct dose calculation by the TPS. Lung tissue is prone to lateral electron scattering, making the dose calculation more advanced and possibly not as accurate. However, since the dose calculation algorithm is used clinically, the results project clinically relevant results. One could expect the worse treatment plan quality for the lung tissue to be evident on the dose spill (fig. 4.20). On the contrary, the dose spill was lower for lung tissue than for the other tissue types. However, the plan quality did not influence the impact of translational geometric distortions, regarding D_{95} (fig. 4.18). Again, the results support little influence of treatment plan quality on the effect of geometric distortions as previously discussed (section 5.3).

The CI for the lung tissue was symmetric around the reference plans (fig. 4.21), suggesting that the 2 Gy isodose within the target is close to the centre. For bone and soft tissue, CIs favour displacements in the positive x-direction indicating an accumulation of higher doses closer to this direction within PTV. Because the dose spill is symmetric around the reference dose, both the 2 Gy isodose volume inside PTV and the total 2 Gy isodose are similarly affected by the displacements (fig 4.20).

To summarise, the tissue composition of PTV does not influence the effect of translational geometric distor-

tions. However, large areas of bone may need extra consideration due to the higher photon attenuation, which may cause a slightly larger effect from displacements. An MRI-only workflow is applicable independent of the tumour compositions as long as the distortions are kept below 2 mm.

5.8 Patient case

Patient images were utilised to verify the phantom results. As mentioned (section 1), phantom results are reproducible and were therefore mostly utilised in this thesis. Furthermore, it was easier to isolate the effect from one parameter. PTV's size was found to have an impact on the effect of translational geometric distortions (section 5.4). The same sizes were chosen for the patient case to ensure a correct comparison between the phantom and patient results.

This section will discuss the patient results from D_{95} analysis (fig. 4.22), DVHs (fig. 4.23), dose spill (fig. 4.24 and 4.25) and CI (fig. 4.26). Furthermore, the dose error using phantom data on patients will be discussed (fig. 4.27).

Smaller targets were more influenced by displacements than larger targets (fig. 4.22) regarding target coverage D_{95}. This was as expected, as discussed earlier (section 5.4). D_{95} decreases as the displacement increases, also as expected. Thus, the patient investigation provides similar results as the phantom investigations. The clinically acceptable displacement was around 2 mm for the 26 mm and 30 mm PTVs, 1.5 mm for 22 mm PTVs and 2.5 mm for 35 mm PTVs. The tolerance for translational geometric distortions was therefore found lower for the patient case than the phantom case for the 22 mm target. Consequently, using phantom data may lead to underestimating the effect of translational geometric distortions. The maximum relative dose difference comparing the 22 mm PTV in the phantom to the patient, was 1.8 % (fig. 4.27). As discussed (section 5.4), smaller targets are more prone to distortions because the relative displacement is larger. Furthermore, the more complicated composition of the patient body causes this effect to increase with displacements (fig. 4.27). Although 1.8% was larger compared to the maximum difference of 0.5 % found for the 26, 30 and 35 mm PTV, the difference is below the gamma criteria of 3 % utilised in the clinic. The gamma criteria are used to compare a planned dose to the actual delivered dose. Hence, if assuming the planned dose can be delivered, 1.8 % dose difference is within the clinically acceptable limit. However, if the dose difference is 1.8 %, fewer distortions would be tolerable considering both these errors. For small targets (< 26 mm), phantom data may be applied to patient cases, but extra consideration is needed if the amount of distortions are large. In clinical cases where PTV is larger than 26 mm, phantom data may be safely applied because the dose difference was below 0.5 % for all displacements (fig. 4.27). Furthermore, the difference did not increase with displacement.

The dose spill dependence on PTV size is difficult to interpret as the smallest target has the lowest dose spill and the second smallest target has the most dose spill (fig. 4.24). However, the dose spill increases as the displacements increase, and the volume of the dose spill is larger for larger PTVs (fig. 4.25), as expected from the phantom cases. Furthermore, despite a significant difference in dose spill for several displacements, the means are mostly within each other's standard errors.

The CI has been shown to be vulnerable to the 2 Gy isodose's position within the reference plan before

introducing the displacements. Analysing the patient plans shows that the 2 Gy isodose is positioned closer to the negative x-direction within PTV. This is because the CI is higher for displacements in that direction. The exact position is not portrayed in any of the parameters investigated. The dose distribution depends on the optimisation algorithm fulfilling the dose criteria set, and there are no constraints on where the dose should accumulate within the target. As mentioned, CI should therefore not alone be an indicator of the treatment plan quality.

The DVHs (fig. 4.23) show increasing plan quality as the target size increases. This is because it is more difficult to deliver the desired dose to a small volume. As discussed for the phantom case (section 5.4), it may look like the plan quality and the target coverage as a function of displacement are in agreement, and one may be tempted to conclude that the plan quality influences the effect of translational geometric distortions. However, the larger tolerance for the larger PTV is not because of a better reference plan quality but because the displacement size is relatively smaller compared to the target size than for a smaller target.

To summarise, the patient results are in agreement with the phantom results. The maximum dose difference was found to be 1.8 % and the tolerance limit of translational geometric distortions was 2 mm. The phantom results are therefore applicable for patient cases and the influence of the parameters investigated in this thesis holds.

5.9 Patient selection for MRI-only

Generally, this study found 2 mm translational geometric distortions to be clinically acceptable (< 5% dose difference D_{95}). This is in agreement with ACR [29] that define a 2 mm misposition limit of any lengths in the image for their specific phantom. PTV's size was found to affect the tolerance limit. Larger targets tolerated more displacements regarding target coverage. Thus, these results suggest that larger tumours are less sensitive to geometric distortions than smaller tumours. However, the normal tissue may not tolerate these displacements, especially if critical structures are close to the target. This is because the volume of the dose spill is larger for larger targets. Some organs are more sensitive to a small volume of larger doses than large volumes of small doses and vice versa. The effect on OARs should therefore be further investigated for different cancer sites.

The tumour composition and position within the body were found to have minimal impact on the effect of translational geometric distortions. An MRI-only workflow may therefore be beneficial independent of these parameters. Thus, the workflow is generally applicable for all cancer sites within the body. However, even though the tumour position did not influence the effect of geometric distortions, it influenced the magnitude of the distortions (section 5.5). Therefore the amount of geometric distortions should be verified below 2 mm, and extra considerations may be needed if the tumour is positioned far from the magnetic isocentre.

The body shape was also found to have minimal impact on the effect of geometric distortions. However, large bodies, i.e., very obese patients, may not be suited for MRI-only if the tumour position is far from the magnetic isocentre or if the patient does not fit into the MRI-machine. This was the case for 2 patients in a study of MRI-only for prostate cancer [44]. Furthermore, patients with metal implants are not suited for

MRI-only due to large distortions.

For patients struggling with motion restrictions or patients needing treatment delivery during breath-hold, the expected distortions may be larger than 2 mm. The RT fraction delivery is typically shorter than an MRI examination, and matching the breathing level may not be possible [45]. In some cases, a CT may be the best solution because of the shorter image acquisition. However, the need for improved soft-tissue contrast for volume delineation must be compared to the decreased target coverage because of motion. Suppose the patient is dependent on the improved delineation of tumour volume and OARs. In that case, an MRI-only workflow may be superior to the combined workflow to reduce the large co-registration errors caused by motion. Furthermore, an MRI-guided therapy would be even more applicable to monitor the motion during RT treatment [45]. Cancer sites at areas prone to motion and where geometric accuracy is important due to the position of OARs may therefore benefit from a workflow with fewer imaging modalities. An example may be head and neck cancer where radiosensitive organs, e.g., the spinal cord, is in close proximity. Adjeiwaah, Mary, et al. (2019) showed little dosimetric difference for head and neck cancer patients [3] between distorted and undistorted plans.

An example of a cancer site suited for an MRI-only workflow is brain cancer. Patients with brain cancer may benefit from avoiding the extra dose from the CT scan and improved delineation from the enhanced soft-tissue contrast. Co-registering MRI and CT is currently the standard planning process for brain cancer to ensure correct tumour localisation and extent [42]. The co-registration uncertainties are approximately 2 mm [38]. The brain is an area with little motion and small FOV compared to other body parts. The expected distortions are therefore small (theory 2.3.2), making it suitable for an MRI-only workflow. The results from the size cases show that extra considerations are needed if the tumour is smaller than 26 mm. This is in agreement with Pappas et al. (2017) [4] that found a significant dose difference for 1 mm distortions for targets below 20 mm.

To summarise, the patients benefitting from the co-registration workflow should be suited for an MRI-only workflow. An MRI-only workflow will improve treatment by enhancing delineation, removing co-registration errors and simplifying the workflow for both patients and clinicians. The amount of geometric distortions should be predicted and found below 2 mm.

5.10 Further work

Plans generated for one PTV and no additional volumes were utilised in this thesis. This is considered a simple plan where the dose is homogeneously distributed within the volume. A more advanced plan with several volumes and criteria may produce a plan with more considerable dose variations within the volume. Thus, these plans may be more prone to distortions in some directions than others. The CI investigated in this thesis may be an indicator of how important the position of these doses may be where one direction tolerated more distortions than the other direction. However, this study was in agreement with studies investigating the dosimetric effect on cancer patients. As mentioned above, a prostate study showed no significant dose impact from geometric distortions [2]. Hence, the 2 mm limit may be valid even for more complicated

plans. However, this should be further investigated. This thesis only considered translational distortions in two directions in relation to VMAT. Other types of geometric distortions may result in slightly different dosimetric effects. Furthermore, the dosimetric impact on critical structures where not investigated. To fully understand the repercussions of geometric distortions, the effects on healthy tissue should be considered.

Therefore, further investigation should involve 1) translational distortions in other directions, 2) other types of geometric distortions than translational, 3) More advanced treatment plans and 4) the dosimetric influence on healthy tissue. Furthermore, methods to generate sCT of other areas than the brain and pelvis and methods to reduce geometric distortions further should be developed.

6 Conclusion

This study found the general clinically acceptable limit of translational geometric distortions to be 2 mm using acceptance criteria of 5% dose difference in D_{95}. This limit was found independent of PTV's position within the body, body shape, tissue density in PTV and photon energy. Thus, the results are applicable regardless of cancer site and tissue type. Small targets below 26 mm in diameter tolerate less and larger targets above 35 mm tolerate more. The dosimetric effect may vary in proximity to tissue inhomogeneities, e.g., lung and bone, and require extra consideration.

This thesis mainly utilised phantom images for investigations. However, the results were compared to translational geometric distortions introduced on patient images. The results were in good compliance for target volumes above 26 mm. For the 22 mm diameter PTV, using phantom data to predict the effect on patients may result in larger errors as the maximum dose difference was found to be 1.8%. However, this is clinically acceptable by considering the gamma dose criteria of 3 % utilised in the clinic. To conclude, the phantom results can be safely utilised for patients. Although, extra consideration could be needed for small targets combined with large displacements.

This thesis suggests that an MRI-only workflow is adequate when the translational geometric distortions are below 2 mm. Concerning geometric distortions, all patients suited for a combined CT and MRI workflow could potentially benefit from an MRI-only workflow if the distortions are below this limit.

Although the aim was to quantify the effect of translational geometric distortions, the results may also be valid for other uncertainties leading to translational relocation of the target. The results are limited to simple VMAT plans generated using sCT only and only consider the effect on target coverage. Further investigations should be performed to determine the effect on normal tissue and investigate other geometric distortions.

References

[1] Philip Mayles, E. Alan Nahum and Jean-Claude Rosenwald. *Handbook of radiotherapy physics: theory and practice*. Taylor & Francis, 2007.

[2] Mary Adjeiwaah et al. 'Quantifying the effect of 3T magnetic resonance imaging residual system distortions and patient-induced susceptibility distortions on radiation therapy treatment planning for prostate cancer'. In: *International Journal of Radiation Oncology* Biology* Physics* 100.2 (2018), pp. 317–324.

[3] Mary Adjeiwaah et al. 'Dosimetric impact of MRI distortions: a study on head and neck cancers'. In: *International Journal of Radiation Oncology* Biology* Physics* 103.4 (2019), pp. 994–1003.

[4] Eleftherios P Pappas et al. 'MRI-related geometric distortions in stereotactic radiotherapy treatment planning: evaluation and dosimetric impact'. In: *Technology in cancer research & treatment* 16.6 (2017), pp. 1120–1129.

[5] T Seibert et al. 'Distortion inherent to magnetic resonance imaging (MRI) can lead to geometric miss in radiosurgery planning'. In: *International Journal of Radiation Oncology, Biology, Physics* 90.1 (2014), S97.

[6] Amy Walker et al. 'MRI geometric distortion: Impact on tangential whole-breast IMRT'. In: *Journal of applied clinical medical physics* 17.5 (2016), pp. 7–19.

[7] Lene Fikstvedt. 'Dosimetric impact of geometric distortions in radiotheraputic dose planning'. In: *Not published* (2021). Project thesis conducted at NTNU and UNN during autumn 2021.

[8] Eric J Hall, Amato J Giaccia et al. *Radiobiology for the Radiologist*. Vol. 6. Philadelphia, 2006.

[9] JHL Mott and NS West. 'Essentials of Depth Dose Calculations for Clinical Oncologists'. In: *Clinical Oncology* 33.1 (2021), pp. 5–11.

[10] Helsedirektoratet. *Nasjonalt handlingsprogram med retningslinjer for gynekologisk kreft*. `https://www.helsedirektoratet.no/retningslinjer/gynekologisk-kreft-handlingsprogram`. [Online; accessed May, 2022]. 2021.

[11] Norwegian Radiation Protection Authority. *Volumes and doses for external radiotherapy - Definitions and recommendations.* `https://dsa.no/publikasjoner/stralevernrapport-9-2012-volum-og-doser-i-ekstern-straleterapi/StralevernRapport_09-2012.pdf`. [Online; accessed May, 2022]. 2012.

[12] Daniela Thorwarth, Sara Leibfarth and David Mönnich. 'Potential role of PET/MRI in radiotherapy treatment planning'. In: *Clinical and Translational Imaging* 1.1 (2013), pp. 45–51.

[13] Nadja Ebert, Falk Tillner and Michael Baumann. 'Radiation Oncology'. In: *Encyclopedia of Cancer (Third Edition)*. Ed. by Paolo Boffetta and Pierre Hainaut. Third Edition. Oxford: Academic Press, 2019, pp. 321–336. ISBN: 978-0-12-812485-7.

[14] Eclipse. *Eclipse Photon and Electron Algorithms Reference Guide*. https://jpneylon.github.io/ABR/PDFs/Add_052418/EclipseAlgorithms13.6_RefGuide.pdf. [Online; accessed March, 2022]. 2015.

[15] Helsedirektoratet. *Kreft*. https://www.helsedirektoratet.no/tema/kreft. [Online; accessed May, 2022].

[16] Karl Otto. 'Volumetric modulated arc therapy: IMRT in a single gantry arc'. In: *Medical physics* 35.1 (2008), pp. 310–317.

[17] Janne Sievinen, Waldemar Ulmer, Wolfgang Kaissl et al. 'AAA photon dose calculation model in Eclipse'. In: *Palo Alto (CA): Varian Medical Systems* 118 (2005), p. 2894.

[18] ICRU. 'Report 83'. In: *Journal of the International Commission on Radiation Units and Measurements* 10.1 (June 2016), NP–NP. ISSN: 1473-6691.

[19] Dimitri Lefkopoulos et al. 'Determination of dose-volumes parameters to characterise the conformity of stereotactic treatment plans'. In: *The Use of Computers in Radiation Therapy*. Springer, 2000, pp. 356–358.

[20] Edward Shaw et al. 'Radiation Therapy Oncology Group: radiosurgery quality assurance guidelines'. In: *International Journal of Radiation Oncology* Biology* Physics* 27.5 (1993), pp. 1231–1239.

[21] Nicoletta J Lomax and Stefan G Scheib. 'Quantifying the degree of conformity in radiosurgery treatment planning'. In: *International Journal of Radiation Oncology* Biology* Physics* 55.5 (2003), pp. 1409–1419.

[22] Arie Van't Riet et al. 'A conformation number to quantify the degree of conformality in brachytherapy and external beam irradiation: application to the prostate'. In: *International Journal of Radiation Oncology* Biology* Physics* 37.3 (1997), pp. 731–736.

[23] Nadine Barrie Smith. *Introduction to medical imaging : physics, engineering and clinical applications*. eng. Cambridge, 2011.

[24] Joseph Weygand et al. 'Spatial precision in magnetic resonance imaging–guided radiation therapy: the role of geometric distortion'. In: *International Journal of Radiation Oncology* Biology* Physics* 95.4 (2016), pp. 1304–1316.

[25] Cathrine Westbrook and John Talbot. *MRI in practice, 5th edition*. Wiley Blackwell, 2019.

[26] Donald W McRobbie et al. *MRI from Picture to Proton*. Cambridge university press, 2017.

[27] Gary P Liney and Marinus A Moerland. 'Magnetic resonance imaging acquisition techniques for radiotherapy planning'. In: *Seminars in radiation oncology*. Vol. 24. 3. Elsevier. 2014, pp. 160–168.

[28] IAEA International Atomic Energy Agency. *Accuracy Requirements and Uncertainties in Radiotherapy*. IAEA Human Health Series. IAEA, 2017.

[29] EF Jackson et al. 'Acceptance testing and quality assurance procedures for magnetic resonance imaging facilities'. In: *American Association of Physicists in Medicine One Physics Ellipse College Park* (2010).

[30] A.D Elster. *Magnetic susceptibility*. http://mriquestions.com/what-is-susceptibility.html. [Online; accessed January, 2022]. 2021.

[31] Jinsoo Uh et al. 'MRI-based treatment planning with pseudo CT generated through atlas registration'. In: *Medical physics* 41.5 (2014), p. 051711.

[32] Siemens Healthcare GmbH. *MR-only RT planning for the brain and pelvis with Synthetic CT*. https://www.siemens-healthineers.com/magnetic-resonance-imaging/clinical-specialities/synthetic-ct. [Online; accessed February, 2022]. 2019.

[33] Siemens Healthcare GmbH. *MR-based Synthetic CT reimagined*. white paper. received by mail from Siemens Healthineers on request April 2022. 2022.

[34] Bernard Rosner. *Fundamentals of biostatistics*. Cengage learning, 2015.

[35] Helsedirektoratet. *Nasjonalt handlingsprogram med retningslinjer for diagnostikk, behandling og oppfølging av lungekreft, mesoteliom og thymom*. https://www.helsedirektoratet.no/retningslinjer/lungekreft-mesoteliom-og-thymom-handlingsprogram. [Online; accessed May, 2022]. 2021.

[36] Yue Yan et al. 'Impact of geometric distortion on dose deviation for photon and proton treatment plans'. In: *Journal of Applied Clinical Medical Physics* 23.3 (2022), e13517.

[37] Roel JHM Steenbakkers et al. 'Reduction of dose delivered to the rectum and bulb of the penis using MRI delineation for radiotherapy of the prostate'. In: *International Journal of Radiation Oncology* Biology* Physics* 57.5 (2003), pp. 1269–1279.

[38] Amir M Owrangi, Peter B Greer and Carri K Glide-Hurst. 'MRI-only treatment planning: benefits and challenges'. In: *Physics in Medicine & Biology* 63.5 (2018), 05TR01.

[39] Signe Winther Hasler et al. 'Tumor-site specific geometric distortions in high field integrated magnetic resonance linear accelerator radiotherapy'. In: *Physics and Imaging in Radiation Oncology* 15 (2020), pp. 100–104.

[40] Emilia Persson. 'Validation and clinical implementation of an MRI-only prostate cancer radiotherapy workflow'. PhD thesis. Lund University, 2020.

[41] Hanna Solum and Marte Lindgaard. 'Geometriske forvrengingers påvirkning av sekvenser i MRI-only stråleterapibehandling'. Bachelor's Thesis. Norges arktiske universitet, UiT, 2022.

[42] Helsedirektoratet. *Nasjonalt handlingsprogram med retningslinjer for diagnostikk, behandling og oppfølging av hjernesvulster generelt (hos voksne)*. https://www.helsedirektoratet.no/retningslinjer/hjernesvulster-handlingsprogram. [Online; accessed May, 2022]. 2020.

[43] Asha Kandathil et al. 'Role of FDG PET/CT in the eighth edition of TNM staging of non–small cell lung cancer'. In: *Radiographics* 38.7 (2018), pp. 2134–2149.

[44] Mikko Tenhunen et al. 'MRI-only based radiation therapy of prostate cancer: workflow and early clinical experience'. In: *Acta Oncologica* 57.7 (2018), pp. 902–907.

[45] Maria A Schmidt and Geoffrey S Payne. ‘Radiotherapy planning using MRI’. In: *Physics in Medicine & Biology* 60.22 (2015), R323.

Appendix

A Guide to the appendix

The appendix contains the data used to generate the plots presented (section 4). Appendix B contains tables with the calculated D_{95} values for all six measurements for each case and for every displacement. Appendix C and D contains the same tables but with the calculated dose spill and CI for each displacement, respectively. Appendix E shows a table of the MU values characterising each plan. Finally, Appendix F contains the code created and utilised during the work of this thesis. It comprises of the code to create the synthetic spherical phantom created for the project paper followed by the code to evaluate and generate the DVH plots, calculate D_{95}, dose spill and CI. It also contains the code to display the CT images.

B Calculated D95

This appendix presents D_{95} values for each displacement for the different cases investigated in this thesis. The code used to generate the data are found in appendix F.

The D_{95} values for the spherical phantom (fig. 3.1) are found in table B.1. The six VMAT plans are generated using 6 MV photons, a 22 mm diameter PTV in the centre, and are optimised as explained in section 3.3.

Table B.1: D_{95} values for plans generated using a spherical water phantom with a 22 mm diameter PTV.

Displacement	**Sphere phantom**					
[mm]	1	2	3	4	5	6
-3	90,80109771	90,13101589	89,30584138	90,65081407	90,16608538	89,31685749
-2,5	93,16617322	93,1127666	92,33451133	93,47248592	93,08936281	92,42528656
-2	95,24300697	95,49382128	94,84981899	95,6968858	95,39534793	94,99658832
-1,5	97,44017882	97,6427805	97,13898854	97,9453293	97,51610531	97,33287695
-1	98,62069191	98,83632447	98,6713367	99,09779196	98,65466836	98,73370444
-0,5	99,68006841	99,78091702	99,7573858	99,84814325	99,62301037	99,79181711
0	100	100	100	100	100	100
0,5	99,68006841	99,78091702	99,7573858	99,84814325	99,62301037	99,79181711
1	98,62069191	98,83632447	98,6713367	99,09779196	98,65466836	98,73370444
1,5	97,44017882	97,6427805	97,13898854	97,9453293	97,51610531	97,33287695
2	95,24300697	95,49382128	94,84981899	95,6968858	95,39534793	94,99658832
2,5	93,16617322	93,1127666	92,33451133	93,47248592	93,08936281	92,42528656
3	90,80109771	90,13101589	89,30584138	90,65081407	90,16608538	89,31685749

D_{95} values for the pelvis phantom (fig. 3.2) are seen in table B.2. The six VMAT plans are generated using 6 MV photons, a 22 mm diameter PTV in the centre, and are optimised as explained in section 3.3.

Table B.2: D_{95} values for plans generated using a pelvis phantom with a 22 mm diameter PTV.

Displacement	**Pelvis phantom**					
[mm]	1	2	3	4	5	6
-3	90,6282882	89,77021593	90,06593314	90,40705658	89,13287178	90,59594699
-2,5	93,31083449	92,63846818	92,99633402	93,22414934	92,61205601	93,34115446
-2	95,40161869	95,06846475	95,34571598	95,47780882	95,16823927	95,57352098
-1,5	97,3283824	96,98731948	97,41324001	97,40278527	97,28783243	97,50582904
-1	98,79679233	98,5513051	98,92253169	98,9260307	98,80208621	98,95897478
-0,5	99,69058709	99,51063532	99,72715402	99,77375636	99,61399907	99,72305894
0	100	100	100	100	100	100
0,5	99,75322769	99,8203029	99,6579465	99,65607075	99,76693611	99,92618587
1	98,97999386	99,12005551	98,82135601	98,83716627	99,00214181	99,39695771
1,5	97,35162523	97,87861748	97,46189155	97,40750068	97,78984081	98,07595462
2	95,38225148	96,16947651	95,73858701	95,6905056	96,20726341	96,22829753
2,5	93,13558382	93,98997536	93,50987456	93,46462971	94,12686871	94,11804624
3	90,59273128	91,44152691	90,9732821	90,99897193	91,63941758	91,6483121

D_{95} values for the NEMA IQ phantom are seen in table B.3. The six different plans are generated using 6 MV photons and a 22 mm PTV positioned as explained in section 3.5.1.

Table B.3: Calculated D_{95} for plans generated using the NEMA IQ phantom with a 22 mm diameter PTV.

Displacement	**Nema IQ phantom**					
[mm]	1	2	3	4	5	6
-3	94,70462519	93,71498117	94,01562027	93,35250983	95,14202498	93,33085752
-2,5	96,75664227	96,19993369	96,3075864	95,81829365	97,40551546	95,84666229
-2	98,23068534	98,20311078	97,92062013	97,77717219	99,01552286	97,74304691
-1,5	99,20147455	99,43355984	98,94878223	99,06046684	99,74420045	98,94545651
-1	99,7433295	99,94097885	99,58384734	99,72586889	100,06981245	99,62958991
-0,5	100,01024238	100,1240499	99,94625726	100,03247997	100,16407431	99,96282633
0	100	100	100	100	100	100
0,5	99,77069833	99,59752388	99,83520128	99,69790427	99,56157032	99,81326462
1	99,22792614	98,79660523	99,40097384	99,00242887	98,68817788	99,36483706
1,5	98,21533867	97,47947539	98,52697931	97,79387662	97,32724308	98,40175511
2	96,82106365	95,60908124	96,84872795	96,07469528	95,37038997	97,09029918
2,5	94,94242984	92,85112736	94,24707984	93,67702003	92,71605043	95,34472801
3	92,47941675	89,44271843	90,73002845	90,78333549	89,51118176	93,07776317

Calculated D_{95} values for treatment plans generated for the pelvis phantom with a 26 mm PTV positioned in the centre is presented in table B.4.

Table B.4: D_{95} values for treatment plans generated using a 26 mm spherical PTV positioned in the centre of the pelvis phantom (fig. 3.2)

Displacement	**PTV 26 mm**					
[mm]	1	2	3	4	5	6
-3	89,61289435	90,09203874	89,40551151	90,74143331	89,86894611	90,40837808
-2,5	92,67695946	92,9484244	92,40245047	93,57301371	92,74000815	92,09794691
-2	95,09010669	95,31371563	94,8648603	96,02746754	95,0014254	95,53011548
-1,5	97,25995816	97,38996816	97,14579652	98,04624732	97,11279995	97,64938604
-1	99,0106736	98,96326177	98,92350446	99,32277389	98,81923472	99,12180185
-0,5	99,82087712	99,80536866	99,72685463	99,84454185	99,73117781	99,80408396
0	100	100	100	100	100	100
0,5	99,86883191	99,68164251	99,90501553	99,90280338	99,8513933	99,81939156
1	99,15139105	98,70258132	99,25979312	99,2967453	99,07858719	99,07000369
1,5	97,63543574	97,03888529	97,6097393	97,98084146	97,32848596	97,50697621
2	95,71401911	95,09142065	95,39578528	96,03406105	95,34161302	95,60620518
2,5	93,49337898	92,78719613	92,98968308	93,96055711	92,94790336	93,33971438
3	90,86537505	90,19894108	90,05523947	91,36088788	90,25021561	90,68940111

Calculated D_{95} values for treatment plans generated for the pelvis phantom with a 30 mm PTV positioned in the centre are presented in table B.5.

Table B.5: Calculated D_{95} values for treatment plans generated using a 30 mm spherical PTV positioned in the centre of the pelvis phantom (fig. 3.2)

Displacement	**PTV 30 mm**					
[mm]	1	2	3	4	5	6
-3	93,54925162	91,749709	93,27707819	92,71283437	92,92911349	92,68918089
-2,5	95,5887453	94,16300547	95,35001702	94,90202957	95,06321388	94,9320507
-2	97,3670869	96,66947384	97,1182777	96,78517971	96,91646647	96,93595722
-1,5	98,81699059	98,59462148	98,56586806	98,29687774	98,45851533	98,51273617
-1	99,56639443	99,53455959	99,45987594	99,34242971	99,49828697	99,47392504
-0,5	99,91262656	99,91129202	99,88554266	99,870895	99,90867854	99,87041409
0	100	100	100	100	100	100
0,5	99,8725457	99,89595889	99,91004094	99,86995369	99,88687977	99,93744171
1	99,37628844	99,43593403	99,44808253	99,38001186	99,37606885	99,64626545
1,5	98,31542443	98,27535106	98,44834325	98,19932558	98,23272192	98,66307684
2	96,76161842	96,60674087	96,95533556	96,5021818	96,67356006	97,0273744
2,5	94,87062352	94,46748386	95,0635797	94,2877593	94,71848487	95,08137501
3	92,72997888	92,23999898	92,88206131	91,899011	92,5588889	92,90645243

Calculated D_{95} values for treatment plans generated for the pelvis phantom with a 35 mm PTV positioned in the centre are presented in table B.6.

Table B.6: D_{95} values for treatment plans generated using a 35 mm spherical PTV positioned in the centre of the pelvis phantom (fig. 3.2)

Displacement	**PTV 35 mm**					
[mm]	1	2	3	4	5	6
-3	94,78462506	93,92727439	93,87269701	95,05844738	93,59842163	94,62719485
-2,5	96,88770493	96,00880914	95,86457053	96,95430931	95,63409721	96,52216878
-2	98,70294933	97,80070311	97,54272067	98,45998212	97,47998019	98,22029499
-1,5	99,68608582	99,14347273	98,89698327	99,26190731	98,91275618	99,37781849
-1	100,01456648	99,70888453	99,59859344	99,70028158	99,58024861	99,87028134
-0,5	100,0978317	99,93129197	99,9101403	99,96948532	99,90655659	100,02578807
0	100	100	100	100	100	100
0,5	99,64246107	99,86531206	99,85854847	99,79423402	99,88629676	99,74098033
1	99,00788054	99,49631117	99,51853859	99,46859095	99,5048065	99,1983742
1,5	97,86476326	98,61867475	98,62062825	98,88949839	98,77564674	98,26089812
2	96,41259362	97,26050196	97,19684868	97,75233147	97,4414021	96,87277811
2,5	94,67628078	95,53561911	95,46685122	96,02310471	95,80701967	95,16408037
3	92,8333933	93,57469931	93,45321964	94,08715738	93,88212043	93,18962686

The calculated D_{95} values for the case with a 22 mm PTV positioned 3 cm from the centre in the positive x-direction of the pelvis phantom are presented in table B.7.

Table B.7: D_{95} data calculated for treatment plans generated using a 22 mm PTV positioned 3 cm from the centre in the pelvis phantom.

Displacement	**PTV 3 cm**					
[mm]	1	2	3	4	5	6
-3	90,6900431	90,32723883	90,69936448	89,13071938	90,54350447	89,97117334
-2,5	93,22198317	93,23156186	93,31668766	91,96603198	93,22348157	92,77304631
-2	95,37094962	95,61188501	95,62118071	94,82080632	95,57286255	95,122894
-1,5	97,24937699	97,48351134	97,52099003	96,92986259	97,33411893	97,18815602
-1	98,77529838	99,02510467	98,95196744	98,54844112	98,87623779	98,69403775
-0,5	99,61337246	99,78312251	99,69650349	99,59824142	99,67993012	99,64282993
0	100	100	100	100	100	100
0,5	100,00084179	99,69583712	99,84789199	99,9093328	99,84703277	99,84780684
1	99,63099228	98,9234162	99,3149654	99,35941617	99,34745229	99,08128572
1,5	98,43198181	97,71388496	98,05873515	97,95444943	98,18862977	97,69984356
2	96,66655454	95,87661029	96,08834013	96,40685159	96,43327988	95,9561156
2,5	94,35119295	93,5186403	93,7558209	94,32040496	94,29323478	93,77993141
3	91,63415645	90,93107554	90,8767274	92,07256246	91,79354782	91,3453422

Table B.8 shows the calculated D_{95} for treatment plans generated with a 22 mm spherical PTV positioned 6 cm from the centre of the pelvis phantom.

Table B.8: D_{95} for treatment plans generated with a spherical PTV positioned 6 cm from the centre of the phantom.

Displacement	**PTV 6 cm**					
[mm]	1	2	3	4	5	6
-3	90,61252244	90,30490648	90,02986071	91,49205424	91,25043143	90,63475724
-2,5	93,26783301	92,95547701	93,03973443	94,06197011	93,88979832	93,24890703
-2	95,4479869	95,27937826	95,25510538	96,17944563	95,97139362	95,45248505
-1,5	97,40430319	97,21652148	97,35269726	98,01594961	97,87396097	97,35155982
-1	98,78637014	98,7073629	98,88446464	99,22878086	99,13382484	98,81990295
-0,5	99,63866745	99,55634588	99,70967828	99,86086875	99,74263265	99,66429788
0	100	100	100	100	100	100
0,5	99,87438764	99,87346632	99,83222763	99,81239431	99,78852406	99,91093368
1	99,2459317	99,28778465	99,16169109	99,15079364	99,16529163	99,42489093
1,5	98,11132285	98,20204697	97,95891942	97,94783714	97,97788728	98,27645786
2	96,63195092	96,76607103	96,17625301	96,19256592	96,2374043	96,81567673
2,5	94,74308605	94,58042417	93,87789849	93,89920757	94,27285893	94,78443191
3	92,25525895	92,03780591	91,17339938	91,21283711	91,7964209	92,44396194

D_{95} values for each displacement for plans generated with PTV positioned 9 cm from the centre of the phantom are shown in table B.9.

Table B.9: D_{95} data calculated for treatment plans generated using a 22 mm PTV positioned 9 cm from the centre in the pelvis phantom.

Displacement	**PTV 9 cm**					
[mm]	1	2	3	4	5	6
-3	91,21812361	91,8189521	90,84989067	91,36925673	91,03699465	90,70967092
-2,5	93,84469789	94,25089218	93,39823421	93,88824472	93,76373682	93,47522217
-2	96,2713113	96,42166769	96,03715614	96,06867886	95,95504368	95,92191032
-1,5	98,03677122	98,14333979	97,75182395	97,90220764	97,70948209	97,74174926
-1	99,24093712	99,22688445	99,17261044	99,23129005	99,00978512	99,17230482
-0,5	99,79227946	99,7665462	99,8036782	99,73812766	99,68933695	99,79142505
0	100	100	100	100	100	100
0,5	99,96332853	99,90190667	99,7885906	99,84492894	99,73949555	99,94904904
1	99,55930325	99,40171528	99,08876245	99,17489335	99,03909948	99,42018256
1,5	98,17601095	98,26567626	97,88314261	97,71664456	97,65478817	98,23991055
2	96,19347372	96,60348697	96,06467786	95,81020127	95,94926929	96,55807458
2,5	93,73189974	94,32971416	93,89199764	93,64598858	93,75084203	94,34540079
3	90,83846705	91,6690693	91,16504513	90,77837307	90,92976706	91,64227113

Table B.10 presents the calculated D_{95} values for each displacement for plans generated using photons with 10 MV energy.

Table B.10: D_{95} for each displacement for plans generated using 10 MV photons.

Displacement	**Energy 10 MV**					
[mm]	1	2	3	4	5	6
-3	90,3542912	90,1022244	90,6283687	90,7558819	90,602226	91,3796344
-2,5	93,10389	92,5634203	93,0357339	93,4951449	93,4610241	94,1540774
-2	95,4511994	94,9346427	95,4503591	95,7627991	95,7222492	96,4408492
-1,5	97,4533494	96,9669777	97,2755325	97,7659995	97,6280885	98,2597288
-1	98,9059112	98,5510018	98,7485615	99,1355831	99,0321721	99,3847901
-0,5	99,6473737	99,4994433	99,5948481	99,7962402	99,7051929	99,8458779
0	100	100	100	100	100	100
0,5	99,7860597	99,8869942	99,8291897	99,9417308	99,8419679	99,8812553
1	99,1642929	99,2633338	99,1109191	99,668817	99,3343894	99,5447083
1,5	98,0501587	97,9707537	97,9058701	98,6840917	98,305774	98,6911502
2	96,6612803	96,2707736	96,3498408	97,0287666	96,7710843	97,0644881
2,5	94,5950893	94,2849456	94,4208916	95,0528027	94,7692786	95,1702417
3	92,2890397	91,9219603	92,2182961	92,5627724	92,3354266	92,7030048

D_{95} values for each displacement for plans generated using 15 MV photons are found in table B.11.

Table B.11: D_{95} values for each displacement are presented. The six reference plans with 0 mm displacement are generated using 15 MV photons.

Displacement	**Energy 15 MV**					
[mm]	1	2	3	4	5	6
-3	91,29078447	91,14708543	90,00458689	90,54196735	91,98682753	91,88210119
-2,5	93,68789386	93,34587691	92,64917244	93,14435717	94,44611131	94,20665216
-2	95,71597644	95,75660835	94,92552892	95,13117623	96,62346292	96,40119266
-1,5	97,52434208	97,54494441	96,88860543	97,08542701	98,40008721	98,11445623
-1	98,85906607	98,71001303	98,34588435	98,51617207	99,37650205	99,2932081
-0,5	99,57813241	99,53555917	99,39276013	99,49002386	99,81015915	99,74942948
0	100	100	100	100	100	100
0,5	99,89550314	99,94291357	100,0032079	99,98905382	99,88608291	99,98712781
1	99,4460455	99,45492412	99,45276666	99,65159738	99,52173062	99,7849734
1,5	98,43032118	98,47990891	98,2539206	98,57120658	98,78878629	99,17381793
2	96,79764491	96,97236593	96,75346133	97,08396976	97,4191485	97,70011873
2,5	94,99226735	94,96222262	94,88350035	94,98567151	95,550336	95,78632357
3	92,50624714	92,4788247	92,71780724	92,67902527	93,30768821	93,39977684

D_{95} values calculated for each displacement when PTV was positioned in lung tissue are found in table B.12.

Table B.12: Calculated D_{95} for each displacement when PTV comprised of lung tissue.

Displacement	**Lung tissue**					
[mm]	1	2	3	4	5	6
-3	89,66893955	90,39919245	89,46554752	90,75459405	89,16731534	88,66514853
-2,5	92,5776278	93,11739786	92,41682018	93,43042282	92,01230419	91,44785171
-2	95,43509701	95,73998086	95,21249525	95,89196837	94,76013775	94,43064178
-1,5	97,4315186	97,58850126	97,29370292	97,7118062	96,77841481	96,60532177
-1	98,92090489	99,04198401	98,89386367	99,02287801	98,59174467	98,42165199
-0,5	99,75152123	99,80652342	99,76626896	99,77176102	99,69019948	99,57373368
0	100	100	100	100	100	100
0,5	99,6937594	99,74003567	99,63259783	99,64291532	99,67801205	99,85021099
1	98,64010732	98,89388286	98,66530468	98,77224697	98,74253087	98,96899585
1,5	97,02667968	97,6195393	97,35389791	97,46622202	97,30763804	97,47538682
2	94,94716239	95,78397804	95,4232439	95,51786308	95,43788304	95,5596268
2,5	92,14239757	93,44781855	92,86781908	92,92071804	93,03917092	92,93653995
3	89,24603984	90,96666068	90,1672405	90,35570408	90,60032293	90,12140973

Table B.13 presents the calculated D_{95} for each displacement when PTV was positioned in bone.

Table B.13: D_{95} values for each displacement for PTV placed in bone.

Displacement [mm]	Bone					
	1	2	3	4	5	6
-3	88,05845137	89,0382956	89,33711154	89,14276232	89,78513814	89,2543541
-2,5	91,29432086	92,03982855	92,39553391	92,1348367	92,7588589	92,30749529
-2	93,78539847	94,34674819	94,70468301	94,67390974	95,09794809	94,68568668
-1,5	96,34481319	96,80811071	96,9508222	96,92885206	97,12792441	96,9381471
-1	98,11299489	98,36817015	98,48220922	98,62907064	98,48576538	98,54565979
-0,5	99,27890167	99,60941868	99,52060223	99,66634083	99,54410251	99,56457106
0	100	100	100	100	100	100
0,5	99,86397023	99,3517431	99,48047941	99,58325625	99,65854599	99,74296781
1	98,67085312	98,08288987	98,23019477	98,33185045	98,47582597	98,57427058
1,5	97,2506648	96,28191646	96,59690674	96,69283595	97,03845069	97,23113827
2	94,76404653	93,44330551	94,33611387	93,67128045	94,61507565	94,86960082
2,5	92,27937088	90,96321671	92,12423288	91,03395108	92,29760837	92,57094681
3	88,72999578	87,16227819	89,10225987	86,98747443	89,02764074	89,33805725

D_{95} values for each displacement for plans generated using patient images with a 22 mm diameter PTV are seen in table B.14.

Table B.14: D_{95} values calculated for each displacement. The reference plans are generated using patient images with a spherical 22 mm PTV.

Displacement [mm]	Patient image 22 mm PTV					
	1	2	3	4	5	6
-3	86,28138606	87,36612917	87,13072652	86,18663041	87,06349106	87,33022457
-2,5	89,71127725	90,69504557	90,73596076	89,75201036	90,41829128	90,4414719
-2	93,04273407	93,84457703	93,81854482	92,82617813	93,32626779	93,44604718
-1,5	95,62338455	96,28796273	96,37088068	95,69695113	95,89574052	99,28535472
-1	97,72046718	98,34973315	98,39865985	97,91357473	97,95432588	97,80215522
-0,5	99,41110906	99,7936263	99,60073298	99,37782379	99,44970982	99,28521279
0	100	100	100	100	100	100
0,5	99,80761001	99,50148289	99,44165096	99,60322632	99,67453599	99,76226233
1	98,47357737	98,04907951	98,29670907	98,4275108	98,48831568	98,63634381
1,5	96,32655153	95,83419951	96,5710652	96,81455228	96,7674842	96,95641965
2	93,93369576	93,18606808	94,05341332	94,72055035	94,6221182	94,76027366
2,5	90,68353119	90,09197033	90,73240491	91,93181912	91,81797359	92,08874077
3	87,42417812	86,68455279	87,23593392	88,9714209	88,82544268	88,99843881

D_{95} values for plans generated using patient images with a 26 mm diameter PTV are seen in table B.15.

Table B.15: Calculated D_{95} values for each displacement for six different reference plans. The plans are generated using patient images with a 26 mm diameter PTV.

Displacement	**Patient image 26 mm PTV**					
[mm]	1	2	3	4	5	6
-3	88,80212955	89,46358366	89,6199491	91,43939771	92,25533115	89,41954845
-2,5	92,06548673	92,44251329	92,83576595	94,00953385	94,5363443	92,52485434
-2	94,65604939	94,99654364	95,13012697	96,11334441	96,38358089	95,07546952
-1,5	97,02162304	97,19679859	97,26872239	97,75492586	98,14454393	97,18648759
-1	98,71485608	98,87095254	98,73992278	99,02508796	99,26022462	98,73941939
-0,5	99,64418028	99,69716397	99,6936993	99,76092547	99,74531644	99,63052728
0	100	100	100	100	100	100
0,5	99,80727966	99,67660482	99,81767104	99,77806379	99,88082077	99,82272992
1	99,16023611	98,77803086	99,07239673	99,16945043	99,56278059	99,17279807
1,5	97,77171668	97,20778218	97,7928531	97,97277051	98,87056566	97,92443099
2	96,01749148	95,24974118	96,00911843	96,31439795	97,16292659	96,13780093
2,5	93,78848437	93,03236845	93,85968351	94,25158396	95,11241637	94,10055017
3	90,99135441	90,33055628	90,91117975	91,83510047	91,92450476	91,46488868

Table B.16 shows D_{95} for each displacement for six different reference plans. The reference plans are generated using patient images with a 30 mm PTV.

Table B.16: D_{95} values for 12 different displacements are presented. The reference plans are generated using patient images with a 30 mm PTV.

Displacement	**Patient image 30 mm PTV**					
[mm]	1	2	3	4	5	6
-3	92,3080713	91,40494345	92,37989574	93,10985872	93,19961299	93,23938851
-2,5	94,51552359	93,78069565	94,53481629	95,01321007	95,08219848	95,12461283
-2	96,5280212	96,073822	96,52820791	96,73781074	96,87873824	96,89073843
-1,5	97,99351561	97,68522946	97,9665483	98,01577214	98,17530191	98,27559253
-1	99,08221638	98,94016588	98,98700783	99,09459737	99,19687037	99,32975486
-0,5	99,79812318	99,71529624	99,71337956	99,75644372	99,81553023	99,85096934
0	100	100	100	100	100	100
0,5	99,83470023	99,75746569	99,79350341	99,90202794	99,92534159	99,93370224
1	99,25749463	98,98875297	99,17413462	99,37761815	99,52698701	99,57721264
1,5	98,30611989	97,96006749	98,22033289	98,56230715	98,7322832	98,8633349
2	97,00478662	96,50847976	96,65670296	97,28666361	97,43261104	97,62957795
2,5	95,28222218	94,74560047	94,61081586	95,5919815	95,76946002	96,01225324
3	93,16192196	92,59983328	92,3576814	93,58761487	93,88924202	94,18739737

D_{95} values for patient images with 35 mm PTV are seen in table B.17. D_{95} is calculated for each displacement case.

Table B.17: This table presents D_{95} values calculated for each displacement. The reference plans are generated using patient images with a spherical 35 mm PTV.

Displacement	**Patient image 35 mm PTV**					
[mm]	1	2	3	4	5	6
-3	94,3639535	95,05648934	94,07825156	94,45837347	95,04046104	94,41902935
-2,5	96,08570212	96,74746761	95,87190588	96,22508122	96,77866361	96,23090694
-2	97,67797004	98,26779546	97,53260285	97,80314174	98,26791711	97,83012935
-1,5	98,92520321	99,24120493	98,84550897	99,01661954	99,20017447	99,00221219
-1	99,58261781	99,70091964	99,60850969	99,72381345	99,72550845	99,63972517
-0,5	99,9551353	99,93761707	99,95243094	99,99498172	99,99399471	99,95762873
0	100	100	100	100	100	100
0,5	99,82214348	99,87652664	99,85987121	99,7631508	99,78969077	99,87723804
1	99,47024563	99,61488732	99,34130241	99,16629235	99,38717667	99,49595179
1,5	98,7254892	99,1000398	98,33053911	98,00546934	98,7148832	98,80059296
2	97,45313743	98,01507265	97,01960572	96,55373834	97,60531449	97,60338409
2,5	95,86214583	96,4507524	95,33731064	94,68455322	95,94248584	95,95641631
3	94,03654044	94,61526197	93,4989882	92,60841139	94,03307693	94,07743824

C Calculated dose spill

This appendix presents tables with the calculated dose spill for each displacement for every case evaluated in this thesis.

Table C.1 shows the dose spill for each displacement for plans generated using the spherical phantom.

Table C.1: Dose spill for each displacement for plans generated using the spherical water phantom.

Displacement	**Sphere phantom**					
[mm]	1	2	3	4	5	6
-3	0,13785011	0,11617033	0,11232664	0,16019248	0,13727526	0,11548124
-2.5	0,09382975	0,08090924	0,07263084	0,11727412	0,09888305	0,07654126
-2	0,0599176	0,05003927	0,04121549	0,0847638	0,06313347	0,04419073
-1.5	0,02834968	0,02401703	0,01747575	0,05112627	0,03235539	0,01886556
-1	0,01116014	0,00985564	0,00651549	0,03314593	0,01565996	0,00705953
-0.5	0,00656474	0,00754612	0,00552539	0,02116105	0,0093579	0,00602981
0	0,00359747	0,00458351	0,00322009	0,01168148	0,00695124	0,00388282
0.5	0,00656474	0,00754612	0,00552539	0,02116105	0,0093579	0,00602981
1	0,01116014	0,00985564	0,00651549	0,03314593	0,01565996	0,00705953
1.5	0,02834968	0,02401703	0,01747575	0,05112627	0,03235539	0,01886556
2	0,0599176	0,05003927	0,04121549	0,0847638	0,06313347	0,04419073
2.5	0,09382975	0,08090924	0,07263084	0,11727412	0,09888305	0,07654126
3	0,13785011	0,11617033	0,11232664	0,16019248	0,13727526	0,11548124

Table C.2 shows the calculated dose spill using the pelvis phantom with a 22 mm PTV positioned in the centre.

Table C.2: Dose spill for each displacement for plans generated using the pelvis phantom. All plans are generated for a spherical PTV positioned in the centre.

Displacement	**Pelvis phantom**					
[mm]	1	2	3	4	5	6
-3	0,22338926	0,27651161	0,2417566	0,24538896	0,22313957	0,27096779
-2,5	0,18742788	0,23031978	0,20493043	0,20907408	0,18430761	0,22869779
-2	0,15796633	0,19072271	0,17268549	0,17725584	0,15238949	0,18987825
-1,5	0,13429637	0,15673156	0,14635884	0,14826927	0,12559336	0,15555761
-1	0,11464967	0,12848042	0,12662329	0,12421039	0,10468648	0,12691644
-0,5	0,10425995	0,11055695	0,11487888	0,10928622	0,0934202	0,10881983
0	0,09900545	0,10295014	0,10936401	0,10477486	0,08865602	0,09894178
0,5	0,09874262	0,10523848	0,11302713	0,10948957	0,09003526	0,100144
1	0,10410112	0,11467284	0,12705674	0,12368992	0,10091294	0,10737346
1,5	0,11576919	0,13149749	0,1486586	0,14893176	0,12319192	0,12413512
2	0,13571746	0,1569651	0,17884488	0,18062363	0,15416267	0,15114127
2,5	0,16492419	0,19162302	0,21563278	0,21951906	0,19058729	0,18359043
3	0,20087719	0,22198236	0,25410891	0,2598695	0,22563469	0,2198646

Table C.3 presents the dose spill calculated for plans generated using the NEMA IQ phantom.

Table C.3: Dose spill for each displacement for treatment plans generated using the NEMA IQ phantom.

Displacement	**NEMA IQ phantom**					
[mm]	1	2	3	4	5	6
-3	0,22611348	0,20428876	0,2446283	0,20604991	0,21758207	0,22264404
-2,5	0,19401626	0,16811222	0,21689482	0,16848622	0,18747903	0,18451077
-2	0,16481823	0,1306451	0,18511577	0,13108718	0,1495413	0,15045897
-1,5	0,13972651	0,10279984	0,1580638	0,09830441	0,1168615	0,12908642
-1	0,11589624	0,07729671	0,12752508	0,07107379	0,09012861	0,10288476
-0,5	0,10182289	0,07104859	0,11110534	0,05530103	0,07115318	0,08530729
0	0,09782501	0,07666593	0,11080847	0,0536031	0,06499926	0,07267983
0,5	0,10267975	0,08236221	0,11181809	0,06195366	0,06398203	0,0685131
1	0,11750447	0,09554527	0,12812599	0,08077695	0,07816512	0,07797384
1,5	0,14130382	0,11078332	0,15103267	0,10565862	0,0990983	0,09451488
2	0,17014818	0,12857108	0,17674619	0,13636387	0,12934877	0,11998717
2,5	0,2001447	0,15662429	0,20487159	0,17442846	0,16417727	0,15231105
3	0,22865401	0,18986816	0,23523927	0,21228181	0,1978113	0,18956626

Table C.4 presents the dose spill for each displacement for plans generated for a 26 mm PTV positioned in the centre of the pelvis phantom.

Table C.4: Dose spill for plans generated with a 26 mm spherical PTV positioned in the centre of the pelvis phantom.

Displacement	**PTV 26 mm**					
[mm]	1	2	3	4	5	6
-3	0,24885277	0,2207183	0,28842302	0,2886623	0,28276491	0,26420842
-2,5	0,21292728	0,18090166	0,24276612	0,24705488	0,23913032	0,19629232
-2	0,17994155	0,14754657	0,20619721	0,20720561	0,1984022	0,18396134
-1,5	0,15266565	0,1196036	0,17175971	0,17049453	0,16122679	0,14849606
-1	0,13376258	0,09937221	0,14665016	0,14304411	0,1333053	0,12188151
-0,5	0,12308121	0,09082649	0,13316642	0,1235737	0,11596432	0,10604359
0	0,11853315	0,0864894	0,12579243	0,11583449	0,10790614	0,0981556
0,5	0,12380569	0,08963511	0,12561956	0,12170664	0,10806771	0,09943773
1	0,13736142	0,09947353	0,13108857	0,13748638	0,11567414	0,11086377
1,5	0,1605781	0,11885024	0,14942328	0,16500671	0,13494496	0,13171934
2	0,18953948	0,14439323	0,17629154	0,19716378	0,16207823	0,15807936
2,5	0,22307284	0,175153	0,21062277	0,2333346	0,19260056	0,19078952
3	0,26188838	0,20956576	0,24812284	0,27024926	0,22819624	0,22620719

Table C.5 presents the dose spill calculated for plans generated for a spherical 30 mm PTV positioned in the centre of the pelvis phantom.

Table C.5: Dose spill for each displacement for six plans generated for a 30 mm PTV positioned in the pelvis phantom's centre.

Displacement	**PTV 30 mm**					
[mm]	1	2	3	4	5	6
-3	0,23251829	0,2078401	0,22224394	0,21916022	0,22593402	0,24570434
-2,5	0,19689493	0,17565734	0,18853989	0,18290585	0,18847454	0,20826095
-2	0,166119	0,14529819	0,15775894	0,1495434	0,15443628	0,17561589
-1,5	0,13900921	0,12071172	0,12940534	0,11950794	0,12512861	0,14341534
-1	0,11979474	0,10373071	0,10989787	0,099034	0,10364885	0,11797773
-0,5	0,10652763	0,09295313	0,09593653	0,08719835	0,09067135	0,10155495
0	0,1011734	0,09010509	0,09285187	0,08563231	0,08698901	0,096022
0,5	0,10508532	0,09427618	0,09811618	0,08978639	0,09025479	0,0987207
1	0,12098893	0,10771297	0,11137736	0,10117404	0,10203176	0,11190051
1,5	0,14381587	0,13094932	0,13081694	0,11854292	0,12012395	0,1319181
2	0,17060643	0,16374434	0,15682398	0,14308635	0,14559801	0,15650813
2,5	0,20117462	0,19884495	0,18743337	0,17113832	0,17442666	0,18444398
3	0,23045122	0,23697865	0,22077766	0,20190429	0,20528371	0,21374346

The calculated dose spill for plans optimised for a spherical 35 mm PTV positioned in the centre of the pelvis phantom is presented in table C.6.

Table C.6: Dose spill for plans generated with a 35 mm spherical PTV positioned in the centre of the pelvis phantom.

Displacement	**PTV 35 mm**					
[mm]	1	2	3	4	5	6
-3	0,11031688	0,19117551	0,2119863	0,13863798	0,20167114	0,12522842
-2,5	0,09571884	0,16218707	0,1796622	0,11514096	0,17253944	0,10838116
-2	0,08387997	0,13633181	0,14875255	0,09639166	0,14595166	0,09525633
-1,5	0,07494118	0,11266697	0,12124453	0,0813601	0,12252338	0,08445503
-1	0,06972072	0,09332379	0,09969977	0,07063924	0,10413451	0,07746629
-0,5	0,0671162	0,08077715	0,08791922	0,06416902	0,09223988	0,07361203
0	0,06805373	0,07703223	0,08530353	0,06232758	0,08709233	0,07167244
0,5	0,07476354	0,07894539	0,09075549	0,0661444	0,08727021	0,07494293
1	0,09236326	0,09280216	0,10376192	0,07961355	0,09751464	0,0901789
1,5	0,11948285	0,11724748	0,12471342	0,1036309	0,11809739	0,11358279
2	0,15131273	0,14600856	0,15299147	0,13269153	0,14394829	0,14302998
2,5	0,18517917	0,1786016	0,18452909	0,16604126	0,17383361	0,17594222
3	0,22094654	0,21095202	0,21766159	0,20043066	0,20449113	0,2111536

Dose spill for plans generated for a spherical PTV positioned 3 cm from the centre of the pelvis phantom is found in table C.7.

Table C.7: Dose spill calculated for plans generated for PTV positioned 3 cm from the centre of the pelvis phantom.

Displacement	**PTV 3 cm**					
[mm]	1	2	3	4	5	6
-3	0,32996931	0,25032664	0,33399066	0,27675026	0,26276211	0,24557311
-2,5	0,28195918	0,20811732	0,28689367	0,22580213	0,21716947	0,20760398
-2	0,23804764	0,17277942	0,24226783	0,18542844	0,1770441	0,17575067
-1,5	0,19736596	0,13927797	0,20218821	0,15371375	0,14007853	0,14912171
-1	0,16421004	0,11535769	0,16910938	0,12962411	0,11214965	0,13230821
-0,5	0,14344223	0,10279504	0,14417078	0,11263213	0,0941305	0,11999695
0	0,13574693	0,09840867	0,13036832	0,1025261	0,08801061	0,11151366
0,5	0,13749328	0,10516222	0,12933211	0,1014991	0,09552859	0,10964216
1	0,1459684	0,12563744	0,13780248	0,11230346	0,11235309	0,11608447
1,5	0,1665095	0,15431251	0,15748949	0,13326798	0,13837215	0,13545535
2	0,19489389	0,18814164	0,18198466	0,15885455	0,17054638	0,16694668
2,5	0,23046379	0,226913	0,21048604	0,19013735	0,20822193	0,20147141
3	0,26729384	0,26665711	0,23799289	0,22435682	0,25094579	0,24002526

Table C.8 presents the dose spill calculated for each displacement for plans generated for PTV positioned 6 cm from the centre of the pelvis phantom.

Table C.8: Dose spill for plans generated for a spherical 22 mm PTV positioned 6 cm from the pelvis phantom's centre.

Displacement	**PTV 6 cm**					
[mm]	1	2	3	4	5	6
-3	0,27971493	0,32510605	0,34833787	0,26454516	0,32125419	0,26057502
-2,5	0,24014608	0,2754572	0,29935817	0,22944964	0,27334077	0,2244823
-2	0,20465549	0,22828589	0,24942171	0,18842458	0,22786225	0,19604014
-1,5	0,1741631	0,18617852	0,2058006	0,15320478	0,19073566	0,16818706
-1	0,14670718	0,15037467	0,1649158	0,12343169	0,15802143	0,1412393
-0,5	0,12765297	0,12533047	0,13163844	0,10401138	0,13704101	0,11942629
0	0,11862253	0,10511336	0,10890168	0,09738407	0,1211969	0,10471452
0,5	0,11788892	0,09746925	0,10043175	0,10474895	0,11535997	0,09877
1	0,125319	0,10526173	0,1064525	0,1219634	0,12360079	0,10553714
1,5	0,14396153	0,12416514	0,12847558	0,14772515	0,14750424	0,12320626
2	0,17260753	0,15041738	0,15399395	0,17544923	0,17275257	0,15360692
2,5	0,20525976	0,18603512	0,18571604	0,21034544	0,20458968	0,18004928
3	0,23942449	0,21465697	0,21572335	0,24540334	0,2376624	0,21118423

Table C.9 presents the dose spill calculated for plans generated for PTV positioned 9 cm from the pelvis phantom's centre.

Table C.9: Dose spill calculated for the plans generated for PTV positioned 9 cm from the centre of the pelvis phantom.

Displacement	**PTV 9 cm**					
[mm]	1	2	3	4	5	6
-3	0,32762633	0,26025107	0,24367884	0,24372059	0,3115437	0,29863329
-2,5	0,27432759	0,21585585	0,20251854	0,20605274	0,26315517	0,24819502
-2	0,22674641	0,18556511	0,17559041	0,18323369	0,21945784	0,20295389
-1,5	0,18758555	0,1623523	0,15188883	0,16213664	0,17712542	0,1615724
-1	0,15054254	0,13897687	0,13523463	0,1469586	0,13617437	0,12511318
-0,5	0,12979253	0,121388	0,12062769	0,13687548	0,11162686	0,1048788
0	0,12002612	0,11901226	0,11221464	0,13498815	0,10237144	0,08849391
0,5	0,1162862	0,12091797	0,12005762	0,12945555	0,09932123	0,08734697
1	0,12197771	0,12961353	0,13396428	0,13396512	0,10912984	0,09874968
1,5	0,13465731	0,14354518	0,15265334	0,14775995	0,118803	0,12241641
2	0,15314822	0,1566006	0,17031967	0,16993828	0,13020616	0,14954192
2,5	0,18101491	0,18761101	0,19314726	0,19277105	0,14658279	0,17877776
3	0,20737447	0,21207935	0,21869334	0,21326876	0,16667298	0,20457136

Dose spill for each displacement for treatment plans generated with 10 MV photons is found in table C.10.

Table C.10: Dose spill for treatment plans generated with 10 MV photons.

Displacement	**Energy 10 MV**					
[mm]	1	2	3	4	5	6
-3	0,24153467	0,25008684	0,23832217	0,29941295	0,2729028	0,27894616
-2,5	0,2045444	0,21397081	0,20302688	0,25998035	0,23593663	0,24162386
-2	0,17025186	0,18376209	0,17293758	0,22448025	0,20266464	0,20888128
-1,5	0,13811896	0,15852639	0,15022739	0,19206794	0,17252538	0,17972318
-1	0,11369781	0,13795967	0,130767	0,16487459	0,14704907	0,15358222
-0,5	0,09781516	0,12527537	0,11996867	0,14865321	0,13175853	0,13819602
0	0,08985036	0,1162567	0,11278977	0,1392557	0,12259536	0,13012289
0,5	0,09236951	0,11482561	0,1125844	0,142021	0,12641173	0,13597311
1	0,10630293	0,11811396	0,11878983	0,15491845	0,14180211	0,15552344
1,5	0,13140728	0,13056166	0,13361596	0,17792363	0,16688544	0,18585433
2	0,16444848	0,1532482	0,15820765	0,21130083	0,20217351	0,22335393
2,5	0,20311581	0,1821428	0,18844105	0,2517859	0,24364239	0,26507388
3	0,24291127	0,21682818	0,22367832	0,29331944	0,28589429	0,30649751

Table C.11 shows the calculated dose spill for plans generated with 15 MV photons.

Table C.11: Calculated dose spill for plans generated using 15 MV photons.

Displacement	**Energy 15 MV**					
[mm]	1	2	3	4	5	6
-3	0,26865653	0,28159913	0,27414154	0,28899845	0,28636107	0,32568362
-2,5	0,22575812	0,23602681	0,23412346	0,24398192	0,2454939	0,28482188
-2	0,18722557	0,19519753	0,20107557	0,20471362	0,21003446	0,24696457
-1,5	0,15259156	0,16054443	0,17258858	0,17115101	0,17906716	0,21186798
-1	0,12502563	0,13856211	0,14856905	0,14574717	0,15326587	0,18156812
-0,5	0,1039462	0,12511785	0,13358827	0,12713283	0,13575152	0,16236014
0	0,09284009	0,1218398	0,12372675	0,11351271	0,12789973	0,15090192
0,5	0,09266527	0,12211003	0,12205176	0,11171381	0,13374856	0,15208981
1	0,10371934	0,13027535	0,12530496	0,11905022	0,1523048	0,1648597
1,5	0,12155745	0,14551231	0,13737544	0,13321556	0,18030244	0,18805701
2	0,14838169	0,16983308	0,15830015	0,1555541	0,21589752	0,21955228
2,5	0,17764071	0,19794367	0,18432512	0,18199819	0,25490204	0,25587176
3	0,21144216	0,22784949	0,21704915	0,21403378	0,29592081	0,2923036

Dose spill for each displacement for plans generated with PTV positioned in lung tissue is presented in table C.12.

Table C.12: Dose spill for six reference plans and displacement plans generated with PTV positioned in lung tissue.

Displacement	**Lung tissue**					
[mm]	1	2	3	4	5	6
-3	0,15716121	0,16445885	0,17287438	0,15318765	0,12382941	0,16446545
-2,5	0,11491606	0,1273182	0,13558663	0,11955064	0,08700715	0,12822874
-2	0,0834164	0,10298953	0,1111196	0,0868017	0,06503706	0,10596974
-1,5	0,06460873	0,08565806	0,09490327	0,07331474	0,05963258	0,09843813
-1	0,05450435	0,07162849	0,08332221	0,0689786	0,05870982	0,08928017
-0,5	0,05424922	0,06406666	0,0802935	0,06840337	0,05847481	0,08358178
0	0,05556856	0,05924007	0,07791532	0,06904189	0,05906556	0,0792367
0,5	0,0572566	0,05692004	0,07613416	0,07001114	0,05972329	0,07680112
1	0,06346036	0,06314904	0,07736345	0,08080673	0,06212469	0,07848546
1,5	0,07691786	0,08004568	0,08213752	0,09786375	0,06851807	0,08117511
2	0,10051683	0,108209	0,09978624	0,12025482	0,08216583	0,09082253
2,5	0,13590681	0,14887761	0,13441441	0,15380364	0,11234106	0,11731274
3	0,17312177	0,18499972	0,17645943	0,19072893	0,15367535	0,14900624

Table C.13 shows the calculated dose spill for plans generated with PTV positioned in bone. Dose spill is calculated for each displacement.

Table C.13: Dose spill for each displacement for treatment plans generated with PTV positioned in bone.

Displacement	**Bone**					
[mm]	1	2	3	4	5	6
-3	0,22192565	0,22084504	0,22556169	0,24485707	0,23678549	0,27667834
-2,5	0,18780957	0,18008644	0,18742012	0,20795813	0,20038573	0,23659407
-2	0,15664374	0,14049695	0,15568016	0,17297442	0,16587921	0,19540321
-1,5	0,12849895	0,11329405	0,12934559	0,14410869	0,13632765	0,15964989
-1	0,10811918	0,09453742	0,11080104	0,12351106	0,11550502	0,13534163
-0,5	0,0969008	0,08880691	0,10213476	0,11479915	0,10603896	0,12094889
0	0,0874483	0,08288901	0,09559321	0,1087622	0,10071808	0,1176508
0,5	0,09545894	0,08989241	0,10367693	0,11484483	0,11083667	0,12610825
1	0,10828585	0,09721472	0,11315834	0,12516115	0,1253814	0,1405022
1,5	0,12469852	0,11284036	0,12668077	0,14127064	0,14251071	0,16105211
2	0,15032047	0,14009614	0,15381587	0,16694218	0,1740093	0,19558033
2,5	0,17742222	0,16741048	0,18399978	0,19299232	0,20460951	0,23058074
3	0,20590282	0,19640838	0,21759612	0,21899184	0,23854593	0,26697093

Dose spill for each displacement for plans generated using patient images with a 22 mm diameter PTV is presented in table C.14.

Table C.14: Calculated dose spill for plans generated using patient images with 22 mm diameter PTV.

Displacement	**Patient 22 mm**					
[mm]	1	2	3	4	5	6
-3	0,16318015	0,17015137	0,1901178	0,189666	0,210644	0,197653
-2,5	0,13170636	0,13238164	0,15793606	0,158519	0,17635	0,158769
-2	0,10158865	0,10415857	0,12196303	0,127629	0,143458	0,125493
-1,5	0,08523691	0,09129579	0,09323739	0,107057	0,11986	0,093825
-1	0,08091092	0,0850538	0,0775621	0,096744	0,10668	0,095638
-0,5	0,08224948	0,08361724	0,07141279	0,092014	0,102721	0,093817
0	0,0848668	0,08500622	0,07100678	0,092587	0,103119	0,091696
0,5	0,08225596	0,08204252	0,06867769	0,090842	0,100892	0,092813
1	0,0824194	0,08265329	0,07250473	0,09818	0,100222	0,098891
1,5	0,08748245	0,09367212	0,08501983	0,112957	0,106684	0,111008
2	0,1023949	0,11335358	0,11088199	0,139875	0,120359	0,129754
2,5	0,12761182	0,13939982	0,1458723	0,169697	0,14092	0,155099
3	0,1555494	0,16856552	0,18372415	0,204683	0,158665	0,185972

Table C.4 shows the dose spill calculated for plans generated using patient images with a 26 mm diameter PTV.

Table C.15: Calculated dose spill for each displacement for treatment plans generated using patient images with spherical 26 mm PTV.

Displacement	**Patient 26 mm**					
[mm]	1	2	3	4	5	6
-3	0,24015906	0,17805929	0,23553074	0,206617	0,294464	0,231669
-2,5	0,20652509	0,14503489	0,20037006	0,174966	0,261338	0,196292
-2	0,17524473	0,11405754	0,16952093	0,148629	0,227052	0,166445
-1,5	0,14607383	0,08695652	0,13797363	0,122974	0,193175	0,138324
-1	0,12334717	0,07255837	0,11427428	0,105031	0,16453	0,115169
-0,5	0,10994648	0,0679918	0,10113982	0,094946	0,145143	0,100561
0	0,10515935	0,06902875	0,09690723	0,091227	0,132106	0,093632
0,5	0,11268183	0,07533553	0,10359162	0,097813	0,134337	0,098329
1	0,12059788	0,0804487	0,1117319	0,106959	0,139341	0,103393
1,5	0,13862431	0,0940781	0,13100767	0,124382	0,15391	0,117668
2	0,16265262	0,11506089	0,15934396	0,14677	0,175201	0,138004
2,5	0,19658014	0,14493586	0,19620908	0,177034	0,204172	0,168372
3	0,23497761	0,18136499	0,23838782	0,213848	0,237464	0,205375

Dose spill calculated for plans generated using patient images with a spherical 30 mm PTV is presented in table C.5.

Table C.16: Calculated dose spill for plans generated using patient images with 30 mm diameter PTV.

Displacement	**Patient 30 mm**					
[mm]	1	2	3	4	5	6
-3	0,213318	0,18070434	0,20622724	0,20142	0,225394	0,221592
-2,5	0,18916649	0,15760725	0,17851377	0,176313	0,192465	0,190885
-2	0,16555976	0,13595867	0,15152719	0,151834	0,161022	0,162066
-1,5	0,14232173	0,11695124	0,12668445	0,127564	0,130868	0,134425
-1	0,12206987	0,09856078	0,10495497	0,105987	0,104702	0,11358
-0,5	0,10606827	0,08429498	0,0876633	0,087637	0,08774	0,099236
0	0,1026235	0,08394895	0,08754374	0,079549	0,08497	0,096856
0,5	0,10733775	0,08800862	0,091607	0,0787	0,087397	0,100708
1	0,12475453	0,09997344	0,1041553	0,086993	0,096503	0,109018
1,5	0,14693928	0,11984431	0,12333063	0,100534	0,110234	0,123542
2	0,17470469	0,14413022	0,1484561	0,120626	0,132896	0,143968
2,5	0,20736489	0,17395369	0,17883208	0,148856	0,160298	0,173069
3	0,2412259	0,20495119	0,20924504	0,179855	0,190741	0,204085

Dose spill for each displacement calculated for plans generated using patient images with a spherical 35 mm PTV is presented in table C.17.

Table C.17: Calculated dose spill for each displacement for treatment plans generated using patient images with spherical 35 mm PTV.

Displacement	**Patient 35 mm**					
[mm]	1	2	3	4	5	6
-3	0,16147255	0,18773777	0,17701272	0,168163	0,141303	0,165715
-2,5	0,13866413	0,1639143	0,15490585	0,144783	0,123883	0,144844
-2	0,11549603	0,13896131	0,13186803	0,120311	0,105691	0,12361
-1,5	0,0958499	0,11742946	0,1116049	0,10233	0,090016	0,104728
-1	0,07986902	0,09884442	0,09624411	0,089773	0,076742	0,089542
-0,5	0,07262825	0,08849178	0,08888172	0,08502	0,069931	0,08148
0	0,07536194	0,08640167	0,08896973	0,087022	0,072358	0,082966
0,5	0,08163261	0,08933902	0,09268157	0,092823	0,080295	0,089322
1	0,09677715	0,1003135	0,10438314	0,10593	0,093824	0,102825
1,5	0,115938	0,11888781	0,12061386	0,122272	0,111993	0,120929
2	0,14226011	0,14481031	0,14461891	0,147258	0,137919	0,146602
2,5	0,17019207	0,17460047	0,17159922	0,175133	0,167179	0,175707
3	0,19757072	0,20259626	0,19940885	0,203632	0,195499	0,205255

D Calculated CI

This appendix contains tables with calculated CI for each displacement for the treatment plans generated for this thesis.
Table D.1 presents the calculated CI for each displacement for the plans generated using the spherical water phantom images.

Table D.1: CI for each displacement for treatment plans generated using the spherical phantom.

Displacement	**Sphere phantom**					
[mm]	1	2	3	4	5	6
-3	0,77351764	0,87208173	0,87687316	0,84535841	0,85654062	0,89078549
-2,5	0,82833238	0,90914201	0,91797882	0,88890794	0,89620303	0,92879206
-2	0,87578384	0,9413695	0,95096378	0,92152726	0,9328142	0,95956407
-1,5	0,92326359	0,97023461	0,9773914	0,95672015	0,96643719	0,98504735
-1	0,95711969	0,98652358	0,99062788	0,97552452	0,98535287	0,99658225
-0,5	0,97896001	0,99168811	0,99399666	0,98842328	0,99387257	0,99707692
0	1	1	1	1	1	1
0,5	0,97896001	0,99168811	0,99399666	0,98842328	0,99387257	0,99707692
1	0,95711969	0,98652358	0,99062788	0,97552452	0,98535287	0,99658225
1,5	0,92326359	0,97023461	0,9773914	0,95672015	0,96643719	0,98504735
2	0,87578384	0,9413695	0,95096378	0,92152726	0,9328142	0,95956407
2,5	0,82833238	0,90914201	0,91797882	0,88890794	0,89620303	0,92879206
3	0,77351764	0,87208173	0,87687316	0,84535841	0,85654062	0,89078549

CI for each displacement for plans generated for 22 mm PTV in the centre of the pelvis phantom is shown in table D.2.

Table D.2: CI for each displacement for plans generated for a 22 mm PTV in the centre of the pelvis phantom.

Displacement	**Pelvis phantom**					
[mm]	1	2	3	4	5	6
-3	0,80071796	0,72323277	0,76225066	0,75652632	0,78674601	0,76787132
-2,5	0,84738231	0,7831112	0,81292901	0,8117891	0,83445454	0,81970351
-2	0,88830081	0,83861924	0,8610696	0,86058051	0,87806125	0,86816649
-1,5	0,92395837	0,89092055	0,90721384	0,90466803	0,91839826	0,91246426
-1	0,95672437	0,93667303	0,94622024	0,94470891	0,95427599	0,95152374
-0,5	0,98036739	0,97188535	0,97602593	0,97528864	0,98064256	0,97960175
0	1,00001486	0,99994059	0,99989188	0,99994062	0,9998872	0,99995121
0,5	1,01295998	1,01828367	1,01337077	1,01609069	1,00732184	1,00757472
1	1,0203219	1,0287684	1,0148352	1,02181752	1,0013719	1,00858752
1,5	1,02047946	1,02938608	1,00658822	1,0166508	0,9829492	0,99937738
2	1,01011643	1,02083128	0,98552592	1,00137635	0,95624919	0,97765283
2,5	0,99113764	1,00456635	0,95569054	0,97823043	0,92059783	0,94982539
3	0,96322493	0,98410769	0,92147562	0,95105333	0,88222239	0,91833325

Table D.3 presents the calculated CI for each displacement for treatment plans generated using the NEMA IQ phantom images. The plans were optimised for a spherical 22 mm PTV.

Table D.3: CI for each displacement for plans generated for a 22 mm PTV in the NEMA IQ phantom.

Displacement	**NEMA IQ phantom**					
[mm]	1	2	3	4	5	6
-3	0,78533228	0,77313928	0,7757612	0,79221997	0,77906258	0,77882909
-2,5	0,83303435	0,82306552	0,82474838	0,83911174	0,82470508	0,82496649
-2	0,88163966	0,87322898	0,87555289	0,8867494	0,87553898	0,87442524
-1,5	0,92853515	0,91888542	0,92168542	0,93009109	0,92122641	0,91685547
-1	0,96593801	0,96108963	0,96616602	0,96765409	0,96015533	0,95777406
-0,5	0,99039954	0,9876211	0,99218427	0,99369549	0,98789244	0,9849817
0	1	1	1	1	1	1
0,5	0,9948732	1,00182882	0,99211107	0,99218875	1,00386507	1,00458684
1	0,97810636	0,99034503	0,97050801	0,9727221	0,99217661	0,99321955
1,5	0,95036022	0,97173765	0,93856186	0,94493238	0,96730029	0,96338193
2	0,91957728	0,94654425	0,90420705	0,91146823	0,93475054	0,92558996
2,5	0,88693261	0,91536638	0,86832788	0,8729188	0,89840028	0,88464668
3	0,85325478	0,88151507	0,83222267	0,83262692	0,86031265	0,84273045

CI for each displacement for plans generated with a 26 mm PTV positioned in the centre of the pelvis phantom is presented in table D.4.

Table D.4: Calculated CI for each displacement for plans generated for a 26 mm PTV in the centre of the pelvis phantom.

Displacement	**PTV 26 mm**					
[mm]	1	2	3	4	5	6
-3	0,85006339	0,83912849	0,75715315	0,8066845	0,76580592	0,74540636
-2,5	0,89111174	0,8840071	0,815287	0,8515205	0,81930487	0,92501629
-2	0,92930394	0,92286145	0,86941266	0,8947797	0,8700683	0,8508853
-1,5	0,96076707	0,95520504	0,91801838	0,93525323	0,91735194	0,90206604
-1	0,98226173	0,97765795	0,95608751	0,96674974	0,95511254	0,94374835
-0,5	0,99537381	0,9911348	0,98195323	0,98996235	0,98248521	0,97610398
0	1	1	1	1	1	1
0,5	0,99427839	1,00103496	1,00861962	0,99418706	1,00788551	1,01409224
1	0,97984387	0,99528543	1,01095578	0,97773701	1,00879084	1,01942689
1,5	0,95495116	0,9792517	0,99760341	0,9482562	0,99635403	1,01333607
2	0,92222672	0,95608904	0,97425847	0,91345776	0,97456256	0,99934717
2,5	0,88587282	0,92795409	0,94258136	0,87444614	0,94946781	0,977967
3	0,84347199	0,89546974	0,9067293	0,8351092	0,91982909	0,95170229

Table D.5 shows the CI for each displacement for plans generated with a 30 mm PTV positioned in the centre of the pelvis phantom.

Table D.5: CI for each displacement for a spherical 30 mm PTV positioned in the centre of the pelvis phantom.

Displacement	**PTV 30 mm**					
[mm]	1	2	3	4	5	6
-3	0,80587024	0,88466999	0,84773913	0,85752867	0,81426396	0,76319965
-2,5	0,85000567	0,91630147	0,88591454	0,89628785	0,85885829	0,81209131
-2	0,89026118	0,94603323	0,92090916	0,93163257	0,90090559	0,8611662
-1,5	0,92858862	0,97026175	0,95379784	0,96321835	0,93867361	0,90643121
-1	0,9600773	0,98772611	0,97743509	0,98505172	0,96860525	0,94635658
-0,5	0,9858717	0,99800544	0,99490439	0,99822629	0,99000597	0,97862478
0	1,00003092	1,00003491	1,00003491	1,00003477	1,00003495	1,00003491
0,5	1,00571784	0,99310018	0,99564571	0,99651608	1,00517925	1,01258353
1	1,00023016	0,97631113	0,98387177	0,98577859	1,00109924	1,01517574
1,5	0,98681405	0,9496459	0,96507195	0,96673552	0,98896191	1,00820938
2	0,96670149	0,91389519	0,94014825	0,94122428	0,96930513	0,99567021
2,5	0,94291788	0,87509288	0,90955934	0,91213469	0,94438485	0,97806141
3	0,91917895	0,83374869	0,87742849	0,88038566	0,91736422	0,95758846

Calculated CI for plans generated for a spherical 35 mm PTV positioned in the the pelvis phantom's centre is presented in table D.6.

Table D.6: CI for each displacement for plans generated for a 35 mm PTV positioned in the centre of the pelvis phantom.

Displacement	**PTV 35 mm**					
[mm]	1	2	3	4	5	6
-3	0,98256465	0,8338467	0,88602662	0,90644217	0,83220563	0,93145219
-2,5	0,9928496	0,87150073	0,91831063	0,93284599	0,87088237	0,95031197
-2	0,99973266	0,90613948	0,94735466	0,95546789	0,9064041	0,96654473
-1,5	1,00387208	0,93734263	0,97289308	0,97390631	0,93922418	0,97940032
-1	1,00503592	0,96396045	0,99165351	0,98725249	0,96593803	0,98875616
-0,5	1,00505307	0,98717056	1,00173171	0,99676187	0,98743041	0,9971762
0	1	1	1	1	1	1
0,5	0,98979682	1,00573914	0,99237395	0,99802529	1,00912778	0,99678069
1	0,96846949	0,99859427	0,97726749	0,98667009	1,00606049	0,9830631
1,5	0,93871331	0,98011035	0,95581709	0,96605306	0,99197836	0,96150976
2	0,90334964	0,9560527	0,92642789	0,93921598	0,97170594	0,93207473
2,5	0,86588091	0,92879402	0,8913066	0,90660213	0,94637436	0,89888872
3	0,82686899	0,90016603	0,85406137	0,87250086	0,91897857	0,86375508

Calculated CI for each displacement for plans generated for a spherical 22 mm PTV positioned 3 cm from the centre of the pelvis phantom is presented in table D.7.

Table D.7: CI for each displacement for a spherical 22 mm PTV positioned 3 cm from the centre of the pelvis phantom.

Displacement	**PTV 3 cm**					
[mm]	1	2	3	4	5	6
-3	0,67555029	0,74115388	0,63898072	0,68555751	0,72601065	0,6811154
-2,5	0,74069923	0,79555895	0,70888267	0,75497255	0,78365517	0,74243945
-2	0,8041423	0,84659443	0,77701978	0,81610751	0,83823061	0,80427977
-1,5	0,86611445	0,89724072	0,84282075	0,87013499	0,89051432	0,86462308
-1	0,92302406	0,94091588	0,90307426	0,91859413	0,93612233	0,91534941
-0,5	0,96761233	0,97351489	0,9560412	0,96118776	0,9725914	0,9591403
0	0,99992156	1,00001826	0,99991179	1,00003166	1,0000594	0,99994016
0,5	1,01752114	1,01208605	1,02600186	1,02901436	1,01082727	1,02922389
1	1,02864368	1,01253456	1,04523657	1,04615236	1,01277215	1,05091779
1,5	1,02367492	0,99979578	1,05037555	1,04722528	1,00181662	1,05696856
2	1,00984066	0,97981667	1,04459619	1,03857574	0,98308246	1,04855675
2,5	0,98652146	0,95265045	1,03370929	1,02333049	0,95845903	1,03594723
3	0,96068596	0,92336031	1,02247786	1,00328201	0,92945709	1,02167985

Table D.8 shows the calculated CI for PTV positioned 6 cm from the centre of the pelvis phantom.

Table D.8: CI for each displacement for plans generated for a 22 mm PTV positioned 6 cm from the centre of the pelvis phantom.

Displacement	**PTV 6 cm**					
[mm]	1	2	3	4	5	6
-3	0,58961936	0,54152917	0,52701971	0,64533546	0,54430322	0,58783468
-2,5	0,65775553	0,61835427	0,60872962	0,70857947	0,62675817	0,65590713
-2	0,72985438	0,69883888	0,69333766	0,77454071	0,71140075	0,7269837
-1,5	0,80035238	0,7793048	0,77482231	0,83854921	0,7923688	0,79821883
-1	0,87444861	0,8608464	0,85946258	0,90284388	0,87418131	0,87051878
-0,5	0,94119316	0,93639796	0,93485037	0,95770416	0,94369371	0,93841815
0	0,99996293	0,99996293	0,99996293	0,99996293	0,99996293	0,99996293
0,5	1,0525939	1,06224918	1,05980486	1,03124204	1,04979466	1,05766833
1	1,09048337	1,10398726	1,10317001	1,05018434	1,08017384	1,09555216
1,5	1,11580168	1,13206321	1,13170415	1,05676167	1,09153513	1,12326923
2	1,1300015	1,15116069	1,14969231	1,05795084	1,09859695	1,14278528
2,5	1,12929556	1,15641363	1,1555035	1,05013272	1,09362418	1,15119673
3	1,12241211	1,15485783	1,15622875	1,03646431	1,08183529	1,14989281

Calculated CI for each displacement for treatment plans generated for a 22 mm PTVs positioned 9 cm from the centre of the pelvis phantom is shown in table D.9

Table D.9: CI for each displacement is listed in this table. The treatment plans were optimised for 22 mm PTVs positioned 9 cm from the centre of the pelvis phantom.

Displacement	**PTV 9 cm**					
[mm]	1	2	3	4	5	6
-3	0,53171211	0,59398309	0,59780172	0,57582953	0,51672397	0,57624305
-2,5	0,61894872	0,67025831	0,6705823	0,65141755	0,60070904	0,6548999
-2	0,70302724	0,74464582	0,74035347	0,72648636	0,68377782	0,73229524
-1,5	0,7856446	0,82273307	0,81229237	0,80381639	0,77328651	0,80957161
-1	0,86905843	0,89358896	0,88112449	0,87603464	0,86146333	0,88150017
-0,5	0,9412755	0,95246408	0,94186962	0,94357391	0,93576983	0,94429163
0	0,99997212	0,99997212	1,00002788	0,99997212	0,99997455	0,99997212
0,5	1,04014593	1,03203769	1,03983088	1,04430575	1,04997947	1,03627614
1	1,07118599	1,05557626	1,06990881	1,07624875	1,08595325	1,05862296
1,5	1,093003	1,070493	1,08702758	1,10309451	1,11273269	1,07128008
2	1,09967605	1,07265711	1,0926222	1,11773792	1,12590611	1,0711034
2,5	1,09461451	1,06562407	1,08589872	1,11569745	1,12823988	1,06291699
3	1,08358882	1,0531471	1,07703012	1,11233632	1,12422649	1,05125359

Calculated CI for treatment plans generated with 10 MV photons is presented in table D.10.

Table D.10: CI for each displacement for treatment plans generated with 10 MV photons.

Displacement	**Energy 10 MV**					
[mm]	1	2	3	4	5	6
-3	0,80829588	0,83651558	0,8466958	0,79120894	0,81222366	0,81534301
-2,5	0,85094898	0,87862603	0,88799685	0,83992904	0,85660449	0,86022757
-2	0,8913966	0,91414776	0,92321889	0,88402938	0,89651566	0,89961409
-1,5	0,93065015	0,94470171	0,9506494	0,92522498	0,93352101	0,93513853
-1	0,96216968	0,9702421	0,97451548	0,96079809	0,96565309	0,9671439
-0,5	0,98479872	0,98670732	0,9888516	0,98420808	0,98621706	0,98735449
0	0,99995123	0,99987686	0,99987702	0,99987693	0,99987698	0,99992061
0,5	1,00237941	1,00430046	1,00268887	1,00085932	0,99865537	0,99645434
1	0,99173625	1,00385657	0,99852531	0,98998023	0,98452277	0,97705823
1,5	0,9690307	0,99345055	0,9848536	0,96750615	0,9596047	0,94561831
2	0,93735566	0,9705579	0,95954352	0,93256662	0,9224564	0,90579526
2,5	0,8990557	0,94071494	0,92809866	0,88892524	0,87810438	0,86095982
3	0,8591973	0,90406579	0,89046935	0,84363907	0,83247866	0,81618315

Table D.11 shows the calculated CI for each displacement for the plans generated using 15 MV photons.

Table D.11: CI for each displacement for six plans generated using 15 MV photons.

Displacement	**Energy 15 MV**					
[mm]	1	2	3	4	5	6
-3	0,77596997	0,75208814	0,8031236	0,75841245	0,78806244	0,76271394
-2,5	0,82717761	0,80744148	0,85169644	0,81222035	0,8380274	0,81443611
-2	0,8731253	0,85888768	0,89254824	0,86102891	0,88238634	0,86264857
-1,5	0,91546171	0,90624989	0,92887779	0,90477605	0,92279801	0,90887939
-1	0,95120607	0,94789622	0,96064892	0,94454298	0,95776249	0,94990875
-0,5	0,98050075	0,97780684	0,98287073	0,97590753	0,98405362	0,97898098
0	0,99994048	0,99995108	0,99987687	0,9999214	0,99993071	0,99988949
0,5	1,00652157	1,0065357	1,00697323	1,01037781	0,99955457	1,00521112
1	1,00079422	1,00440699	1,00874412	1,01061271	0,98458437	0,99709114
1,5	0,98806262	0,99427149	1,00079692	1,00323733	0,95853313	0,97648237
2	0,96469392	0,97295411	0,98205102	0,98608011	0,92300495	0,94532646
2,5	0,93843944	0,94696461	0,95721819	0,96290652	0,88250027	0,90789379
3	0,90657594	0,91869378	0,92418516	0,93284892	0,83866861	0,86973425

Calculated CI for each displacement for treatment plans generated with PTV positioned in lung tissue is shown in table D.12.

Table D.12: Calculated CI for each displacement in presented in this table. The reference plans are generated for PTV positioned in lung tissue in the NEMA IQ phantom.

Displacement	**Lung tissue**					
[mm]	1	2	3	4	5	6
-3	0,8976948	0,8953683	0,88922585	0,92195797	0,91582995	0,89998752
-2,5	0,93811	0,93349602	0,92948911	0,95635895	0,95248325	0,94011464
-2	0,96788293	0,95718404	0,9565853	0,98140408	0,97581427	0,96451463
-1,5	0,98514187	0,97250588	0,97508856	0,99301825	0,98320393	0,9737662
-1	0,99450339	0,98518776	0,98804975	0,99667965	0,98723663	0,98414414
-0,5	0,99726578	0,99299064	0,99468905	0,99834187	0,99264769	0,99234479
0	1	1	1	1	1	1
0,5	1,0037013	1,00856355	1,00579741	1,00274156	1,00919681	1,0061503
1	1,00415675	1,011546	1,00769698	0,99645384	1,01529184	1,00832808
1,5	0,99626668	1,00314675	1,00546897	0,98193138	1,01680128	1,00889456
2	0,9790044	0,98528407	0,99092403	0,96298623	1,01222968	1,00270671
2,5	0,94997849	0,95495955	0,96191285	0,93331696	0,99077557	0,97873901
3	0,9192843	0,92673411	0,92973323	0,90223467	0,96430772	0,95105647

Table D.13 shows the calculated dose spill for plans generated with PTV positioned in bone.

Table D.13: CI for each displacement for treatment plans generated with PTV positioned in bone.

Displacement	**Bone**					
[mm]	1	2	3	4	5	6
-3	0,83979362	0,82379095	0,80923372	0,82519405	0,82225387	0,81386883
-2,5	0,87953515	0,87078624	0,85538149	0,87019182	0,86683288	0,85795834
-2	0,91567652	0,91783767	0,89624089	0,91319073	0,90910923	0,90456165
-1,5	0,94882531	0,9522561	0,93299226	0,94897805	0,9459123	0,94615249
-1	0,97314279	0,97694924	0,96325398	0,97531573	0,97359994	0,97455152
-0,5	0,98643594	0,98799308	0,98201939	0,9882395	0,98761877	0,99199303
0	0,9992813	0,99946329	0,99923026	0,9992813	0,99964682	0,99948321
0,5	0,99446792	0,99645979	1,00071821	0,99537604	0,9945316	0,9911528
1	0,98686943	0,99246278	0,99934757	0,9864385	0,98485666	0,973293
1,5	0,97467935	0,98267431	0,99228517	0,9705474	0,97099627	0,95054401
2	0,95221432	0,95997585	0,96807618	0,9427599	0,93964128	0,91151547
2,5	0,92917801	0,93341645	0,93716947	0,91226378	0,90631487	0,86866023
3	0,89793274	0,90128486	0,90033944	0,87751022	0,86784137	0,82304337

CI calculated for treatment plans generated for a 22 mm spherical PTV positioned in patient images is shown in table D.14.

Table D.14: CI for each displacement for plans generated on a 22 mm PTV on patient images.

Displacement	**Patient 22 mm**					
[mm]	1	2	3	4	5	6
-3	0,96352177	0,96051969	0,93228701	0,94301149	0,94245741	0,98944195
-2,5	0,98894585	0,99318348	0,95805691	0,96886067	0,97101029	1,01602426
-2	1,01078098	1,01315672	0,98312344	0,99313029	0,99626634	1,03609753
-1,5	1,01628191	1,01559817	0,99906665	1,00430978	1,01062866	1,0199567
-1	1,01232264	1,01144868	1,00520531	1,00583424	1,01377915	1,03411556
-0,5	1,00806415	1,00770136	1,00645697	1,00677467	1,01070205	1,01998169
0	1	1	1	1	1	1
0,5	0,99566158	0,99537356	0,99417165	0,99426824	0,98940679	0,9827978
1	0,98602061	0,98110272	0,98055569	0,97691929	0,97506794	0,95798732
1,5	0,97220969	0,96140534	0,95960276	0,95388744	0,95857224	0,92857349
2	0,95194928	0,9372006	0,92767305	0,92168201	0,93652872	0,89625539
2,5	0,91676778	0,90201253	0,88425143	0,88144464	0,90184605	0,85389976
3	0,88084898	0,8655582	0,83835988	0,83850133	0,86883489	0,8083774

Table D.15 presents CI calculated per displacement for plans generated using patient images with a 26 mm PTV.

Table D.15: CI for plans generated on patient images with a 26 mm spherical PTV.

Displacement	**Patient 26 mm**					
[mm]	1	2	3	4	5	6
-3	0,88625857	0,95859161	0,89209737	0,94703014	0,89441822	0,89183789
-2,5	0,92026859	0,98680573	0,92671076	0,97487155	0,92483617	0,92501629
-2	0,95172184	1,00537464	0,95645809	0,9939208	0,95379015	0,95195395
-1,5	0,97772569	1,0180363	0,98225897	1,009404	0,98065539	0,97589744
-1	0,99397114	1,01882203	0,99693412	1,01177804	1,00028543	0,99132845
-0,5	1,00056826	1,01067214	1,00191596	1,00852515	1,00359709	0,99896396
0	1	1	1	1	1	1
0,5	0,98691029	0,98210391	0,9873896	0,98096232	0,98397597	0,9879109
1	0,9747302	0,96752085	0,97438677	0,95874495	0,96370295	0,97773471
1,5	0,95024214	0,94405575	0,94570486	0,92638142	0,93277553	0,95610696
2	0,91676861	0,91191467	0,90480609	0,88967276	0,89462024	0,92632417
2,5	0,87528854	0,87247222	0,8589977	0,84783483	0,85190834	0,88768075
3	0,83145798	0,82867562	0,81053223	0,8034242	0,80676653	0,84518792

Table D.16 shows the calculated CI for each displacement. The plans are generated for patient images with a spherical 30 mm PTV.

Table D.16: CI for each displacement. The treatment plans are generated for patient images with a spherical 30 mm PTV.

Displacement	**Patient 30 mm**					
[mm]	1	2	3	4	5	6
-3	0,9348916	0,95635716	0,94299404	0,95670875	0,90710617	0,93549399
-2,5	0,95617306	0,97424213	0,96534623	0,97355982	0,93837896	0,96243829
-2	0,97600029	0,99010186	0,98466313	0,98783601	0,96621419	0,98461462
-1,5	0,99156114	0,99983669	0,99782883	0,99856813	0,98947971	1,00250579
-1	1,00122092	1,00571275	1,00680683	1,00373612	1,00166714	1,01000041
-0,5	1,00824787	1,00870826	1,01208133	1,00691716	1,00753901	1,01093389
0	1	1	1	1	1	1
0,5	0,98494574	0,98828748	0,98551885	0,98664789	0,98963629	0,98474606
1	0,95574845	0,96783608	0,96135853	0,96372858	0,97117653	0,96234618
1,5	0,92033085	0,93803182	0,92734014	0,93513994	0,94586718	0,93275722
2	0,87977463	0,90194006	0,88620794	0,90056151	0,91046753	0,89650528
2,5	0,8373044	0,86230842	0,84190284	0,86053335	0,87042606	0,85352579
3	0,79680607	0,82370812	0,79933665	0,82217856	0,83247001	0,81158617

CI calculated for treatment plans generated on a 35 mm spherical PTV positioned in patient images is shown in table D.17.

Table D.17: Calculated CI for each displacement for treatment plans generated on patient images with a spherical 35 mm PTV.

Displacement	**Patient 35 mm**					
[mm]	1	2	3	4	5	6
-3	0,98239188	0,96511713	0,95817802	0,9710832	0,98530074	0,97246049
-2,5	0,99716328	0,97859611	0,97447015	0,98849757	0,99575391	0,98478021
-2	1,01102666	0,99342669	0,99167968	1,00440218	1,00658638	0,99773298
-1,5	1,01893295	1,00252484	1,00354559	1,01210736	1,0113443	1,00536529
-1	1,02072252	1,00916509	1,00900759	1,01567696	1,01241877	1,00944493
-0,5	1,01538298	1,00816224	1,00875121	1,01328288	1,01112391	1,00971087
0	1	1	1	1	1	1
0,5	0,97792654	0,98401968	0,98541327	0,9795902	0,97981517	0,98237887
1	0,94578616	0,95827368	0,96322984	0,95306601	0,95354415	0,95839035
1,5	0,91048647	0,92483475	0,93611434	0,92281674	0,92209241	0,92933236
2	0,87006977	0,88778696	0,90281669	0,88612459	0,88569452	0,89354055
2,5	0,83102767	0,8490956	0,86787079	0,85054039	0,84895946	0,85653961
3	0,79008973	0,80790248	0,82977593	0,81205999	0,81096226	0,81715559

E MU values

Table E.1 contains the MU values characterising the different reference plans. The parameters of investigation is according to the 3.5.

Table E.1: The table show the MU values generated for each reference plan.

Parameter of investigation	Case	1	2	3	4	5	6
Shape	Sphere phantom	751.9	716.0	687.1	680.4	767.0	693.2
	Pelvis phantom	684.9	709.1	730.5	733.4	716.5	685.2
	NEMA IQ	867.2	902.7	899.6	895.6	902.0	865.4
Size	26 mm PTV	770.2	748.4	763.3	785.6	786.5	762.8
	30 mm PTV	704.1	700.8	683.3	681.0	714.9	737.6
	35 mm PTV	707.2	716.3	718.1	709.3	712.3	715.7
Position	3 cm	710.1	779.3	731.7	670.9	780.2	683.0
	6 cm	677.2	633.9	645.9	651.0	679.0	676.6
	9 cm	610.8	612.3	637.0	604.4	638.2	639.3
Energy	10 MV	691.3	729.8	733.1	687.4	694.6	688.7
	15 MV	701.4	729.2	723.7	763.5	765.2	732.6
Tissue type	Lung tissue	958.4	910.8	953.2	884.8	859.5	957.5
	Bone	713.0	723.5	747.5	683.5	714.0	750.9
Patient images	22 mm	947.1	946.8	933.3	922.2	930.5	950.5
	26 mm	823.0	835.3	828.2	766.7	897.5	821.1
	30 mm	785.7	765.6	786.1	772.2	833.5	851.5
	35 mm	845.3	813.3	851.3	835.4	844.9	850.0

F Python code

This appendix presents code created to construct the spherical water phantom and for data analysis utilised in this thesis.

Code to create the sphere

```

def spherical_mask(file_list, origo, r):
    '''
    Function to make spherical mask:
    Input:
        file_list:      list with files that is to be overwritten
        origo:          tuple with coordinates to origo of sphere (x0, y0, z0)
        r:              radius of sphere [mm]
    Output:
        mask:           mask with boolean values

    '''
    sx, sy = file_list[0].pixel_array.shape
    sz = len(file_list)

    x0, y0, z0 = origo
    xx, yy, zz = np.ogrid[:sx, :sy, :sz]
    pixel_spacing = file_list[0].PixelSpacing[0]
    slice_thickness = file_list[0].SliceThickness


    xx = xx*pixel_spacing
    yy = yy*pixel_spacing
    zz = zz*slice_thickness

    x0 = x0*pixel_spacing
    y0 = (y0*pixel_spacing)+10
    z0 = z0*slice_thickness

    mask = (xx - x0)**2 + (yy - y0)**2 + (zz - z0)**2 <= r**2

    return mask

```

```
def apply_mask(file_list, mask, new_value):
    '''
    Function to apply mask to existing files:
    Input:
        file_list:      list with files that is to be overwritten
        mask:           created mask
        new_value:      value to give the mask
    '''
    for i, slice in enumerate(file_list):
```

```
        slice.pixel_array[mask[:,:,i]] = new_value
```

Code to evaluate DVH

```
def get_dose(dvh_data):
    '''
    Function to get volume Vn in DVH volume units for every dose bin.
    Input:
        dvh_data:      DVH data attribute, a data stream describing the dose bin
                       widths Dn and associated volumes Vn in DVH Volume Units in the
                       order D1V1, D2V2, ... DnVn.
    Output:
        dose:          List of doses.
    '''
    dose= []
    for i, value in enumerate (dvh_data):
        if i%2:
            dose.append(float(value))
    return dose
```

```
def find_roots(x, curve_a, curve_b):
    '''
    Function to find intercept between two curves and the x-axis
    Input:
        x:          x-axis
        curve_a:    One curve
        curve_b:    Other curve
    Output:
        The x-axis value where the two curves intercept
    '''
    y = curve_a-curve_b
    s = np.abs(np.diff(np.sign(y))).astype(bool)
    return x[:-1][s] + np.diff(x)[s]/(np.abs(y[1:][s]/y[:-1][s])+1)
```

```

def calc_dose(dataset, dosevalue):
    '''
    The function calculates the desired volume dose
    Input:
        dataset:        Files that should be evaluated
        dosevalue:      The volume dose that is desired to be calculated
    Output:
        D_volume:    List with the volume dose calculated in the file order
    '''
    D_volume = []
    for i, file in enumerate (dataset):
        structure = file.DVHSequence[1].DVHData  #Should be the sequence that belongs
    to of the structure of interest
        dose = get_dose(structure)

```

```
        line = np.full(shape=len(dose), fill_value=dosevalue, dtype=int)

        volume_dose = dose/np.max(dose)*100
        D_volume.append(find_roots(x,volume_dose,line))

    return D_volume
```

```

def calc_ci(dataset):
    '''
    The function calculates the CI from RT Dose DICOM files.
    Input:
        dataset:    Files that should be evaluated
    Output:
        ci:         List of calculated ci value for every file in the dataset.
    '''
    ci = []
    for i, file in enumerate(dataset):
        ptv = file.DVHSequence[1].DVHData
        dose_ptv = get_dose(ptv)
        x = np.arange(0, len(dose_ptv), 1)
        x = x/100
        index = np.where(x == 2.0)
        ci.append(dose_ptv[index[0][0]] / np.max(dose_ptv))
    return ci
```

```

def calc_dosespill(dataset):
    '''
    The function calculates the dose spill from RT Dose DICOM files.
    Input:
        dataset:        Files that should be evaluated
    Output:
        dose_spill:     List of calculated dose spill value for every file in the
    dataset.
    '''
    dose_spill = []
    for i, file in enumerate(dataset):
        ptv = file.DVHSequence[1].DVHData
        body = file.DVHSequence[0].DVHData
        dose_ptv = get_dose(ptv)
        dose_body = get_dose(body)
        x = np.arange(0, len(dose_ptv), 1)
        x = x/100
        index = np.where(x == 2.0)
        dose_spill.append(1-(dose_ptv[index[0][0]] / dose_body[index[0][0]]))
    return dose spill
```

Code to create plots

```

def plot_dvh(file):
    '''
    Function to plot DVH
    Input:
        file: file containing the DVH data to plot
    '''
    structure = file.DVHSequence[1].DVHData
    dose = get_dose(structure)
    volume_dose = dose/np.max(dose)*100
    num_bins = len(volume_dose)
    x = np.arange(0, num_bins, 1) #If bin widths is 0.01
    x = x/100

    plt.figure()
    plot.plot(x, volume_dose)
    plt.show()
```

```

def display_ct(file):
    '''
    Function to display a CT image slice with HU. This function centres the image and
    scales the axis to mm.
    Input:
        file: CT slice as dicom file
    '''
    rows = (file.Rows * file.PixelSpacing[0])/2
    columns = (file.Columns * file.PixelSpacing[1])/2
    extent= [-rows, rows-0.5, -column, column-0.5]

    ct_arr = file.pixel_array * file.RescaleSlope + file.RescaleIntercept

    plt.imshow(ct_arr, cmap = "gray", extent = extent)
    plt.colorbar(label = "HU")
    plt.xlabel("mm")
    plt.ylabel("mm")
    plt.show()
```

Lene Fikstvedt

Dosimetric impact of geometric distortions in radiotherapeutic dose planning

NTNU
Kunnskap for en bedre verden

UNIVERSITETSSYKEHUSET NORD-NORGE